

THE PROCESS AND FUNCTIONALITY OF BUILDING A 1-D MECHANICAL
EARTH MODEL FROM WELL LOG DATA IN THE MIDLAND BASIN

APPROVED BY SUPERVISORY COMMITTEE:

Sumit Verma, Ph.D.

Mohamed Zobaa, Ph.D.

Miles A. Henderson, Ph.D.

Zhengwen Zeng, Ph.D.

Graduate Faculty Representative

THE PROCESS AND FUNCTIONALITY OF BUILDING A 1-D MECHANICAL
EARTH MODEL FROM WELL LOG DATA IN THE MIDLAND BASIN

By

ROBERT R HISSONG, BSc.

THESIS

Presented to the Graduate Faculty of Geology

The University of Texas Permian Basin

In Partial Fulfilment

Of Requirements

For the Degree of

MASTER OF SCIENCE

THE UNIVERSITY OF TEXAS PERMIAN BASIN

October 2020

© Copyright by Rob Hissong 2020
All Rights Reserved.

DEDICATION

This Thesis is dedicated first and foremost to my wife. Your support and patience is the reason I was able to complete my graduate degree. My advisor, Dr. Sumit Verma, for working with me through a pandemic to get the necessary data and Fasken Oil and Ranch for providing me with the dataset to perform the analysis.

ACKNOWLEDGEMENT

I would like to thank Dr. Sumit Verma for his mentorship and guidance throughout my project. His knowledge of, and helping with, coding the script necessary to perform a trained facies model from a machine learning algorithm, and willingness to branch outside of his area of expertise to provide support, truly helped me in the process. The professors, friends, and colleagues that I have had the pleasure of getting know at The University of Texas of the Permian Basin. Dr. Mohamed Zobaa for pushing me to be a writer in his Scientific Writing class and pushing me towards working with Dr. Verma. An honest thank you to everyone on my committee; insights are always appreciated.

To my wife, you are wonderful and supportive, I could not have done it without you. A special thanks to my parents for helping proof read and listen to my rants.

Finally, I would like to thank Fasken Oil and Ranch for providing the dataset for the Fee BI #307 well to the Department of Geosciences along with the Midland Energy Library for supplying DST data and logs. Without this valuable information, this project would not have been realized.

ABSTRACT

Rock mechanics play an integral role in drilling wellbores in the oil and gas industry. Cost of drilling can be increased by issues such as hole enlargement or collapse, lost circulation of drilling fluids, and unintentionally induced fractures. An integrated geomechanical model can be used, prior to drilling the wellbore, to help identify and avoid these costly occurrences. A detailed analysis of datasets from well log data were used to create a 1-D geomechanical model for the Fasken C Ranch, Fee BI #307 well. Calculated geomechanical curves were generated as inputs and a wellbore stability model was created determining breakout and loss thresholds for the well. The model was able to accurately predict intervals of potential wellbore breakout, as well as estimate a potential fluid weight window used for optimal drilling parameters through identified problematic section of stratigraphy. Predicting these thresholds builds confidence in the planned drilling parameters. It allows for cost effective decisions, minimizing the risk of problematic intervals in the drilling process. It also suggest a safe casing depth for an intermediate casing shoe based on the breakout thresholds. Developing pro-active approaches to wellbore instability can save capital in the field development and lead to further study utilizing the calculated geomechanical variables.

TABLE OF CONTENTS

DEDICATION	1
ACKNOWLEDGEMENT	2
ABSTRACT	3
TABLE OF CONTENTS.....	4
LIST OF FIGURES	7
LIST OF TABLES.....	12
CHAPTER I: INTRODUCTION	13
2.1 Elastic Properties	17
2.1.1 Static Properties vs Dynamic Properties	17
2.1.2 Young's Modulus (E).....	18
2.1.3 Poisson's Ratio (ν)	19
2.1.4 Shear Modulus (G).....	20
2.1.5 Bulk Modulus (K)	21
2.1.6 Derivatives of Elastic Properties.....	21
2.2 In Situ Stress Components	23
2.2.1 Overburden Stress (σ_v).....	25
2.2.2 Minimum Horizontal Stress (σ_h).....	25
2.2.3 Maximum Horizontal Stress (σ_H).....	28
2.2.4 Biot's Elastic Constant (α)	29
2.2.5 Stress Orientation.....	31
2.3 Rock Strength (UCS)	31
2.3.1 Correlations of UCS	32
2.3.2 Friction Angle (ϕ)	35
CHAPTER III: LITERATURE REVIEW	38
3.1 Pore Pressure (P_p).....	38
3.1.1 Bower's Method.....	38
3.1.2 Eaton's Method.....	40
3.1.3 Pore Pressure from Well Logs	42
3.2 Failure Criteria and Mechanisms	43
3.2.1 Mohr Coulomb.....	44

3.2.2 Mogi Coulomb.....	45
3.2.3 Modified Lade.....	47
3.2.4 Overall Comparisons.....	48
CHAPTER IV: GEOMECHANICAL MODEL FEE BI #307	49
4.1 Study Area.....	49
4.2 Well Overview.....	52
4.2 Data Gathering.....	54
4.2.1 Log Data.....	55
4.2.2 Core Data.....	56
4.2.3 Offset Data.....	58
4.2.4 Image Log.....	59
4.2.5 Quality Control	61
4.3 Mechanical Earth Model Workflow	62
4.4 Overburden.....	62
4.5 Elastic Properties	64
4.5.1 Young’s modulus (E).....	64
4.5.2 Poisson’s Ratio (ν).....	65
4.5.3 Bulk Modulus (K).....	66
4.5.4 Shear Modulus (G).....	67
4.6 Rock Streangth (UCS).....	68
4.7 Facies Breakdown.....	72
4.8 Geologic Formation Tops.....	76
4.9 Pore Pressure (P_p).....	78
4.10 Minimum Horizontal Stress (σ_h).....	80
4.11 Loss and Breakout Thresholds.....	82
4.12 Cross Plots	87
CHAPTER V.....	90
5.0 DISCUSSION AND CONCLUSIONS.....	90
5.1 Recommendations for Future Work.....	94
5.2 Image of Final Model.....	95
REFERENCES.....	96
APPENDIX.....	106

Appendix A: List of Equations	106
Appendix B: List of Variables	108
Appendix C: Conversion Tables	112
Appendix D: Facies Python Code.....	113

LIST OF FIGURES

Figure 1: Oil and gas production in Ector Co., TX on July 28th, 2020, for the month of July 2020 (ShaleXP.com, 2020).....	13
Figure 2: Average price of WTI crude oil for the month of July 2020, portraying ~\$41.01 average price per barrel of oil (Rotrends.net, 2020).....	14
Figure 3: In-situ principal stress example for a drilled vertical well.....	24
Figure 4: Representation of a diagnostic fracture injection test and the corresponding points of interest one can glean from it. This includes a minimum horizontal stress point, a pore pressure point, a FIP (fracture initiation point), as well as an ISIP (initial shut in pressure) point.	27
Figure 5: Graphical representation of estimation of Biot based on lithology and effective porosity of that lithology from log (Crain, 2000).....	30
Figure 6: Internal friction angle correlations compared to test data (Chang et al., 2006).	36
Figure 7: Graphical representation of determining friction angle from gamma ray data (Albukhari et al., 2018).....	37
Figure 8: Overburden and pore pressure gradients and effective stress (Formento, 2004).	41
Figure 9: Pore pressure, overburden stress, and effective stress versus the true vertical depth (TVD) in a deep water well in the Gulf of Mexico (Zhang, 2013).....	43
Figure 10: Example of Mohr Circle with arrow demonstrating the moment of failure, modified from (Zhang, 2013).....	44

Figure 11: Map view of the study area in Fasken C Ranch. Red star indicated the Fee BI #307 well used in the model and the other two wells are offsets used to correlate tops. ...49

Figure 12: Super sequence correlation from a global, to basinal, to well log level portraying major geologic formations and their correlative lithologies from Ulmo (2018).
.....51

Figure 13: Image of the well location of Fee BI #307 well location from the Texas Railroad Commission (RRC, 2020).52

Figure 14: Different wireline logs along with computed well log curves, and machine learning facies of Fee BI #307 well. The computed well logs curves include, Young’s modulus (*YME*), Poisson’s ratio (*PR*), bulk modulus (*BM*), shear modulus (*SM*), uniaxial compressive strength (*UCS*). The available core measured data points are posted on the corresponding well log curve track. Notice that the well log velocities, and density are approximately same as their core measured values.57

Figure 15: Log curve of caliper for the offset Fee BM #1 SWD well highlighting potential borehole breakout intervals of borehole enlargement.....59

Figure 16: Sections of the image log taken for the Fee BI #307 well highlighting drilling induced fractures (DIF).....60

Figure 17: Processed FMI rosette provided by Fasken portraying the plane for minimum horizontal stress direction of 80° - 90° / 260°-270°.61

Figure 18: Example workflow used to build the wellbore stability model for the Fee BI #307 well.....62

Figure 19: Example of calculated overburden curve.....63

Figure 20: Different well log curves of Fee BI #307 well, between the depths of 9250 ft. (base of lower Spraberry) to 10150 ft. (Strawn formation). The last track of the well log display panel shows the computed Young’s modulus curve as along with core measured Young’s modulus data points.....65

Figure 21: Different well log curves of Fee BI #307 well, between the depths of 9250 ft. (base of lower Spraberry) to 10150 ft. (Strawn formation). The last track of the well log display panel shows the computed Poisson’s ratio curve as along with core measured Poisson’s ratio data points in log view along with the facies model.66

Figure 22: Different well log curves of Fee BI #307 well, between the depths of 9250 ft. (base of lower Spraberry) to 10150 ft. (Strawn formation). The last track of the well log display panel shows the computed bulk modulus curve as along with core measured bulk modulus data points in log view along with the facies model.67

Figure 23: Different well log curves of Fee BI #307 well, between the depths of 9250 ft. (base of lower Spraberry) to 10150 ft. (Strawn formation). The last track of the well log display panel shows the computed shear modulus curve as along with core measured shear modulus data points in log view along with the facies model.68

Figure 24: Three calculated *UCS* curves with quality control data points from core.70

Figure 25: Gamma ray log curve of Fee BI #307 well, between the depths of 9250 ft. (base of lower Spraberry) to 10150 ft. (Strawn formation). The last track of the well log display panel shows the computed *UCS* curve as along with core measured *UCS* data points in log view along with the facies model.71

Figure 26: Printed optimized facies classification accuracy percent for the Fee BI #307 facies SVM generation script.....	72
Figure 27: Printed log view with facies column using python for the Fee BI #307 well.	73
Figure 28: Zoomed in view of all geomechanical logs along with corresponding facies column.	74
Figure 29: Facies classification key for calculated facies used on the Fee BI #307 well in this model.....	75
Figure 30: Map view, with scale, of the correlated geologic tops on the Fasken C Ranch dataset, including the Fee BI #307 well used in this model.....	76
Figure 31: Cross section view of the geologic tops on the Fasken C Ranch dataset, including the Fee BI #307 well used in this model.	77
Figure 32: Associated depths of formation tops correlated on the Fasken C Ranch dataset, including the Fee BI #307 well used in this model.....	78
Figure 33: Visualization of pore pressure and overburden calculated curves used in this model. Units is psi.	79
Figure 34: Visualization of minimum horizontal stress calculated curve. Units is psi. ...	81
Figure 35: Visualization of calculated loss threshold curve. Threshold units in ppg.	83
Figure 36: Visualization of calculated breakout threshold curve, safe mud weight window, and accompanying examples of wellbore complication risks.	84
Figure 37: Example of necessary curves to run a Mohr Coulomb, Mogi Coulomb, and modified Lade breakout curve using the wellbore stability modeling module used in this model.	85

Figure 38: Example of calculated breakout threshold, loss threshold, and safe mud weight windows; Along with offset caliper data, and facies logs, to help quality control the calculated breakout and loss thresholds.	86
Figure 39: Cross plot of compressional and shear sonic log data colored by facies with an r^2 value of 0.94.	88
Figure 40: Cross plot of <i>UCS</i> and Young’s modulus colored by facies with an r^2 value of 0.90 and attributed best fit curve values.	88
Figure 41: Cross plot of Young’s modulus and Poisson’s ratio colored by facies.	89
Figure 42: Cross plot of <i>UCS</i> and Poisson’s ratio colored by facies.	89
Figure 43: Example of calculated breakout threshold, loss threshold, and safe mud weight windows; Along with offset caliper data, and facies log, visualizing the potential problematic intervals while drilling. Thresholds units in ppg.	91
Figure 44: Example of zoomed in view of full model demonstrating accurate depictions of breakout and loss curve trends in relation to logs and facies curves.....	92

LIST OF TABLES

Table 1: Table showing elastic properties and their relationships to each other (Mavko et al., 2009).	22
Table 2: List of basic lithologic rock types and the corresponding rock strength estimations (Zhang, 2020).	33
Table 3: Various correlations for <i>UCS</i> and log based curves, red boxed equations used in analysis (Najibi et al., 2014). V_P is in km/s, E is in GPa, and <i>UCS</i> is in MPa.....	34
Table 4: Various correlations for <i>UCS</i> and log based curves, red boxed equations used in analysis (Zhang, 2020). V_P is in km/s, E is in GPa, ρ is in g/cm^3 , and <i>UCS</i> is in MPa. ...	34
Table 5: Examples of lab calculated correlations of internal friction angle for shales and sands (Chang et al., 2006). V_P is in km/s.	35
Table 6: Surface hole location and well information for Fee BI #307 well.....	53
Table 7: Surface hole location and well information for Fasken ‘32’ #1 well.....	53
Table 8: Surface hole location and well information for Fasken ‘32’ #1 well.....	54
Table 9: Table describing the available log data, aliasing, and start depths of the digital log data for the Fee BI #307 well.	55
Table 10: Table describing the available core data points for the Fee BI #307 well.	56
Table 11: Table describing the surface location and well data for the Fee BM #1 SWD well.	58
Table 12: Table referencing conversions to and from metric and imperial unit of measurement systems (Zhang, 2011).	112

CHAPTER I: INTRODUCTION

In July 2020, shale exp.com reported Ector County, TX as the #44 ranked oil producing county nationally; producing over 1.5 million barrels of oil (Figure 1). That is equivalent to over 63 million dollars in production for one month of completing wells, at 42 dollars per barrel average on July 27th, 2020 (Figure 2). Given the dollar value of oil production, it is both crucial and prudent to garner as much information as possible to optimize the capital used when operating wells in this area of study. One such path to achieve this goal is using geomechanical modeling. In understanding how the rock breaks one is able to glean much insight into components of the reservoir being produced.

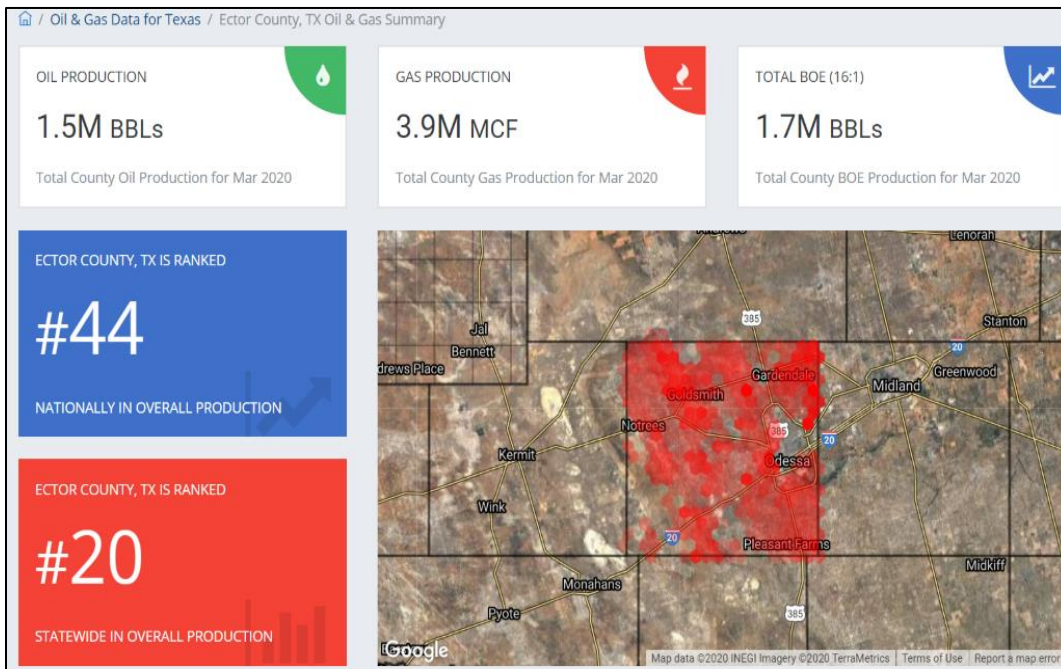


Figure 1: Oil and gas production in Ector Co., TX on July 28th, 2020, for the month of July 2020 (ShaleXP.com, 2020)



Figure 2: Average price of WTI crude oil for the month of July 2020, portraying ~\$41.01 average price per barrel of oil (Rotrends.net, 2020).

Geomechanics is a diverse field of study with many applications, while this thesis focuses on building a wellbore stability model, there is a myriad of other research done in the Permian Basin using geomechanics. Zheng et al. (2018) researched production based stress changes and their impact on wellbore stability. They demonstrated that as depletion and reservoir pressure changes with field development, so will the effective principal stresses. This particular is insightful due to the years of vertical well production in the Permian Basin. Wang and Weijermars (2019) specifically researched failure criteria in a lateral wellbore sense; observing elastically anisotropic shales and how they fail. Since

horizontal drilling is a new normal, this has implications on both drilling the well, understanding when the surrounding rock may collapse and fail, along with completing the well, in understanding pressure and principal stresses needed to break and drain the reservoir.

Specifically, in the Permian Basin, Ouenes et al. (2016) discussed the use of geomechanical modeling to quantify natural fractures and well performance in Reagan County, TX. Their work catered to the lower Wolfcamp, analyzing fracture orientation and simulating hydraulic fracture stages, and viewing it from a micro seismic aspect utilizing geomechanical inputs. Kowan et al. (2017) utilized the same theories of this thesis calculating geomechanical properties from well logs to better analyze weak bedding planes and zones of under and over pressure that could lead to wellbore instability. They concluded that identifying geomechanical related hazards leads to more intelligent well design from the planning process.

While operators in Ector county, TX may have done some work using geomechanical parameters, there is no available publications of any geomechanically calculated curves in this county in Texas. Drilling wells can be costly. Garnering a greater understanding of the rock and the geomechanical properties around the wellbore lead to a more cost-effective drilling program. In understanding the potential wellbore breakout and loss thresholds one can minimize risk of hole collapse or fluid loss when drilling the well. This can be seen in work available from Schlumberger (2012), that gives more detail into basic wellbore stability theory and defines “risk based” geomechanical modeling that can be used in drilling the Wolfcamp Shale play.

The purpose of this study is to utilize the offset well datasets to build a working model that can determine “high risk” or “problematic” geologic intervals in the drilling process. By using geomechanical parameters, both measured and calculated, thresholds of potential wellbore breakout and losses will be determined. A calculated “safe” fluid weight window to optimize wellbore stability through the identified problematic section of stratigraphy will be recognized. By establishing the process and workflow of building the first model in the area, others will be able to utilize the dataset to further understand and improve the initial model built.

CHAPTER II: GEOMECHANICAL PROPERTIES

2.1 Elastic Properties

The elastic properties of the rock are required to be calculated in order to build a 1D mechanical earth model from well data including: Young's modulus (E), shear modulus (G), bulk modulus (K), and Poisson's ratio (ν). They must be either obtained through laboratory testing on core or derived using sonic well log measurements of compressional and shear waves along with a bulk density measurement (Knöll, 2016). While more accurate, the core measurements are assumed to be a more static property, while derived calculations are called dynamic properties (Słota-Valim, 2015). It is common to calculate the dynamic elastic properties for use in modelling due the expensive and time consuming nature of running laboratory tests to obtain the static elastic property measurements from core. That fact, coupled with the circumstance of only being able to pressure and measure triaxial strain on core once per sample, lends credence to the use of an approach utilizing the calculated dynamic elastic properties when building a mechanical earth model.

2.1.1 Static Properties vs Dynamic Properties

In an ideal world one would always use the static properties when determining the elastic properties of a rock. Given the less than ideal costs and time associated with the lab work required to obtain the static properties, it is commonplace to derive these values using sonic well log measurements of compressional and shear waves along with a bulk density measurement (Fei et al., 2016). It is possible to determine dynamic values

for Young's modulus and Poisson's ratio from well log data. Dynamic Young's modulus differs from the static variant in that it is always a greater value under identical laboratory conditions (Fei et al., 2016). Dynamic Poisson's ratio is relatively similar to the static variant, it may occasionally run higher (Fei et al., 2016). For details regarding pressure and temperature variances and their corresponding logarithmic and linear relationships, Fei et al. (2016) describes a statistical breakdown of each in turn.

2.1.2 Young's Modulus (E)

Young's modulus expresses the relationship between applied longitudinal stress and the longitudinal deformation/strain in a material. The modulus is a measure of the stiffness of a material (Słota-Valim, 2015). It can be thought of as the modulus of stiffness. It is expressed by the Equation 1 and Equation 2 below and is measured in units of pressure; Pa, bar, or psi (1 Pa = 10⁻⁵ bar = 0.000145038psi). Please note, Appendix A is a reference to all formula used in this thesis. Appendix B is a list of the variables in the sequential order they appear.

$$\textit{Static: } E = \sigma / \varepsilon \quad (1)$$

where,

$\sigma = \textit{stress (psi)}$

$\varepsilon = \textit{strain}$

$$\textit{Dynamic: } E_{dyn} = \rho V_S^2 [(3V_P^2 - 4 V_S^2) / (V_P^2 - V_S^2)] \quad (2)$$

where,

$\rho = \text{bulk density (g/cm}^3\text{)}$

$V_S = \text{shear wave velocity (ft/sec)}$

$V_P = \text{compressional or primary wave velocity (ft/sec)}$

Or if one has calculated a shear modulus and Poisson's ratio curves Equation 3 can be used.

$$E_{dyn} = 2 * G * (1 + \nu) \quad (3)$$

where,

$G = \text{bulk modulus (psi)}$

$\nu = \text{Poisson's ratio}$

2.1.3 Poisson's Ratio (ν)

Poisson's ratio expresses the relationship between transverse strain to axial strain or the deformation of a material (Słota-Valim, 2015). If strain is negative it is a product of stretching from axial tension or if there is a compression, the strain is positive. One way to think about Poisson's ratio is how flexible a material is. The higher the value, the more flexible the material. For example, if one was to pinch a gummy bear it is much more flexible than when compared to a cork. Therefore, the gummy bear has a higher Poisson's ratio and that of the cork is much lower. Poisson's ratio (ν) is expressed by Equation 4 and Equation 5 below.

$$\textbf{Static: } \nu = \varepsilon_{trans} / \varepsilon_{axial} \quad (4)$$

where,

ε_{axial} = axial strain

ε_{trans} = transverse strain

$$\textbf{Dynamic: } \nu_{dyn} = (V_P^2 - 2*V_S^2) / (2(V_P^2 - V_S^2)) \quad (5)$$

2.1.4 Shear Modulus (G)

The shear modulus expresses the ratio of shear stress to shear strain (Archer and Rasouli, 2012). It is commonly referred to as the modulus of rigidity of a material. It can describe how the material reacts to shear stress. The larger the value of the shear modulus the more rigid the material (Słota-Valim, 2015). It is expressed by Equation 6 or Equation 7 in units of pressure; Pa, bar or psi.

$$G = [F/A] / [\Delta x/l] \quad (6)$$

where,

F = the shear force applied

A = the cross-sectional area of material parallel to the applied force vector

Δx = shear displacement

l = initial length

$$G = \rho V_S^2 \quad (7)$$

2.1.5 Bulk Modulus (K)

The bulk modulus expresses the resistance of the material to change in volume when exposed to compression from all every direction (Słota-Valim, 2015). Think of it as the modulus of resistance, or how resistant the substance is to compression (Kadhim et al., 2016). Since bulk modulus deals with compressibility of a given volume of material it also is one of the modulus that affect a given unit of volume (Fei et al., 2016). It is expressed by Equation 8 and Equation 9 in units of pressure; Pa, bar or psi.

$$K = \Delta P / [\Delta V/V] \quad (8)$$

or,

$$K = \rho (V_P^2 - (4/3) V_S^2) \quad (9)$$

where,

$\Delta P =$ change of pressure

$\Delta V =$ change in volume

$V =$ initial volume of material

2.1.6 Derivatives of Elastic Properties

All elastic properties of materials are interrelated and can be mathematically derived if the preferable data is not available (Mavko et al., 2009). Table 1 shows the mathematical relationships one can use to derive certain properties if others are known, or calculated using other means such as sonic data from well logs.

	(V_P, V_S)	(μ, λ)	$(E, \lambda)^\dagger$	(E, μ)	(K, λ)	(K, μ)	(K, E)
P-wave velocity $V_P =$	V_P	$\sqrt{\frac{\lambda+2\mu}{\rho}}$	$\sqrt{\frac{E-\lambda+\lambda}{2\rho}}$	$\sqrt{\frac{\mu(E-4\mu)}{\rho(E-3\mu)}}$	$\sqrt{\frac{3K-2\lambda}{\rho}}$	$\sqrt{\frac{K+\frac{4}{3}\mu}{\rho}}$	$\sqrt{\frac{3K(3K+E)}{\rho(9K-E)}}$
S-wave velocity $V_S =$	V_S	$\sqrt{\frac{\mu}{\rho}}$	$\sqrt{\frac{E-3\lambda+\lambda}{4\rho}}$	$\sqrt{\frac{\mu}{\rho}}$	$\sqrt{\frac{3(K-\lambda)}{2\rho}}$	$\sqrt{\frac{\mu}{\rho}}$	$\sqrt{-\frac{3EK}{\rho(E-9K)}}$
Velocity ratio $\Gamma =$	$\frac{V_P}{V_S}$	$\sqrt{\frac{\lambda+2\mu}{\mu}}$	$\sqrt{\frac{3E+3\lambda+\lambda}{2E}}$	$\sqrt{\frac{E-4\mu}{E-3\mu}}$	$\sqrt{\frac{\frac{4}{3}\lambda-2K}{\lambda-K}}$	$\sqrt{\frac{K+\frac{4}{3}\mu}{\mu}}$	$\sqrt{\frac{E+3K}{E}}$
1st Lamé parameter $\lambda =$	$\rho(V_P^2 - 2V_S^2)$	λ	λ	$\frac{\mu(E-2\mu)}{3\mu-E}$	λ	$K - \frac{2\mu}{3}$	$\frac{3K(3K-E)}{9K-E}$
Shear modulus $\mu =$	ρV_S^2	μ	$\frac{E-3\lambda+\lambda}{4}$	μ	$\frac{3(K-\lambda)}{2}$	μ	$\frac{3KE}{9K-E}$
Young's modulus $E =$	$\frac{\rho V_S^2(3V_P^2 - 4V_S^2)}{V_P^2 - V_S^2}$	$\frac{\mu(3\lambda+2\mu)}{\lambda+\mu}$	E	E	$\frac{9K(K-\lambda)}{3K-\lambda}$	$\frac{9K\mu}{3K+\mu}$	E
Bulk modulus $K =$	$\rho(V_P^2 - \frac{4}{3}V_S^2)$	$\lambda + \frac{2\mu}{3}$	$\frac{E+3\lambda+\lambda}{6}$	$\frac{E\mu}{3(3\mu-E)}$	K	K	K
Poisson's ratio $\nu =$	$\frac{V_P^2 - 2V_S^2}{2(V_P^2 - V_S^2)}$	$\frac{\lambda}{2(\lambda+\mu)}$	$\frac{-E-\lambda+\lambda}{4\lambda}$	$\frac{E}{2\mu} - 1$	$\frac{\lambda}{3K-\lambda}$	$\frac{3K-2\mu}{2(3K+\mu)}$	$\frac{3K-E}{6K}$
P-wave modulus $M =$	ρV_P^2	$\lambda + 2\mu$	$\frac{E-\lambda+\lambda}{2}$	$\frac{\mu(4\mu-E)}{3\mu-E}$	$3K - 2\lambda$	$K + \frac{4\mu}{3}$	$\frac{3K(3K+E)}{9K-E}$

Table 1: Table showing elastic properties and their relationships to each other (Mavko et al., 2009).

Table 1 can be especially useful if one has access to limited data. There are also laboratory tested relationships for various lithologies if only a monopole sonic logging run with compressional or primary wave velocity data is available (Milovac, 2009). An example is Equation 10 used for sandstone below.

$$V_S = 0.8042 * V_P - 855.9 \quad (10)$$

These conversions are useful tools given limiting data conditions to help build a mechanical earth model from well log data.

2.2 In Situ Stress Components

In situ stresses and rock mechanics properties play a key role in the assessment of wellbore design and execution (Aadnøy and Looyeh, 2019b). Understanding what stresses effect the rock at any given point is crucial in determining how rock will break. There are three perpendicular axis of stresses at any given point in a material in the subsurface, vertical stress or overburden stress (σ_v), minimum horizontal stress (σ_h), and maximum horizontal Stress (σ_H) as seen in Figure 3 below (Aadnøy and Looyeh, 2019b).

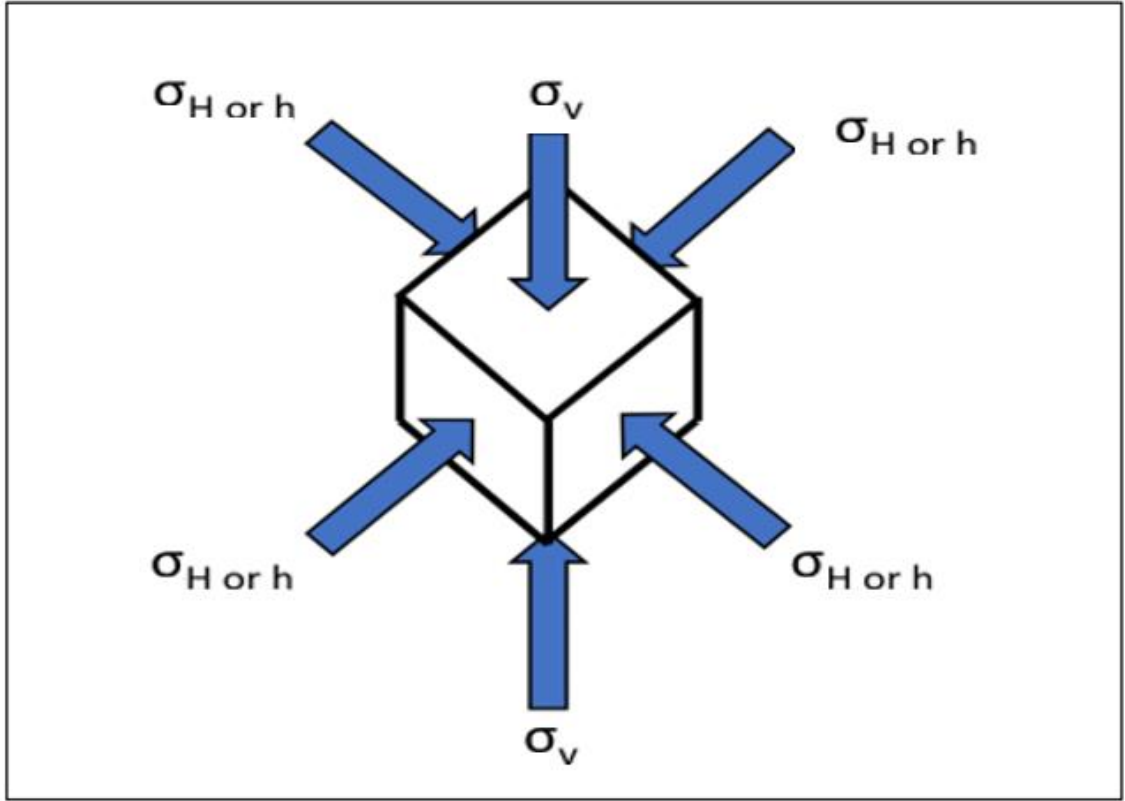


Figure 3: In-situ principal stress example for a drilled vertical well.

It is vital to also realize that these three stresses may affect the wellbore or rock differently when studying it from a vertical to horizontal capacity depending on how the well was drilled. In general all three principal stresses are not hydrostatic, i.e. all have different magnitudes at any given wellbore direction (Aadnøy and Looyeh, 2019a).

This thesis built a 1D mechanical earth model using vertical well data, meaning the stress components were only studied from a vertical wellbore design perspective. The subsequent sections 2.2.1 – 2.2.5 will provide details on each stress component.

2.2.1 Overburden Stress (σ_v)

Overburden stress or vertical stress is defined as the pressure exerted on a material at a given depth due to the total mass of the rocks and/or fluids above it (Aird, 2019). The simple way to consider overburden is just how much material is above, that is compacting the rock in a vertical capacity due to weight and gravity. It is possible to interpolate overburden over an interval if two vertical stress points are measured from lab tests. This is a common practice in computing overburden stress when faced with a lack of data availability (Aird, 2019). Overburden stress can be calculated using Equation 11 and requires knowledge of depth/thickness and the bulk density of the given material to calculate from log-based data sets.

$$\sigma_v = \sum_i \rho_i h_i g \quad (11)$$

where,

g = is the gravitational constant (32.175 ft/s²)

h_i = the vertical thickness of the i^{th} rock layer (ft)

ρ_i = the density of the i^{th} rock layer (lb_m/ft³)

2.2.2 Minimum Horizontal Stress (σ_h)

Minimum horizontal stress is often thought of as “closure stress” as it directly relates to the closure gradient of fractured pores made while drilling or fracking (Belyadi and Belyadi, 2019). During drilling, there is a specific pressure exerted on the surrounding rock that the fluid column of the hole is directly related to. This pressure of

the fluid column must not exceed or be less than that of the surrounding pressure or wellbore instability will occur. As the drill bit breaks the rock drilling down vertically, the fluid column must be held at a specific pressure gradient to balance all three principal stress components. We define this as the hydrostatic pressure of the fluid column (Belyadi and Belyadi, 2019). Breakout pressure is defined by the maximum and minimum horizontal stresses, pore pressure, and rock strength (Belyadi and Belyadi, 2019). If the pressure of the fluid column exceeds the breakout pressure of the surrounding rock, it will break down and push the fluid out into the surrounding formation, resulting in mud losses in the hole. Minimum horizontal stress can be obtained by running a diagnostic fracture injection test (DFIT) (Figure 4).

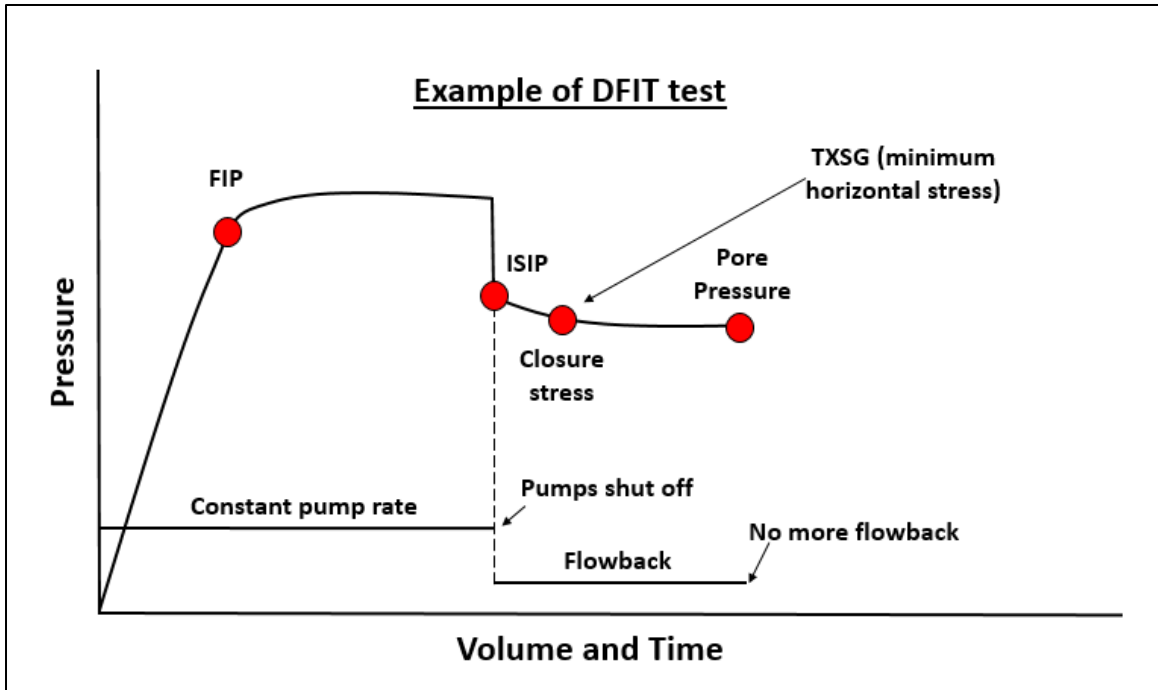


Figure 4: Representation of a diagnostic fracture injection test and the corresponding points of interest one can glean from it. This includes a minimum horizontal stress point, a pore pressure point, a FIP (fracture initiation point), as well as an ISIP (initial shut in pressure) point.

It is also worth noting that minimum horizontal stress can be calculated using isotropic or anisotropic components depending on your reservoir system and deposition as defined below in Equation 12 and Equation 13 from Zahiri et al. (2019).

$$\sigma_h = [(v/1 - v) \sigma_v] + [(1 - 2v/1 - v)P_p \alpha] + [(E/1 - v^2) \epsilon_y] + [(E v/1 - v^2) \epsilon_x] \quad (12)$$

where,

P_p = pore pressure (psi)

α = Biot elastic constant

$\varepsilon_y = \text{vertical strain}$

$\varepsilon_x = \text{lateral strain}$

or,

$$\text{Isotropic } \sigma_h = (v / 1 - v)(\sigma_v - \alpha_v P_p) + \alpha_H P_p + \sigma_{tect} \quad (13)$$

where,

$\alpha_v = \text{Biot elastic constant (vertical)}$

$\alpha_H = \text{Biot elastic constant (horizontal)}$

$\sigma_{tect} = \text{tectonic stress (MPa)}$

2.2.3 Maximum Horizontal Stress (σ_H)

Maximum horizontal stress is more difficult to calculate and is often considered the most challenging component of the stress regimes to derive accurate values (Knöll, 2016). Using measurements of pore pressure, rock strength, vertical stress, minimum horizontal stress, and the tectonic stress it is possible to derive the maximum horizontal stress using Equation 14, however, tectonic stress is exceedingly difficult to determine and is generally estimated (Snee and Zoback, 2016).

$$\sigma_H = [(v / 1 - v) * (\sigma_v - P_p \alpha)] + P_p \alpha + \sigma_{tect} \quad (14)$$

It is also possible to estimate the maximum horizontal stress from image logs, friction limit to stress data, caliper data, and drilling induced fracture data (DIF) (Han et al., 2019).

The estimated maximum horizontal stress values should always be greater than the minimum horizontal stress values. If it is not possible to calculate maximum

horizontal stress due to lack of data one can also assume a value equal to minimum horizontal stress with the addition of a gradient of 0.1 psi/ft (Belyadi and Belyadi, 2019); while not wholly accurate, it at least is valid in principle.

2.2.4 Biot's Elastic Constant (α)

Biot's constant is a direct relationship of porosity, permeability, clay content, grain contact, grain strength, overburden pressure, and bulk modulus (Biot and Willis, 1957). In simpler terms defined in Crain (2000), it is the ratio of the volume change of fluid filled pores in relation to the volume change when fluid is free to move about the pore space. The matrix volume of material needs some porosity or the Biot's elastic constant will be zero because there will be no change in volume. Biot's elastic constant is one of the more difficult variables to calculate and derive due to lack of sample data available for laboratory testing and the potential heterogeneity of the material involved and the underlying volume of pore space, fluid content, and permeability variables of the given system. For example, if one visualizes a very thin, one-millimeter beds of a porous limestone, interbedded with tight clays, it becomes easy to see how it would be difficult to determine the proper volumes of porosity relationships to get an accurate Biot's elastic constant over a one foot sample interval. Equations 15-17 are used to determine Biot's elastic constant from well log data; and using Figure 5 it is possible to estimate Biot's constant with an estimated effective porosity of a known rock or assumed lithology.

$$\alpha = 1 - (K_b / K_m) \quad (15)$$

where,

$K_b = \text{bulk modulus of base material (g/cm}^3\text{)}$

$K_m = \text{bulk modulus of rock matrix (g/cm}^3\text{)}$

$$K_b = \rho * (1 / (DTC^2) - (4/3) * (1 / (DTS^2))) \quad (16)$$

$$K_m = \rho_m * (1 / (DTC^2) - (4/3) * (1 / (DTS^2))) \quad (17)$$

where,

$DTC = \text{compressional wave travel time } (\mu\text{s,m)}$

$DTS = \text{shear wave travel time } (\mu\text{s,m)}$

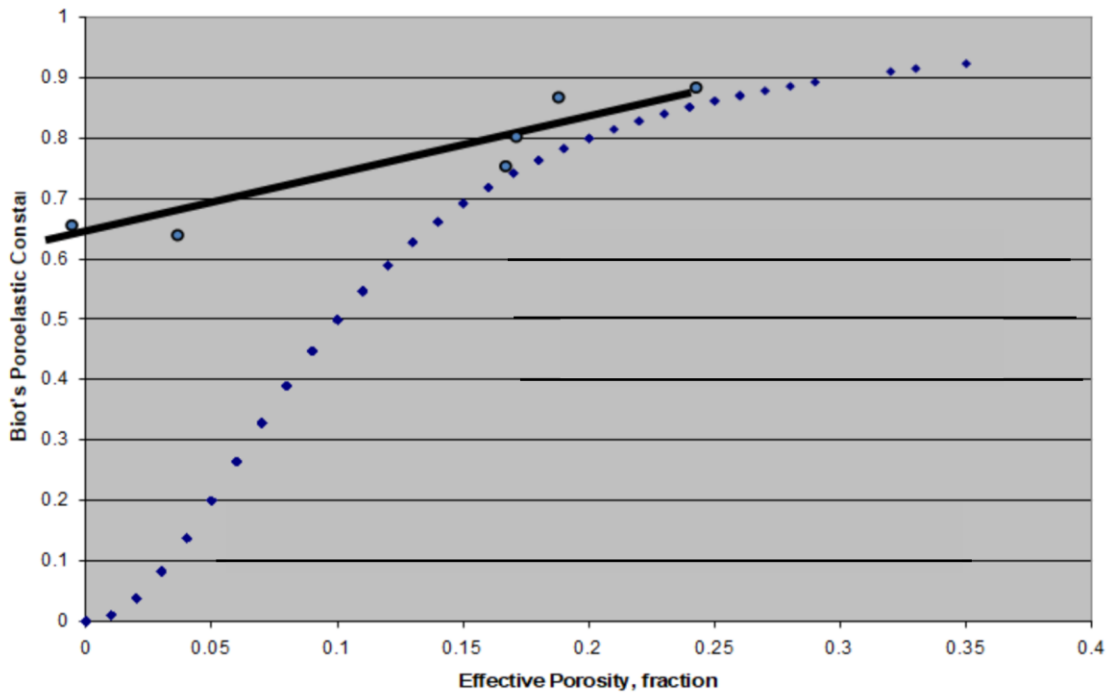


Figure 5: Graphical representation of estimation of Biot based on lithology and effective porosity of that lithology from log (Crain, 2000).

2.2.5 Stress Orientation

Determining the stress orientation of a given depositional setting is a crucial part in understanding the two main horizontal stress components since they are perpendicular to each other (Belyadi and Belyadi, 2019). The simplest way to estimate the direction of horizontal stress components is identifying the direction of borehole breakout from image logs of the given intervals of study. One can also use caliper logs, if at least a 4-arm caliper was used to identify the weakest direction of borehole instability and breakout (Haidary et al., 2015). Using either of these logs can give an understanding of where the borehole is the weakest and more prone to breakout. It can also help identify any anomalies of the weakest stress direction in different intervals. The direction that breakouts are observed is the minimum horizontal stress direction. Perpendicular to that is the maximum stress direction (Warner Jr and Holstein, 2007). This method for determining the minimum and maximum horizontal stress direction is used regularly assuming a vertical borehole, however, this can vary once the wellbore start to build angle and eventually becoming horizontal. This thesis will only focus on determining the stress orientation of the vertical borehole and does not enter into the curve and horizontal drilling realms of stress direction regimes and change.

2.3 Rock Strength (UCS)

Unconfined compressive strength (*UCS*) is the strength that describes the capacity of the rock to resist compressive stresses (Zhang, 2020). When testing for *UCS* in the lab, rock failure mechanisms are observed by performing triaxial or uniaxial tests on specific samples based on the suitable nature of the rock in question. This lab test can give a lot of

information but is used in the geomechanical realm for *UCS* and friction angle (ϕ) data points. Lab testing is always preferable to derived log calculations, however, is it not economical to test an entire well's worth of samples from core. Using laboratory testing, one can obtain good data points used to quality control test separate log-based calculations and correlations of *UCS*. Sections 2.3.1 and 2.3.2 will describe various methods for determining *UCS* from log and correlations as well as deriving friction angle from a gamma ray log and friction angle correlations.

2.3.1 Correlations of UCS

It is common to use known correlations of *UCS* and Young's modulus for a starting point if one has calculated known facies of logs and has a good calibration of Young's modulus for those logs. It is possible to use simple equations such as shown in Table 2 below if a pseudo lithology is determined, but it is recommended to calibrate your *UCS* curves further using petrophysical data (Knöll, 2016).

	UCS (MPa)	Field characteristics	Examples
Extremely strong	>250	Specimen can only be chipped with a geologic hammer	Fresh basalt, chert, diabase, gneiss, granite, quartzite
Very strong	100–250	Specimen requires many blows of a geological hammer to fracture it	Amphibolite, sandstone, basalt, gabbro, gneiss, granodiorite, limestone, marble, rhyolite, tuff
Strong	50–100	Specimen requires more than one blow to fracture it	Limestone, marble, phyllite, sandstone, schist, shale
Medium strong	25–50	Cannot be scraped or peeled with a pocket knife. Specimen can be fractured with a single blow from a geological hammer.	Claystone, coal, concrete, schist, shale, siltstone
Weak	2–25	Can be peeled with a pocket knife with difficulty. Shallow indentation made by firm below with point of a geological hammer.	Chalk, rocksalt, potash
Very weak	1–5	Crumbles under firm blows with point of a geological hammer, can be peeled by a pocket knife	Highly weathered or altered rock
Extremely weak	0.25–1	Indented by thumbnail	Stiff fault gouge

Table 2: List of basic lithologic rock types and the corresponding rock strength estimations (Zhang, 2020).

Table 3 and Table 4 are a full list of various equations to derive *UCS* from log based on lithology type and Young's modulus as an alternative to strictly lithology.

Lithology	Equation	Reference
Igneous and Metamorphic	$E_s = 1.263 E_d - 29.5$	King (1983)
Igneous and Metamorphic	$UCS = 4.31 \left(\frac{E_d}{10} \right)^{1.705}$	King (1983)
Sedimentary	$E_s = 0.74 E_d - 0.82$	Eissa and Kazi (1988)
Sedimentary	$\log(E_s) = 0.02 + 0.7 \log(\rho E_d)$	Eissa and Kazi (1988)
Sedimentary	$E_s = 0.018 E_d^2 + 0.422 E_d$	Lacy (1997)
Sedimentary	$UCS = 0.278 E_s^2 + 2.458 E_s$	Lacy (1997)
Soft Rocks	$UCS = 2.28 + 4.0189 E_s$	Bradford et al. (1988)
Hard Rocks ($E_s > 15$ Gpa)	$E_s = 1.153 E_d - 15.2$	Nur and Wang (1999)
Shale	$UCS = 0.77 v_p^{2.93}$	Horsrud (2001)
Shale	$E_s = 0.076 v_p^{3.23}$	Horsrud (2001)
Shale	$E_s = 0.0158 E_d^{2.74}$	Ohen (2003)
Mudstone	$E_s = 0.103 UCS^{1.086}$	Lashkaripour (2002)
Limestone	$E_s = 0.541 E_d + 12.852$	Ameen et al. (2009)
Limestone	$UCS = 2.94 \left(\frac{E_s^{0.83}}{\phi^{0.088}} \right)$	Asef and Farrokhrouz (2010)
Different Rocks	$UCS = 2.304 v_p^{2.43}$	Kilic and Teymen (2008)

Table 3: Various correlations for UCS and log based curves, red boxed equations used in analysis (Najibi et al., 2014). V_p is in km/s, E is in GPa, and UCS is in MPa.

Lithology	Equation	Reference
Shales	$UCS = 7.22E^{0.712}$	Chang et al. (2006)
Shales	$UCS = 23.524E^{0.4775}$	Horsrud, 2001
Sands	$UCS = 156318*(1/V_p)^{2.064}$	McNally (1987)
Sands	$UCS = (1.745*\rho *V_p^2)-21$	Moos et al. (1999)
Limestone	$UCS = (7682/V_p)^{1.82}/145$	Milizer and Stoll (1973)
Limestone & Dol	$UCS = 10^{(2.44+(109.14/V_p))}/145$	Golubev and Rabinovich (1976)
Limestone	$UCS = 3.67*V_p^{2.14}$	Najibi et al. (2015)

Table 4: Various correlations for UCS and log based curves, red boxed equations used in analysis (Zhang, 2020). V_p is in km/s, E is in GPa, ρ is in g/cm³, and UCS is in MPa.

Not all lithologic types of rock have a perfect correlative equation and it is important to try multiple variations based on the samples being studied and then compare back to laboratory testing results to obtain the most accurate and precise value for *UCS* (Adisornsupawat et al., 2011). One shale is not universal. A correlation of *UCS* based on a shale sample from the Gulf of Mexico may not be correlative to *UCS* of a shale sample from the North Sea (Table 3). Obtaining valid calculations for *UCS* can be difficult given all the preceding variables.

2.3.2 Friction Angle (ϕ)

The measure of the angle of internal friction (ϕ) is the measure of the ability of the rock to withstand a shearing stress (Aadnoy, 1998). It can be considered the angle observed between the normal force, and shearing force, during rock failure from a shearing stress. Like *UCS*, friction angle can be measured in a lab test as well as derived/correlated using log. Due to economic conditions friction angle is often estimated. Common equations used for estimation are observed in Table 5.

Lithology	Equation for internal friction angle	Reference
Shale	$\sin^{-1}((v_p - 1000)/(v_p + 1000))$	Lal (1999)
Sandstone	$57.8 - 105\phi$	Weingarten and Perkins (1995)

Table 5: Examples of lab calculated correlations of internal friction angle for shales and sands (Chang et al., 2006). V_P is in km/s.

This method is not perfect. Figure 6 portrays a graphical example of correlations using this method compared to lab data.

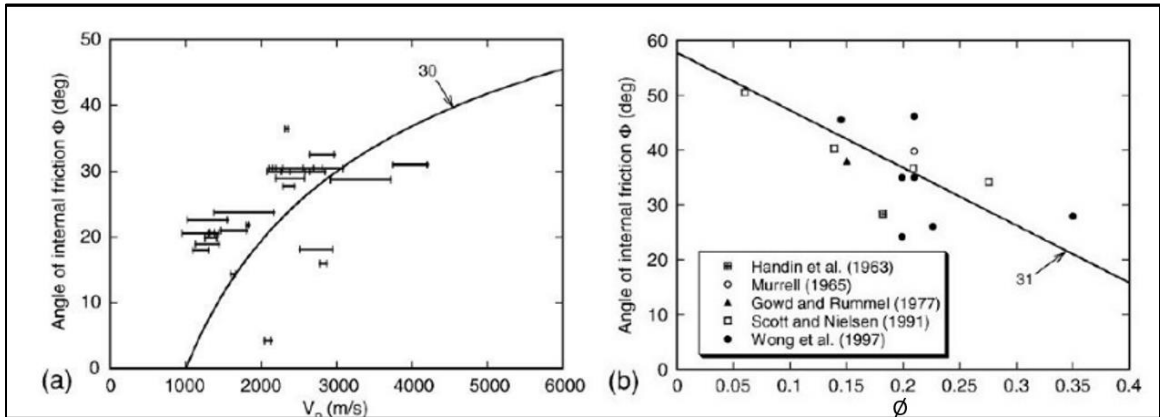


Figure 6: Internal friction angle correlations compared to test data (Chang et al., 2006).

There also exists an empirical correlation to determine friction angle (Kadyrov, 2013), found in the work by Albukhari et al. (2018). This method applied a cutoff to friction angle at certain API gamma ray readings as observed in Figure 7 below.

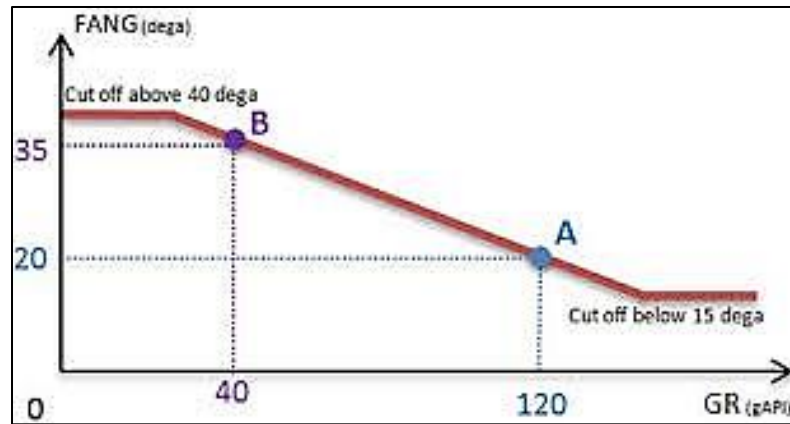


Figure 7: Graphical representation of determining friction angle from gamma ray data (Albukhari et al., 2018).

Due to potential rock having high friction angles, one may need to “force” the cutoffs in individual cases. This can then be quality control tested by laboratory data and the gamma ray API cutoffs can be altered accordingly (Albukhari et al., 2018).

CHAPTER III: LITERATURE REVIEW

3.1 Pore Pressure (P_p)

Pore Pressure (P_p) is the pressure of fluids within the pores of a rock unit, or the pressure exerted by a column of fluid (Schlumberger, 2020). This is important in geomechanics because accurately defining pore pressure of your reservoir helps in determining minimum horizontal stress and directly affects your loss threshold. Drilling through significant zones with low loss thresholds will cause serious risk to operations ranging from loss of mud to loss of wellbore integrity, fluid influx, pressure kicks, or blowout (Zhang, 2020). While there are methods for calculating pore pressure before drilling using log curves, it is always encouraged to incorporate varying observations from the field to better fine tune your model. Effects such as depletion, or water/CO₂ flooding for secondary/tertiary recovery, can greatly affect the pore pressure of a given interval, but can be easily overlooked when just using log based calculation (Zahiri et al., 2019). It is prudent to also look at field tests such as Leak Off Tests (LOTs) or Fracture Initiation Tests (FITs) that can help bring actual field data to quality control your pore pressure curves and give a baseline in a given section of rock (Zhang, 2020). Figure 4 from section 2.2.2 gives an example of how a FIT can be used. Sections 3.1.1 – 3.3.3 will review different methods for estimating pore pressure.

3.1.1 Bower's Method

Bowers (1995) devised a method to calculate the effective stresses from measured pore pressure data in shales, as well as the overburden stresses. He then analyzed the

corresponding sonic velocity data from the well logs and proposed that effective stress and sonic velocity has a power relationship Equation 18.

$$V_P = V_{ml} + C\sigma_v^B \quad (18)$$

where,

V_{ml} = compressional wave velocity at mud line (ft/s)

C and B = constants for calibration

Using the relationship from Equation 19, pore pressure can be derived.

$$Pp = \sigma_v - ((V_P - V_{ml})/C)^{1/B} \quad (19)$$

Be aware that using this method does have its pitfalls, it has been documented that this will lead to inaccurate pore pressures if uplift or unloading has occurred (Archer and Rasouli, 2012). If one believes unloading has occurred Bowers (1995) proposed the subsequent Equation 20.

$$Pp_{ulo} = \sigma_v - ((V_P - V_{ml})/C)^{U/B} * (\sigma_{max}^{1-U}) \quad (20)$$

where,

Pp_{ulo} = pore pressure in unloading (psi)

U = constants for calibration

σ_{max} = the estimated effective stress at the onset unloading (psi)

Rock that is poorly consolidated or unconsolidated may also lead to error and overestimation due to the sonic velocity differences (Rahimi, 2014). Bower's method is effective with exception to the above situations and can be used in many areas of study.

3.1.2 Eaton's Method

Eaton's method was originally developed for under compacted, over pressured, shales in the Gulf of Mexico (Eaton, 1975). He proposed the following Equation 21 that empirically relates compressional sonic transit time and overburden to pore pressure gradient.

$$P_p = \sigma_v - (\sigma_v - Pp_{ng}) * (\Delta t_n / \Delta t)^n \quad (21)$$

where,

Pp_{ng} = pore pressure of hydrostatic pressure (psi)

Δt = sonic delta time ($\mu\text{sec}/\text{m}$)

n = constant for calibration

This method does not take into account unloading effects and requires determination of the normal transit time. Eaton's method relies heavily on Terzaghi's equation of 1948 : Which states that if a rock is subjected to stress, the stress is opposed by the fluid pressure of pores in the rock body (Zhang, 2020).

This relationship demonstrates that effective stress sits somewhere between the overburden stress and the pore pressure. Figure 8 below supports the relationship.

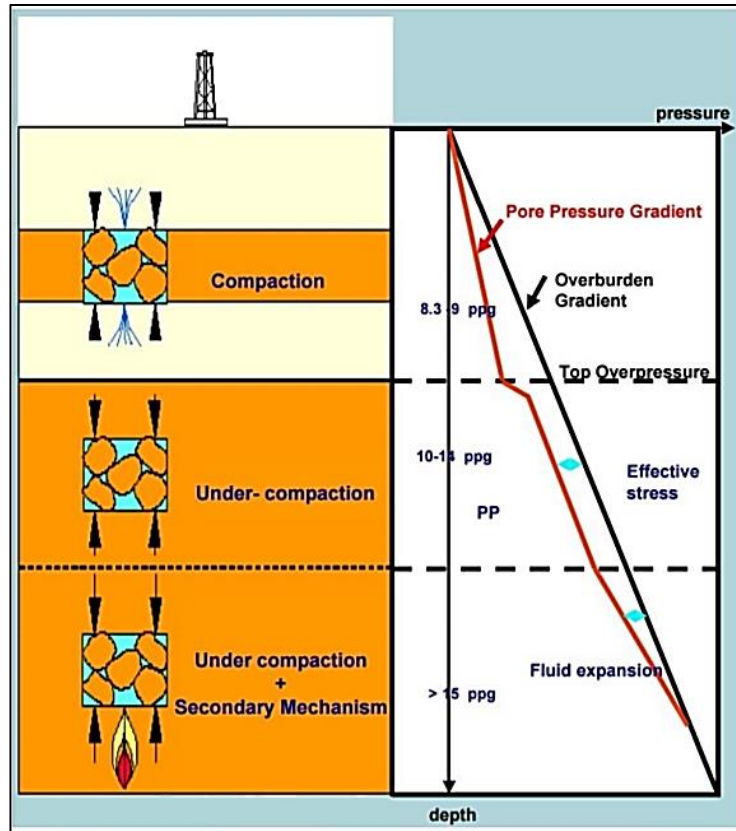


Figure 8: Overburden and pore pressure gradients and effective stress (Formento, 2004).

Once effective stress is understood then one can use resistivity and sonic well log data to estimate pore pressure using Eaton's relationship in Equation 22.

$$P_p = \sigma_v - (\sigma_v - G_{hyd} * TVD) * (V_{norm} - V_{comp})^n \quad (22)$$

where,

G_{hyd} = gradient of hydrostatic pressure (KPa/m)

V_{norm} = Velocity log value according to normal trend

V_{comp} = Velocity log value according to compaction trend

TVD = True Vertical Depth

3.1.3 Pore Pressure from Well Logs

Pore pressure from well logs is recognized based on the divergence of the log measurements from a normal compaction trend line (Aadnoy, 1998). The trend line being an assumption of the log's resistivity or sonic values if pore pressure was normal/hydrostatic. Hydrostatic pressure gradient is representative of a linear fitted trend line in low permeable beds (Aadnoy, 1998). One reason why quality control testing data to observed offset losses, leak off test data, and fracture initiation test data is so crucial, is they provide data points that the pore pressure gradient trend line must pass through for accurate pore pressure to be determined. Because pore pressure is a critical component of the loss threshold it can be accurately surmised that understanding the pore pressure gradient of a given well will greatly effect given acceptable mud weights to drill the given intervals with. This can lead to significant and costly problems drilling if pore pressure is underestimated. Figure 9 below demonstrates an example of a pore pressure plot. Keep in mind the fluid pressures in the wellbore must remain between overburden stress, and the normal pore pressure/pore pressure at hydrostatic. If at any point the interval of rocks pore pressure and pressure gradients change significantly outside the pressure of the fluid downhole it can lead to collapse.

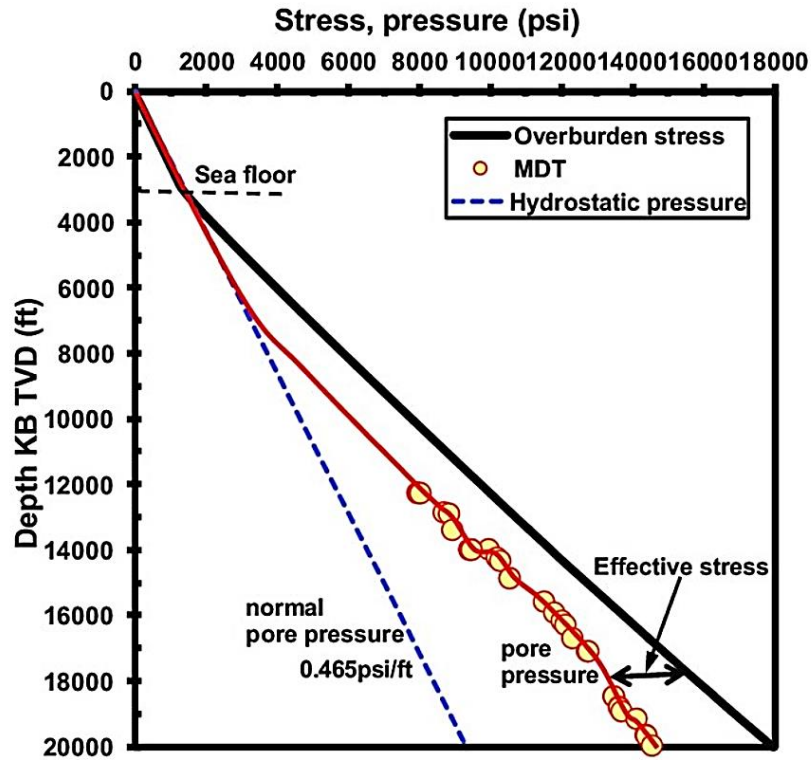


Figure 9: Pore pressure, overburden stress, and effective stress versus the true vertical depth (TVD) in a deep water well in the Gulf of Mexico (Zhang, 2013).

3.2 Failure Criteria and Mechanisms

Calculating an estimation of wellbore failure criteria is not a perfect science and there are numerous methods. Rock can fail in two ways around the wellbore during drilling operations. The first stress induced failure is shear failure; this is caused by too low a density of mud weight. The second type stress induced failure is tensile failure, this is caused by too heavy a density of mud weight (Al-Ajmi, 2012). Failure criteria is important due to wellbore stability, one does not want too small a pressure downhole to support the surrounding rock or the wellbore will start to break and crumble in the hole; at minimum this is revealed by hole enlargement on caliper, while severe consequences

include total hole collapse (Al-Ajmi, 2012). The next sections will go over different methods to calculate the failure criteria including Mohr Coulomb, Mogi Coulomb, and modified Laude.

3.2.1 Mohr Coulomb

The Mohr Coulomb failure criteria is the most commonly used due to its simplicity. It is a triaxial assumption meaning that in the test data ($\sigma_1 > \sigma_2 = \sigma_3$), or one ignores the intermediate principal stress (σ_2), as its assumed equal to the minor stress (σ_3). A common visual associated with Mohr Coulomb failure criteria is the Mohr circle as seen below in Figure 10.

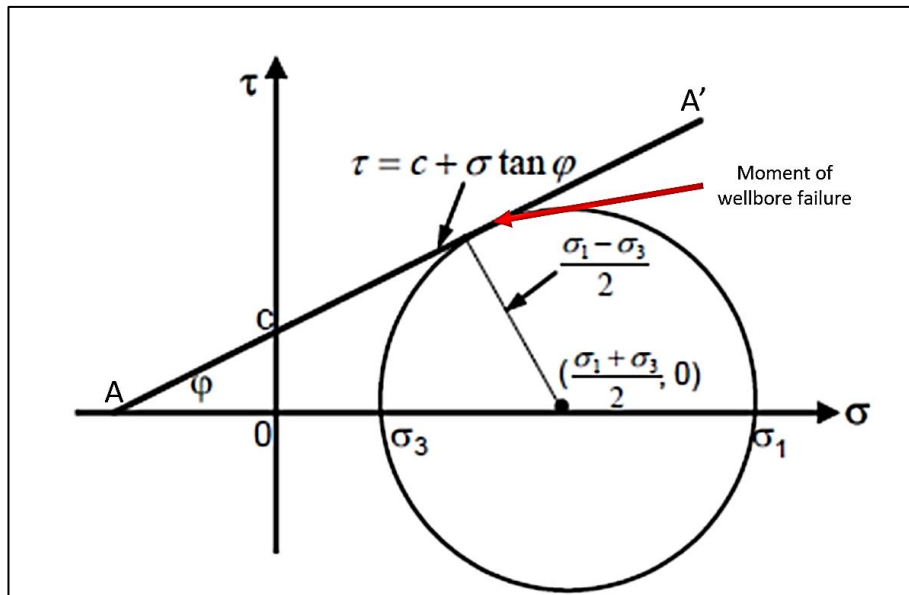


Figure 10: Example of Mohr Circle with arrow demonstrating the moment of failure, modified from (Zhang, 2013).

Using equation 23 one can view the circle as the wellbore maximum shear stress and the line A-A' as the “failure envelope” of acceptable wellbore stability. Once the circle touches the intersection point, wellbore failure and borehole collapse can occur.

$$\tau_{max} = (1/2)(\sigma_1 - \sigma_3) \quad (23)$$

where,

τ_{max} = the maximum shear stress

σ_1 = maximum principal stress

σ_3 = minimum principal stress

It is worth noting that the Mohr Coulomb method is known to underestimate the rock strength or overestimate the failure envelope in mud weight (Zhang et al., 2010). If using this method be aware it is potential to show more excess breakout compared to other methods such as Mogi Coulomb or modified Laude.

3.2.2 Mogi Coulomb

Mogi (1971) developed another method for describing rock failure. It is also a triaxial test like the Mohr Coulomb method, however, it develops a linear function to (σ_2) using polyaxial test data ($\sigma_1 > \sigma_2 > \sigma_3$). It deals with the (σ_2) stress slightly differently, as it takes it into account, rather than assumes it to be equal to the (σ_3). Mogi discovered through laboratory testing that strain energy as a frictional force is proportional to the octahedral shear stress and will increase by increasing (σ_2) until failure occurs. The linear relationship of his findings is seen below in Equation 24.

$$\tau_{oct} = a + b \sigma_{m2} \quad (24)$$

where,

τ_{oct} = max octahedral shear stress

σ_{m2} = intermediate effective mean stress

a = intersection of the line on τ_{oct} axis

b = the line's inclination

The variables (a) and (b) have a direct relation to the angle of internal friction that can be calculated from the Mohr Coulomb parameters q and C_o using Equations 25 – 27.

$$a = ((2\sqrt{2}) / 3) * (C_o / q) \quad (25)$$

$$b = ((2\sqrt{2}) / 3) * ((q-1) / (q+1)) \quad (26)$$

where,

C_o = cohesion (KPa)

$$q \text{ conversion} = (1 + \sin(\phi)) / (1 - \sin(\phi)) \quad (27)$$

Because Mogi Coulomb takes into account the intermediate stress variable but is also a linear equivalent to Mohr Coulomb in conventional triaxial stress test space, it can be thought of as an expansion on the Mohr Coulomb method in that triaxial space (Rahimi, 2014).

3.2.3 Modified Lade

Experimental observed from Lade (1977) concluded that for a cohesionless material, internal friction angle decreases with increasing normal stress. What became known as the modified Lade criterion first was developed by Ewy (1999). This method takes stress invariant parameters first and third stress invariants into account formulating the concept that as shear strength increases, so does the first stress invariant. It also assumes a material constant as zero. Ewy formulated a new measure for effective stress introducing the effective stress into the formula and the proposed Equations 28 -30 below.

$$(I_1^n)^3 / (I_3^n) = 27 + \eta \quad (28)$$

where,

I_1 = first stress invariant

I_3 = third stress invariant

η = material constant

$$I_1^n = (\sigma'_1 + S) + (\sigma'_2 + S) + (\sigma'_3 + S) \quad (29)$$

$$I_3^n = (\sigma'_1 + S) * (\sigma'_2 + S) * (\sigma'_3 + S) \quad (30)$$

where,

S = stress

Using modified Lade to determine a failure criterion has two main benefits (Rahimi, 2014). The first is that unlike the Mohr Coulomb method it takes into account the (σ_2) . The second is that the variables S and η are derivable through the Mohr Coulomb method using cohesion and internal angles of friction based on triaxial lab test data. Equations 31 and 32 are the equations for S and η .

$$S \text{ conversion} = C_o / \tan(\phi) \quad (31)$$

$$\eta \text{ conversion} = (4\tan^2(\phi)*(9-7\sin(\phi))) / (1 - \sin(\phi)) \quad (32)$$

One downside to the modified Lade method is that it is not truly accurate in the presence of any tensile stress component because it has no tension cutoff due to the cohesionless material component of the initial experiments done by Lade (1977).

3.2.4 Overall Comparisons

When calculating breakout thresholds, one should always use more than one method to compare results against any possible quality control data. This includes offset calipers or borehole imaging data, to confirm presence of real breakout in the wellbore at a known mud weight (Knöll, 2016). All methods have their pitfalls. Zhang et al. (2010) gives example of challenges of all three. He gives examples of assessments that demonstrate that the Mohr Coulomb criterion can underestimate rock strength leading to an overestimation of breakout thresholds. The modified Lade criterion can both under and overestimate rock strength, depending on your other variable estimations. The Mogi Coulomb has been found to be the most accurate in terms of rock strength estimation, however, given your area of study this may not always be the case if accurate major,

intermediate, and minor stresses cannot be determined accurately. This model uses all three to get a side by side comparison how the different methods compare to caliper and image log data.

CHAPTER IV: GEOMECHANICAL MODEL FEE BI #307

4.1 Study Area

My study area is in the west-central part of the Midland Basin (Bhatnagar et al., 2019; Verma and Scipione, 2020; Yandell et al., 2019), NW of the city of Midland as noted in Figure 11 below.

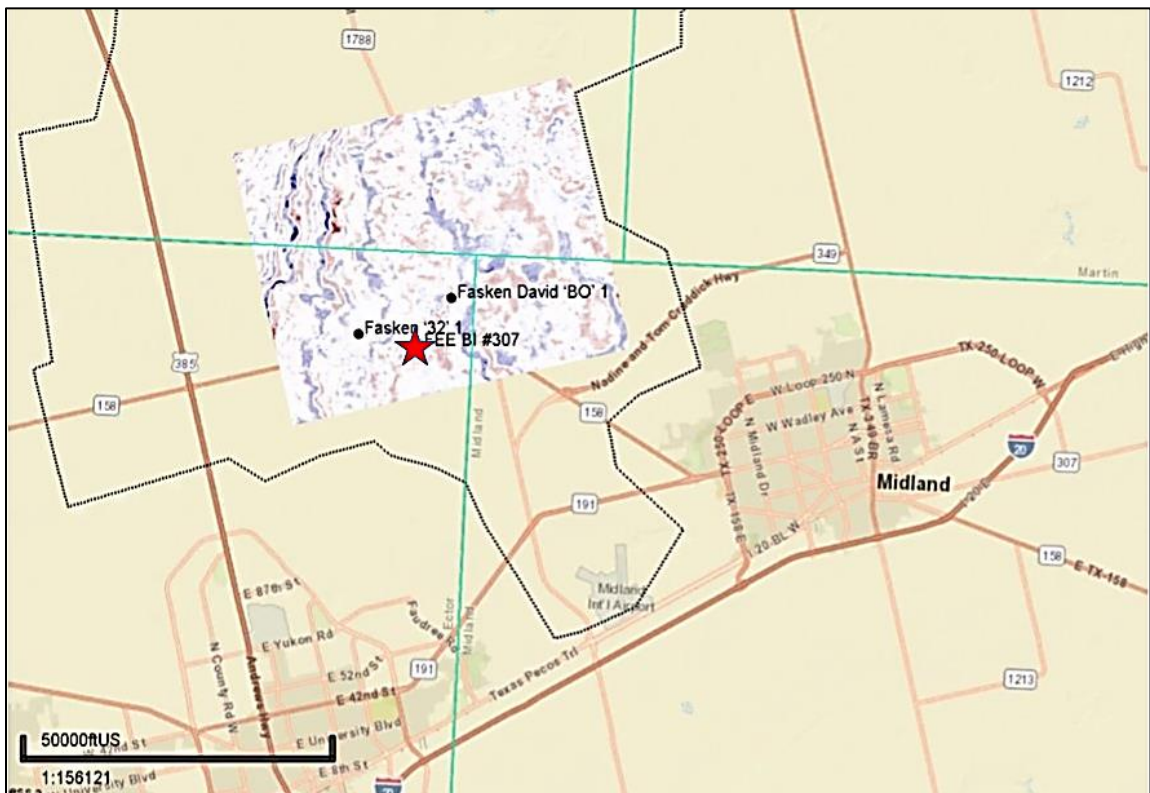


Figure 11: Map view of the study area in Fasken C Ranch. Red star indicated the Fee BI #307 well used in the model and the other two wells are offsets used to correlate tops.

The geologic section of the well logs used from the Fee BI #307 well were from mid Pennsylvanian to late Permian in age. From the Upper Spraberry formation down to the Strawn formation, with core points being collected in the Wolfcamp and Cline formations of strata. A heterogenous mix of sandstone, mudstones, siltstones, organic carbon rich shales, carbonaceous shales, and carbonates can be found in the section of well log studied. A geologic section of super sequence correlation can be observed below in Figure 12 for reference. Utilizing well logs, image logs, and core measurements of the well Fee BI #307, I attempted to build a 1D mechanical earth model and subsequent wellbore stability model using the calculated geomechanical data.

4.2 Well Overview

The Fee BI #307 well is located East of Gardendale Texas, South of US State Highway 158 (Figure 13). It is a vertical oil well spudded October 20th, 2011, in Permian Basin, Northwest of Midland Texas (Table 6).

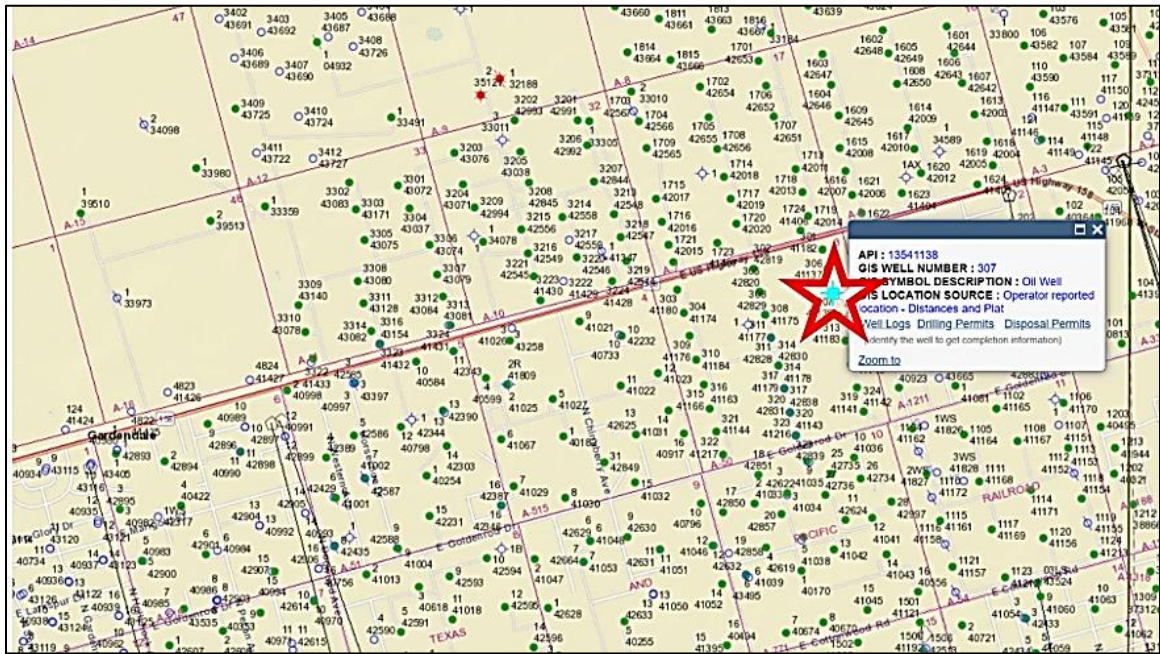


Figure 13: Image of the well location of Fee BI #307 well location from the Texas Railroad Commission (RRC, 2020).

Well Name	Fee BI #307
Depth	11,115 FT
API Serial Number	42-135-41138
Company	Fasken Oil and Ranch, LTD
Field	Spraberry Trend
County	Ector
State	Texas
Latitude	32.04612500°
Longitude	-102.31391670°

Table 6: Surface hole location and well information for Fee BI #307 well.

Two other wells were used to correlate formation tops Table 7 and Table 8 below describe their well information, general locations can be seen in Figure 11.

Well Name	Fasken '32' #1
Depth	13,600 FT
API Serial Number	42-135-34078
Company	Fasken Oil and Ranch, LTD
Field	Spraberry Trend
County	Ector
State	Texas
Latitude	32.05031950°
Longitude	-102.34485080°

Table 7: Surface hole location and well information for Fasken '32' #1 well.

Well Name	Fasken David 'BO' #1
Depth	11,530 FT
API Serial Number	42-135-33800
Company	Fasken Oil and Ranch, LTD
Field	Spraberry Trend
County	Ector
State	Texas
Latitude	32.06777100°
Longitude	-102.29809200°

Table 8: Surface hole location and well information for Fasken '32' #1 well.

4.2 Data Gathering

The accessible data sets from the Fee BI #307 well in the Permian Basin were quality control checked and the subsequent data sets were available and used to build the model.

Digital Data:

- Quad combo well logging data in .las format (LIDAR point cloud data)
- Caliper log data for offset Fee BM #1 SWD in .las format
- FMI log data printout for pilot hole in .pdf format (portable document format)
- Mud Log printout for pilot hole in .pdf format
- Survey Report in .csv format (comma-separated values file)

Core Data:

- Clay mineralogy report in .xls format (Microsoft Excel file format)
- Triaxial data test results in .xls format
- XRD (X-ray powder diffraction) test data in .xls format

- Core image printout in .pdf format
- Core image descriptions in .pdf format

4.2.1 Log Data

Table 9 below defines all the log curve data available for use in this model.

<u>Log curve name</u>	<u>Alias</u>	<u>Start depth (MD in ft)</u>
Gamma ray (API)	GR	201
Resistivity (ohm-m)	RESD	201
Compressional sonic travel time (μ sec/ft)	DTCO	6002
Shear sonic travel time (μ sec/ft)	DTS	6002
Bulk density (g/cm^3)	RHOB	6002

Table 9: Table describing the available log data, aliasing, and start depths of the digital log data for the Fee BI #307 well.

4.2.2 Core Data

Table 10 below defines all the core data points available for use in this model.

Measured Depth	Bulk Density	UCS	Compressional Transit Time	Shear Transit Time	Dynamic Moduli			Poisson's Ratio (ν)
					Shear modulus (G)	Young's modulus (E)	Bulk modulus (K)	
(ft)	(gm/cm ³)	(psi)	(μ s/ft)	(μ s/ft)	(psi)	(psi)	(psi)	
9,657.50	2.69	54150	50.48	96.36	3,904,675	10,236,742	9,019,072	0.311
9,740.00	2.646	102589	52.86	111.37	4,474,534	11,008,539	6,798,733	0.23
9,938.50	2.609	50133	60.38	106.32	3,111,324	7,852,772	5,498,359	0.262
9,995.50	2.589	30346	69.08	115.77	2,604,355	6,372,852	3,841,371	0.223
10,324.50	2.484	21675	83.81	138.89	1,735,934	4,213,636	2,452,508	0.214
10,374.00	2.729	38106	60.16	106.78	3,226,031	8,178,309	5,863,840	0.268

Table 10: Table describing the available core data points for the Fee BI #307 well.

Comparing the calculated geomechanical log data to core one can determine the validity of the calculated curves. Figure 14 below is an example of how they look in the model.

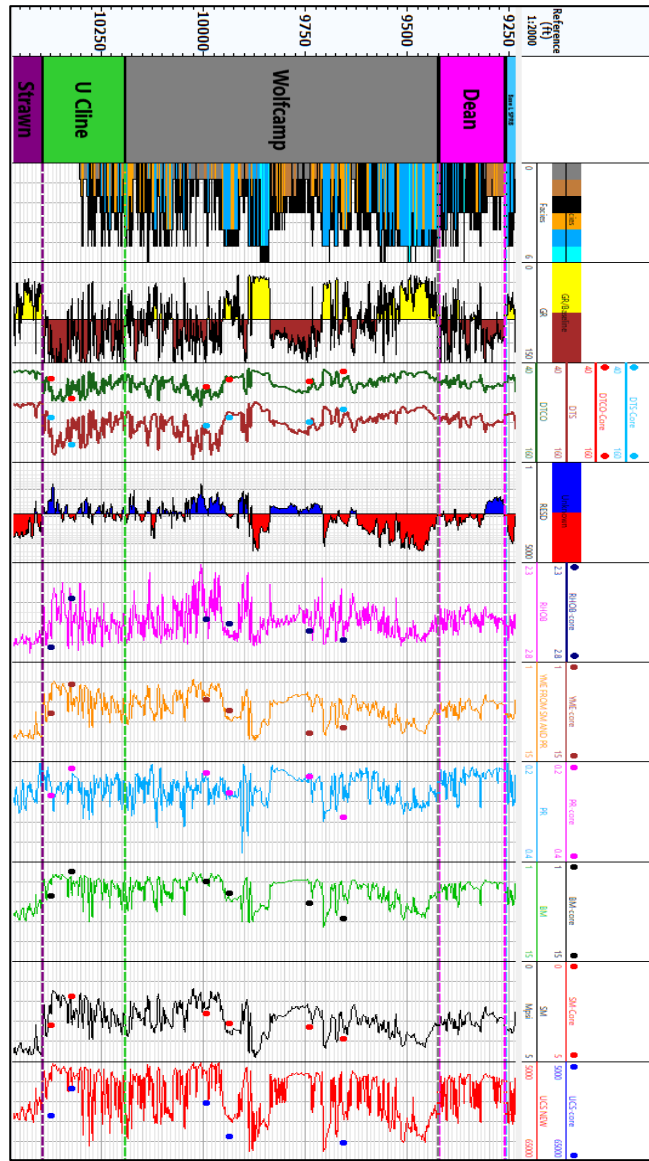


Figure 14: Different wireline logs along with computed well log curves, and machine learning facies of Fee BI #307 well. The computed well log curves include, Young’s modulus (*YME*), Poisson’s ratio (*PR*), bulk modulus (*BM*), shear modulus (*SM*), uniaxial compressive strength (*UCS*). The available core measured data points are posted on the corresponding well log curve track. Notice that the well log velocities, and density are approximately same as their core measured values.

4.2.3 Offset Data

One offset dataset was brought into this analysis and depth corrected to match tops from the Fee BM #1 SWD well to quality control breakout thresholds with a caliper log.

Table 11 below will portray the well information.

Well Name	Fee BM #1 SWD
Depth	14,200 FT
API Serial Number	42-003-42169
Company	Fasken Oil and Ranch, LTD
Field	Spraberry Trend
County	Andrews
State	Texas
Latitude	32.13607780°
Longitude	-102.26774520°

Table 11: Table describing the surface location and well data for the Fee BM #1 SWD well.

The following Figure 15 gives an example of the caliper curve and highlighted areas of borehole breakout used in the quality control process when viewing the breakout curve.

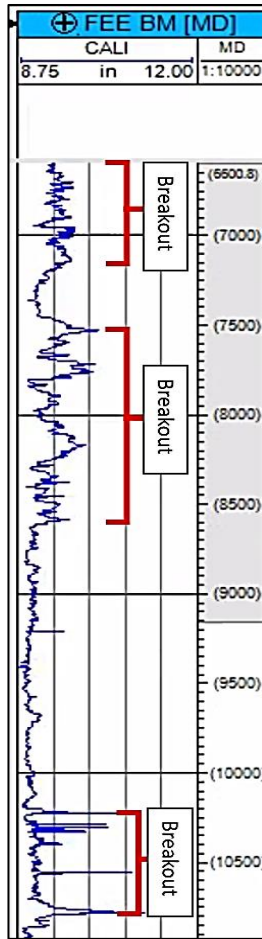


Figure 15: Log curve of caliper for the offset Fee BM #1 SWD well highlighting potential borehole breakout intervals of borehole enlargement.

4.2.4 Image Log

The image log for this well displays good examples of drilling induced fractures (Figure 16). It is clear by the 180° symmetry that these can be used to help determine minimum and maximum horizontal stress directions and are true drilling induced fractures (Tingay et al., 1998). The fractures in Figure 16 cut lithologies and are not bound by bedding, this proves them as drilling induced fractures and can be used to

determine present day minimum stress orientation. Forand et al. (2017) provides examples of bed bounded natural fracture systems on image logs.

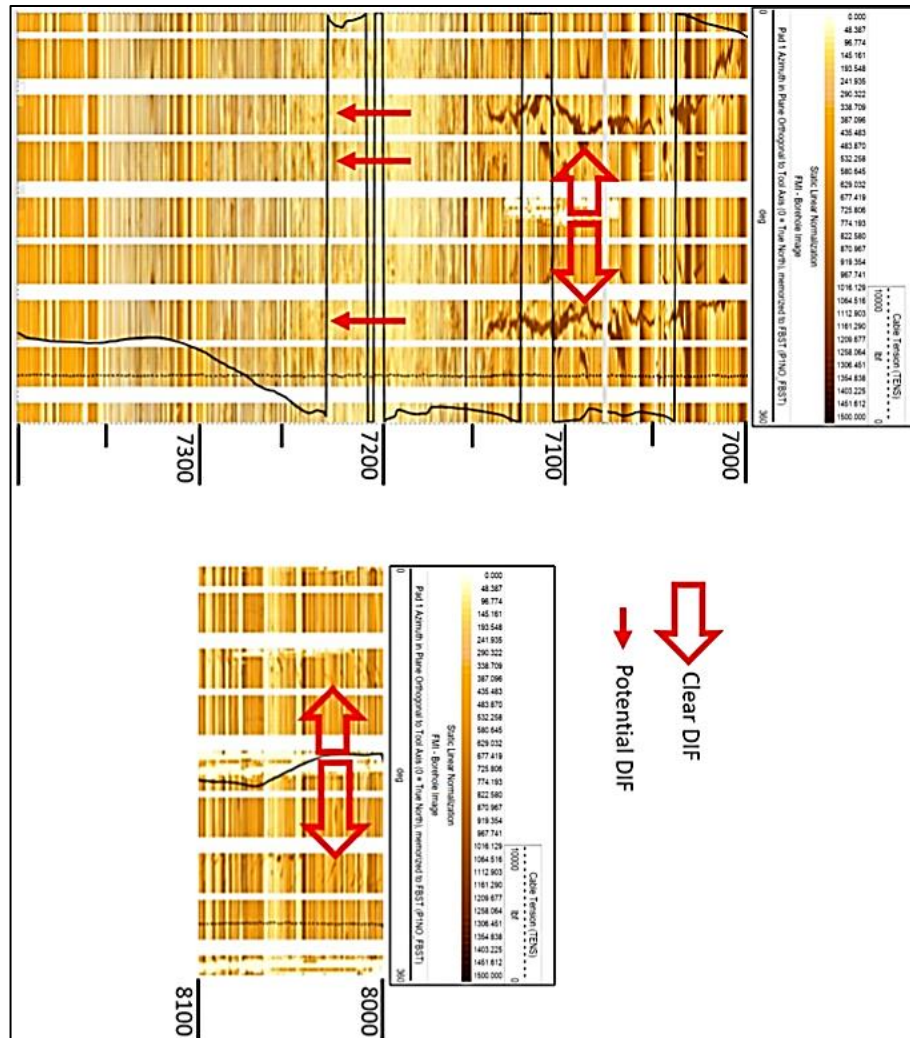


Figure 16: Sections of the image log taken for the Fee BI #307 well highlighting drilling induced fractures (DIF).

The image log from Figure 16 portrays the plane of minimum horizontal stress at $70^\circ - 110^\circ / 250^\circ - 280^\circ$. This plane is confirmed when observing the processed FMI rosette for this depth interval ranging from $80^\circ - 90^\circ / 260^\circ - 270^\circ$ as seen in Figure 17 below.

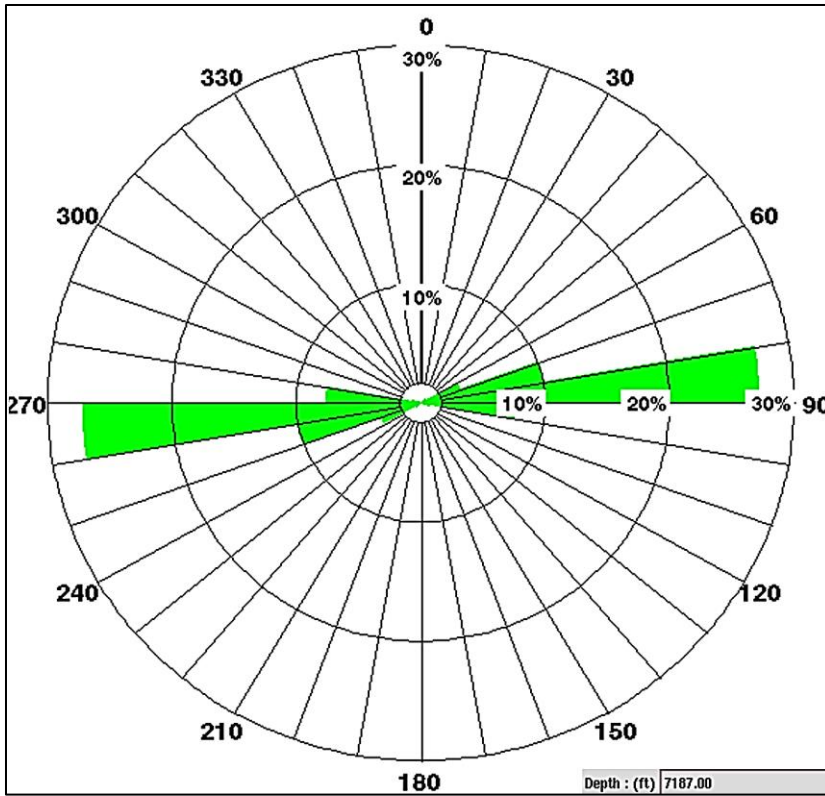


Figure 17: Processed FMI rosette provided by Fasken portraying the plane for minimum horizontal stress direction of 80° - 90° / 260°-270°.

4.2.5 Quality Control

All data files were quality controlled and any poor or null values were removed. Any significant log quality resolution data was removed from the triple combo data and exported in an ASCII file for use.

4.3 Mechanical Earth Model Workflow

Figure 18 below is a representation of the workflow used to build the wellbore stability model from the aforementioned data in sections 4.1 – 4.2.5.

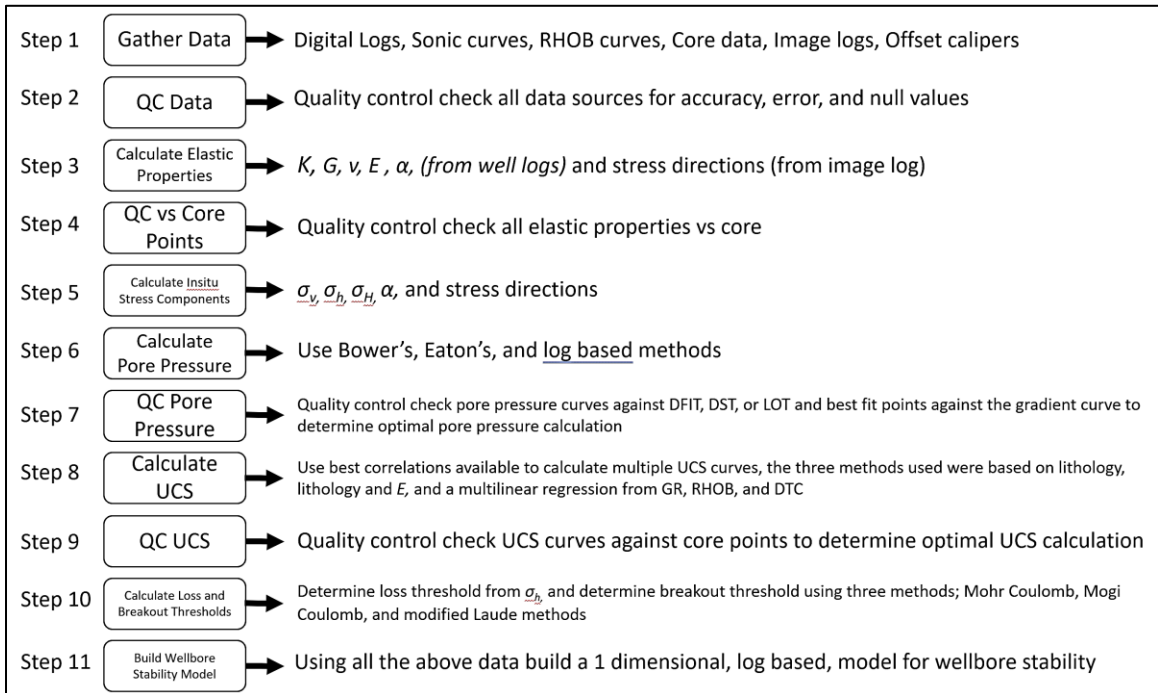


Figure 18: Example workflow used to build the wellbore stability model for the Fee BI #307 well.

4.4 Overburden

As previously discussed in section 2.2.1, overburden stress is mainly derived from the bulk density log using $\sigma_v = \sum_i \rho_i h_i g$ (11). In cases where a bulk density log is unavailable in shallower hole section, an acceptable method is to interpolate the overburden curve using the average slope intercept of your available overburden calculated from logs (Zhang, 2020). The following Figure 19 portrays a representation of overburden stress.

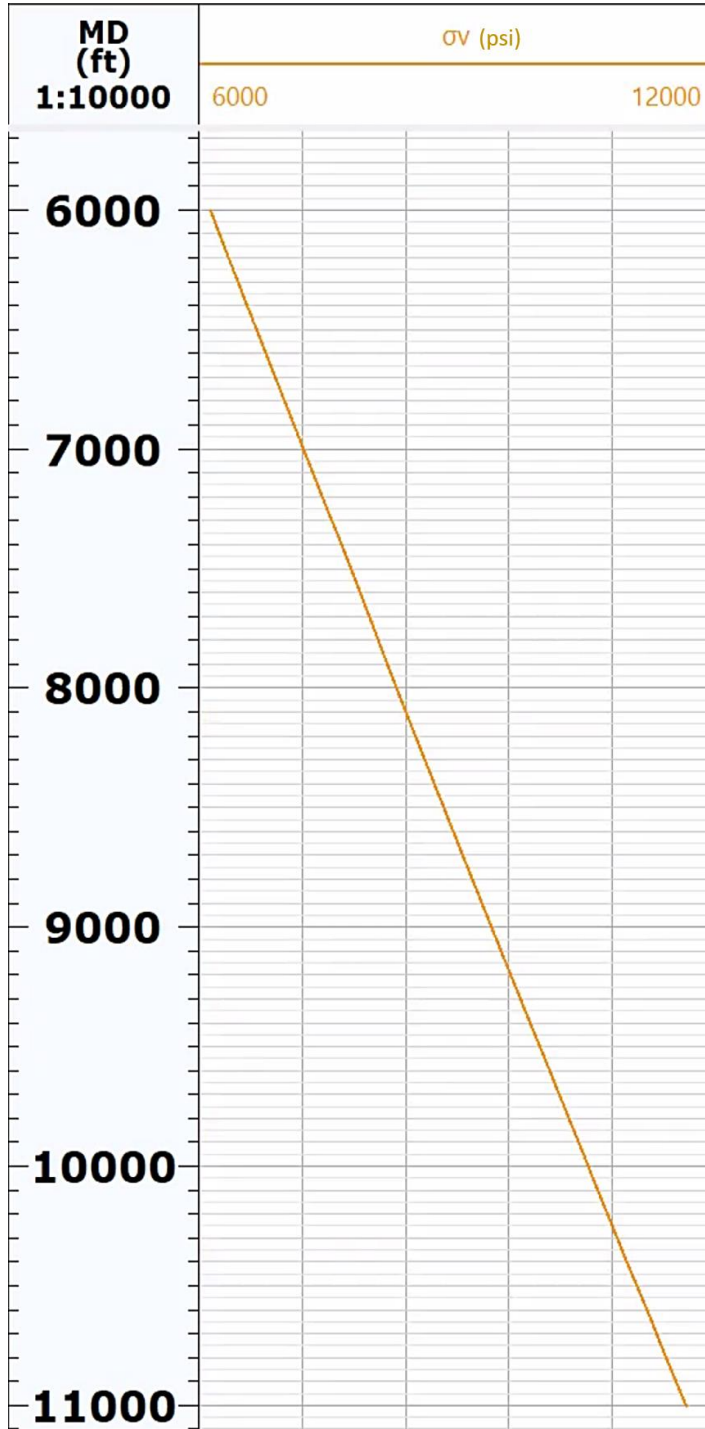


Figure 19: Example of calculated overburden curve.

Since there were no known over pressured intervals it was assumed that the slope of the overburden stress line was constant and hydrostatic.

4.5 Elastic Properties

In this section I calculate Young's modulus, Poisson's ratio, shear modulus, and bulk modulus as well as compared it to the core measurements.

4.5.1 Young's modulus (E)

Equation 2 and Equation

$E_{dyn} = 2 * G * (1 + \nu)$ (3 were used to calculate the dynamic Young's modulus from sonic data and density log curves and shear modulus and Poisson's ratio respectively. I chose to use the calculation from Equation

$E_{dyn} = 2 * G * (1 + \nu)$ (3 as it was a superior correlation with the quality control data points from core

Quality control data points were available throughout the Wolfcamp formation and the upper section of the Cline formation from 9657' MD – 10374' MD. The overall calculated Young's modulus curve looks strong compared to both the quality control points from core as well as the generated facies model as seen below in Figure 20.

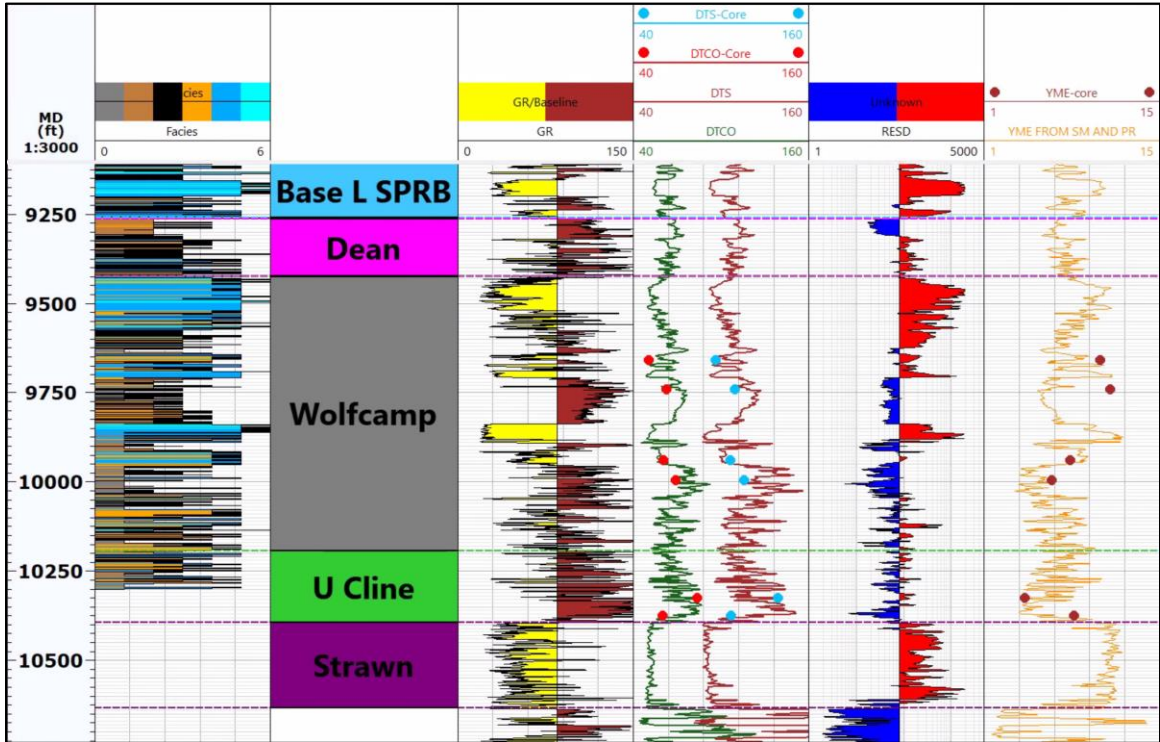


Figure 20: Different well log curves of Fee BI #307 well, between the depths of 9250 ft. (base of lower Spraberry) to 10150 ft. (Strawn formation). The last track of the well log display panel shows the computed Young’s modulus curve as along with core measured Young’s modulus data points.

4.5.2 Poisson’s Ratio (ν)

Equation 5 was used to calculate the dynamic Poisson’s ratio curve from sonic log data curves. Quality control data points were available throughout the Wolfcamp formation and the upper section of the Cline formation from 9657’ MD – 10374’ MD. The overall calculated Poisson’s ratio curve looks strong compared to both the quality control points from core as well as the generated facies model as seen below in Figure 21.

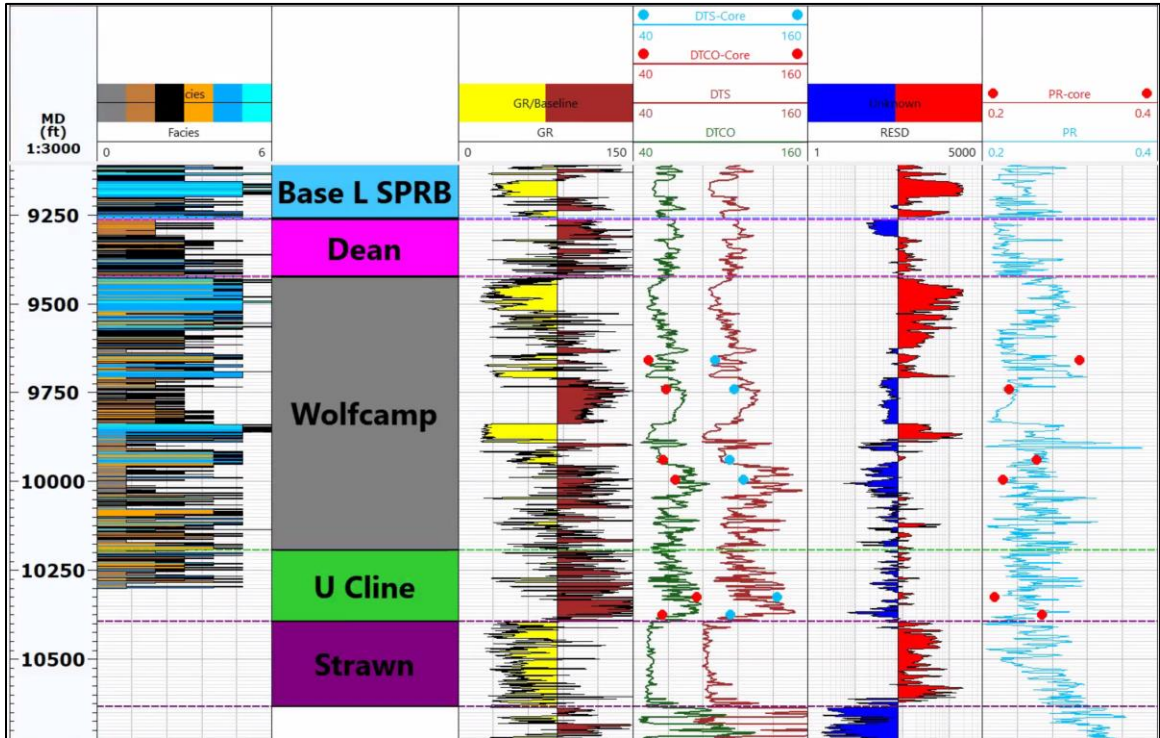


Figure 21: Different well log curves of Fee BI #307 well, between the depths of 9250 ft. (base of lower Spraberry) to 10150 ft. (Strawn formation). The last track of the well log display panel shows the computed Poisson’s ratio curve as along with core measured Poisson’s ratio data points in log view along with the facies model.

4.5.3 Bulk Modulus (K)

$$K = \rho (VP^2 - (4/3) VS^2) \quad (9 \text{ from section 2.1.4 was used to calculate a}$$

dynamic bulk modulus from density and sonic log data curves and is displayed in Kpsi.

Quality control data points were available throughout the Wolfcamp formation and the

upper section of the Cline formation from 9657’ MD – 10374’ MD. The overall

calculated bulk modulus curve looks strong compared to both the quality control points from core as well as the generated facies model as seen below in Figure 22.

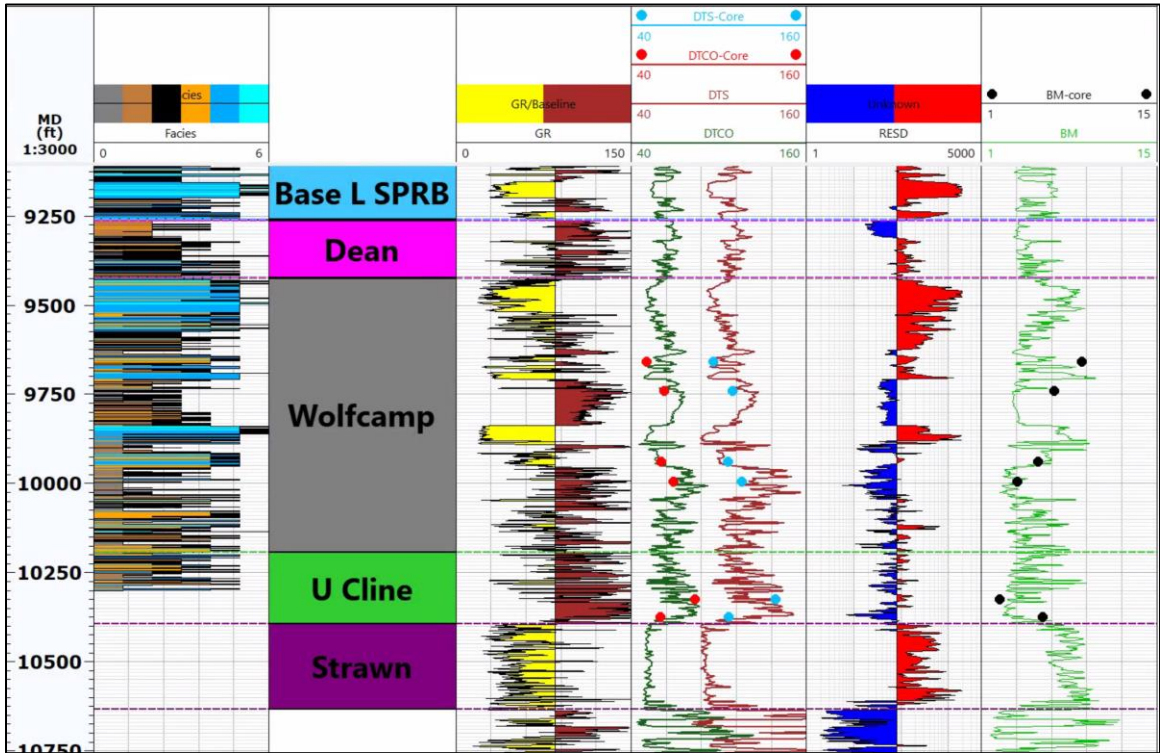


Figure 22: Different well log curves of Fee BI #307 well, between the depths of 9250 ft. (base of lower Spraberry) to 10150 ft. (Strawn formation). The last track of the well log display panel shows the computed bulk modulus curve as along with core measured bulk modulus data points in log view along with the facies model.

4.5.4 Shear Modulus (G)

$$G = \rho VS^2 \quad (\text{7 from section 2.1.3 was used to calculate the shear modulus}$$

curves from bulk density and shear sonic log data. Quality control data points were available throughout the Wolfcamp Formation and the upper section of the Cline formation from 9657' MD – 10374' MD. The overall calculated shear modulus curve

looks strong compared to both the quality control points from core as well as the generated facies model as seen below in Figure 23.

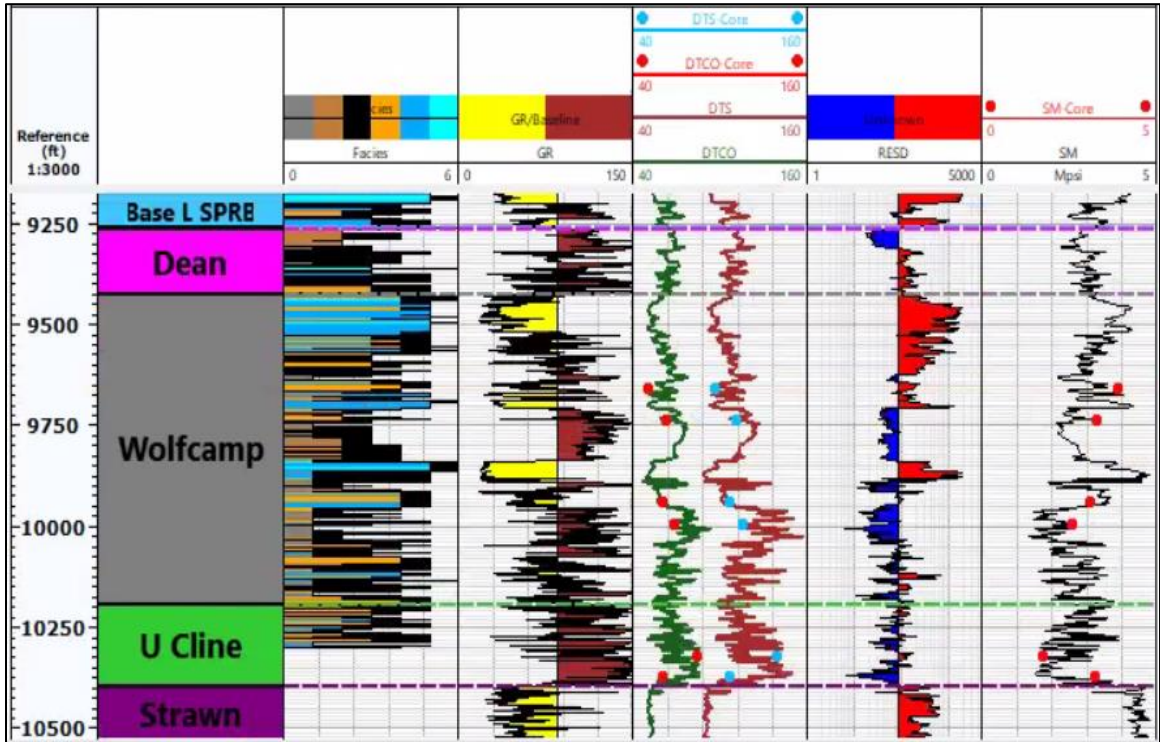


Figure 23: Different well log curves of Fee BI #307 well, between the depths of 9250 ft. (base of lower Spraberry) to 10150 ft. (Strawn formation). The last track of the well log display panel shows the computed shear modulus curve as along with core measured shear modulus data points in log view along with the facies model.

4.6 Rock Strength (UCS)

Calculating Rock strength can be one of the more challenging components of building a wellbore stability model as discussed in section 2.3. For this analysis, three different methods were utilized to generate three separate *UCS* curves and then compared to the *UCS* core data points. The first was based on a strict lithologic factor using the

facies model and then using the correlations from Table 2 from section 2.3.1. The second method was using the same lithologic factors and using both sonic and calculated Young's modulus curves, then using the correlations from Table 3 from section 2.3.1. The final method was through an attempted multi linear regression from gamma ray, bulk density, and compressional sonic data curves from the logs. The dataset I used for the linear regression was from 4 wells from the Suggs pad in the Permian Basin. These wells were obtained from the Hydraulic Fracture Test Site Collaboration ran by the Gas Technology Institute. The following Figure 23 gives a graphical representation of all three methods and demonstrates the second method using lithologic factors, sonic, and calculated Young's modulus curves as the best fit curve for *UCS* in the model given the offset quality control core data points. Note that the calculated *UCS* curves do slightly underpredict rock strength compared to core data points and can lead to slightly weaker rock strength than reality.

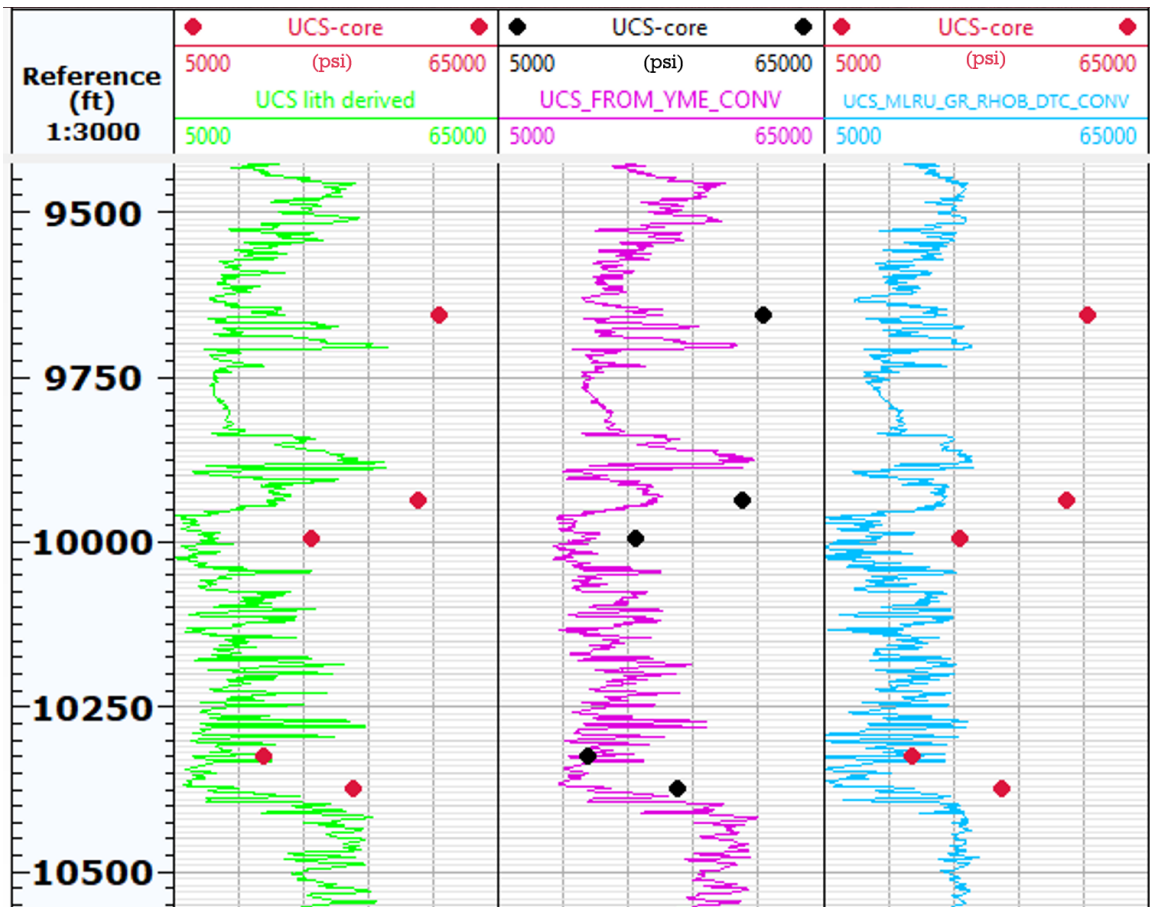


Figure 24: Three calculated *UCS* curves with quality control data points from core.

Upon review, I went through and took note that the first two core points were not correlating strongly. These points were around intervals of the machine learning facies of sandstone and carbonate intervals. Using equations from Table 4, I recalculated UCS for those facies making them stronger to better correlate to the first two core points. The result does correlate better, but is still not perfect. Given the calculated breakout thresholds, it is still within reason. Figure 25 gives a representation of the final UCS curve used in the model.

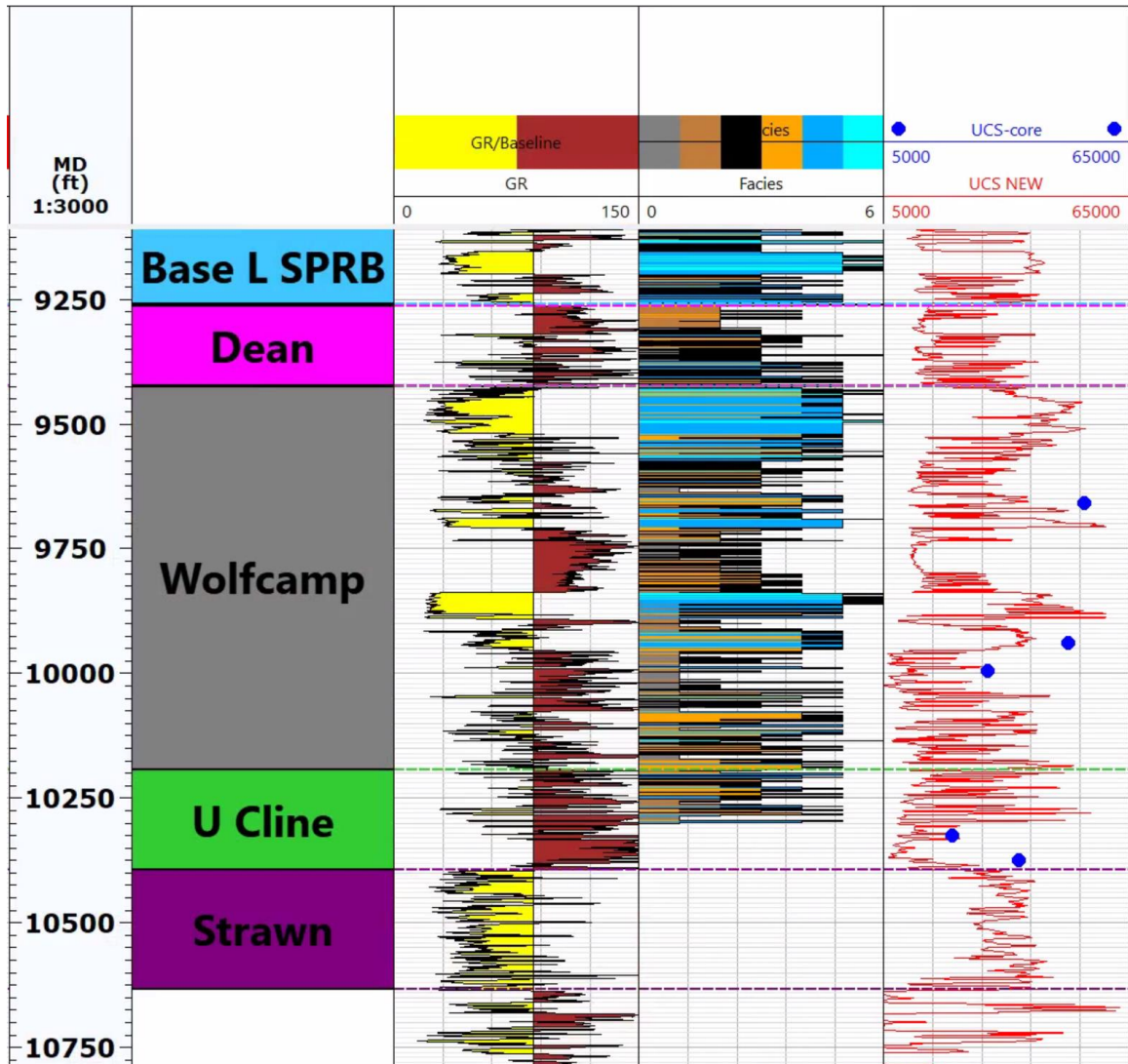


Figure 25: Gamma ray log curve of Fee BI #307 well, between the depths of 9250 ft. (base of lower Spraberry) to 10150 ft. (Strawn formation). The last track of the well log display panel shows the computed *UCS* curve as along with core measured *UCS* data points in log view along with the facies model.

4.7 Facies Breakdown

I used a machine learning techniques called support vector machine to classify facies. Support vector machines (SVMs) are a type of supervised learning model that can be trained on data to perform classification and regression tasks. For more information on the original workflow please look into Hall (2016) and Bohling and Dubois (2003). I trained my SVM on four different wells in Midland Basin (Hissong, 2020, Appendix D). Using this methodology, I was able to train a facies model to the Fee BI #307 well log with ~ 89% facies classification accuracy as seen in Figure 26 below. See Figure 12 from section 4.2.2 for a zoomed in image of the generated facies column against all calculated curves and core points.

```
print('Optimized facies classification accuracy = %.2f' % accuracy(cv_conf))  
  
Optimized facies classification accuracy = 0.89
```

Figure 26: Printed optimized facies classification accuracy percent for the Fee BI #307 facies SVM generation script.

The following Figures 27 - 29 give an overall example of facies to log comparisons used in this model as well as a zoomed in view to support the analysis and a facies classification key.

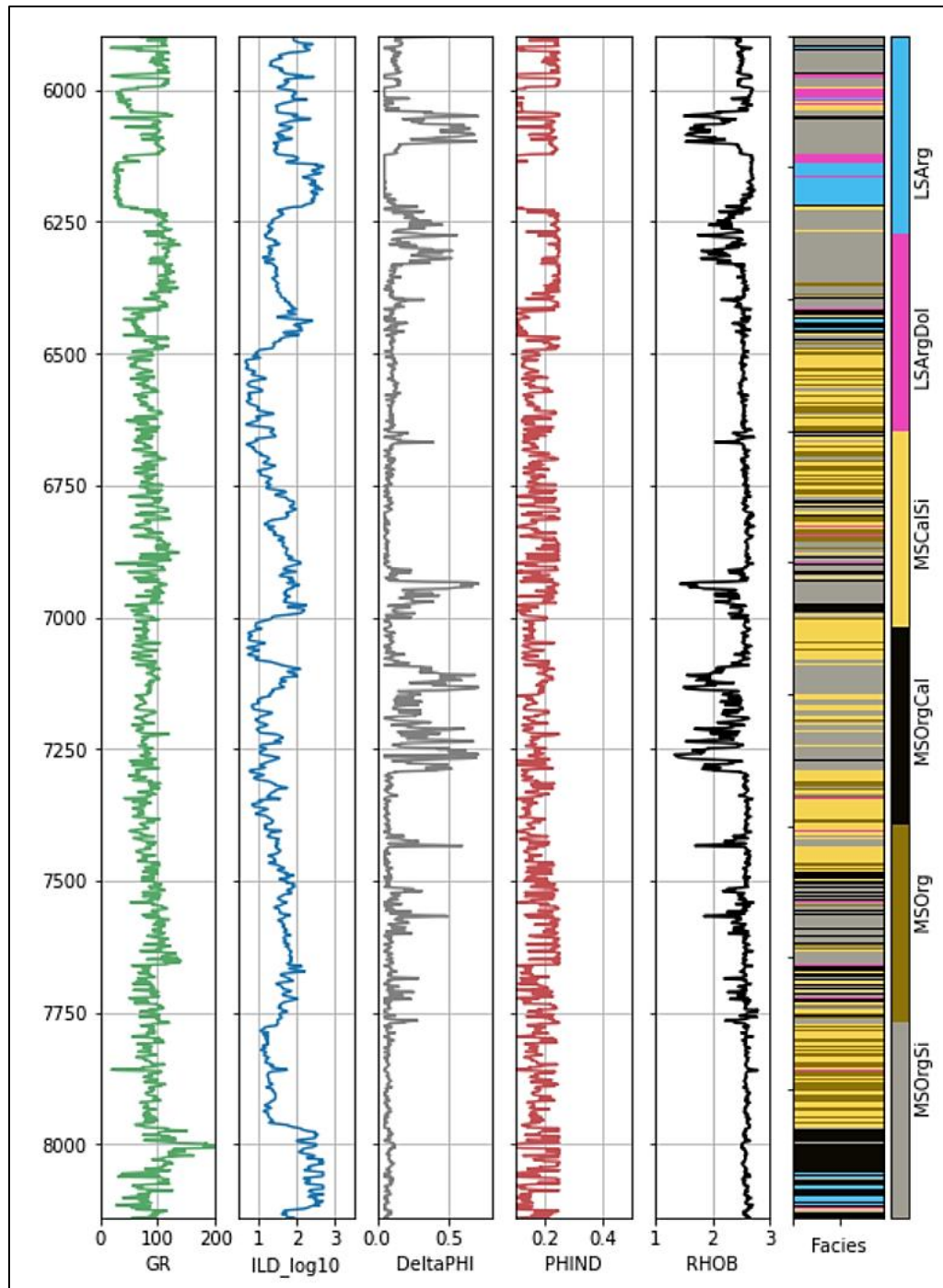


Figure 27: Printed log view with facies column using python for the Fee BI #307 well.

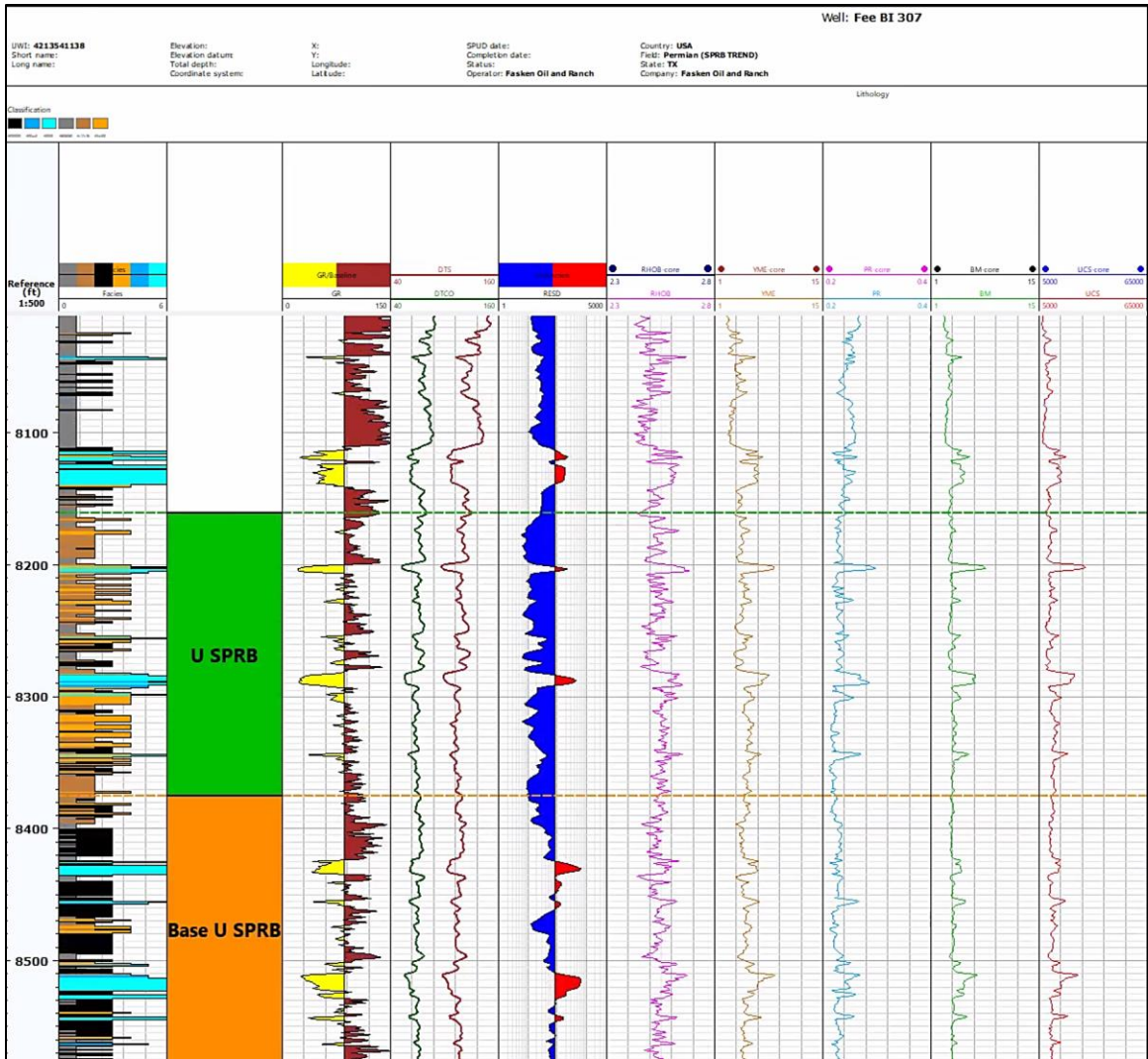


Figure 28: Zoomed in view of all geomechanical logs along with corresponding facies column.

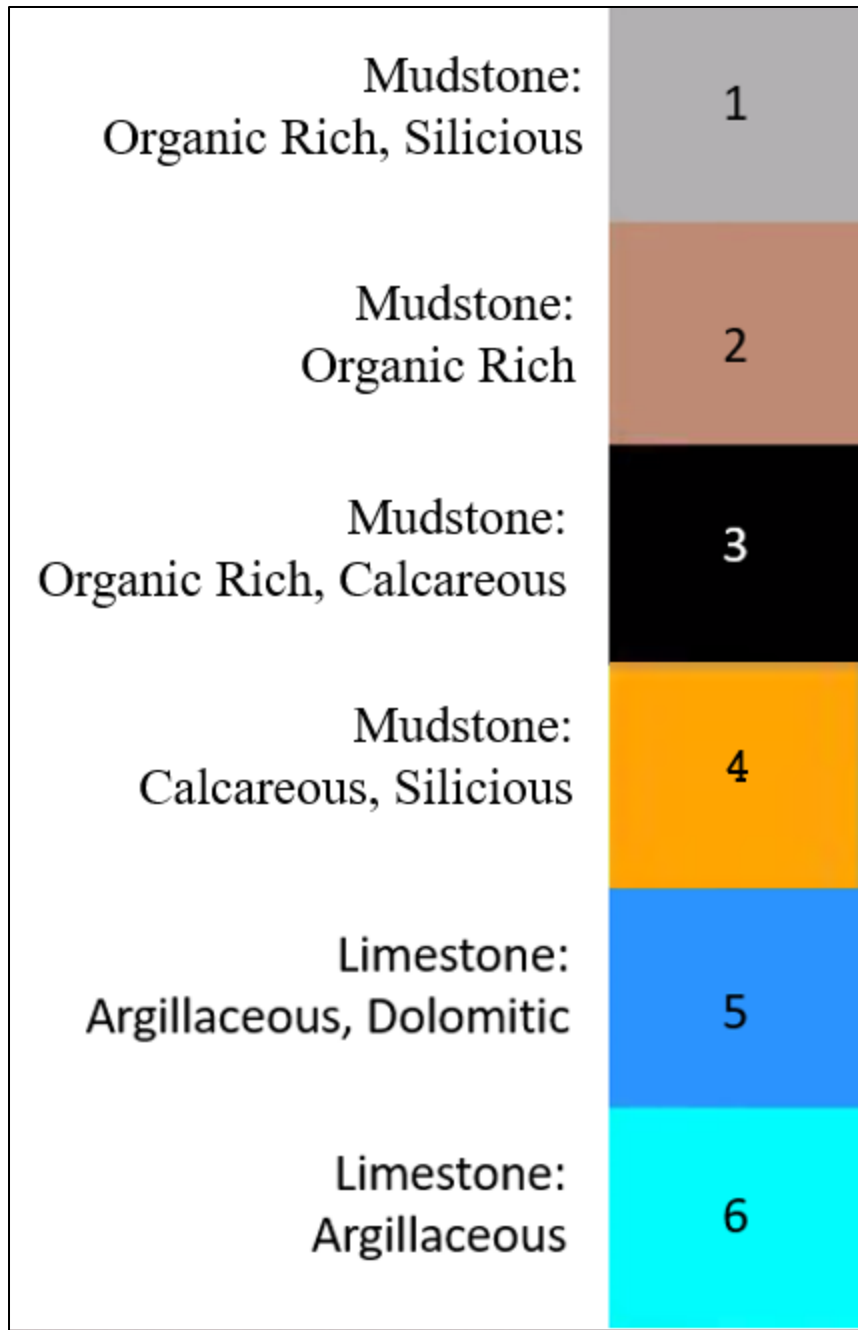


Figure 29: Facies classification key for calculated facies used on the Fee BI #307 well in this model.

4.8 Geologic Formation Tops

Geologic formation tops were correlated using three offset wells in the Fasken C Ranch dataset. Figures 30 - 32 below are the log view, map view, and actual depth values associated with the geologic tops used in this model and analysis.

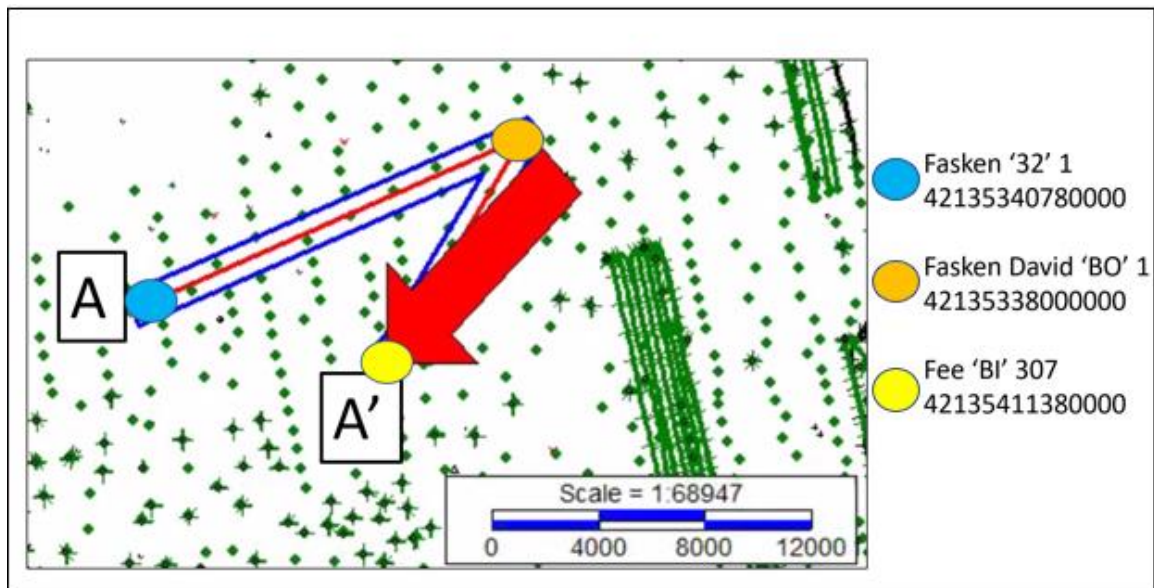


Figure 30: Map view, with scale, of the correlated geologic tops on the Fasken C Ranch dataset, including the Fee BI #307 well used in this model.

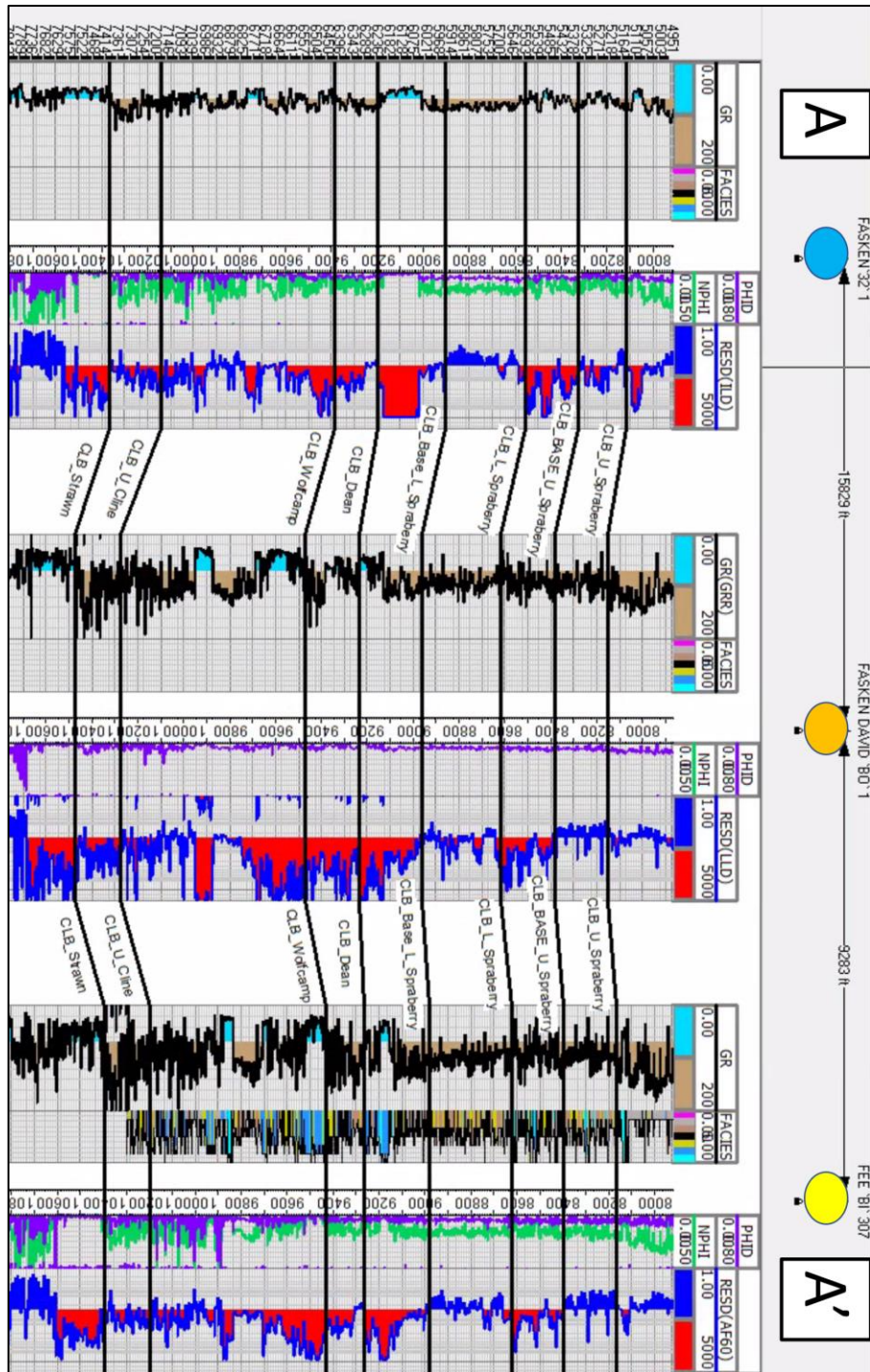


Figure 31: Cross section view of the geologic tops on the Fasken C Ranch dataset, including the Fee BI #307 well used in this model.

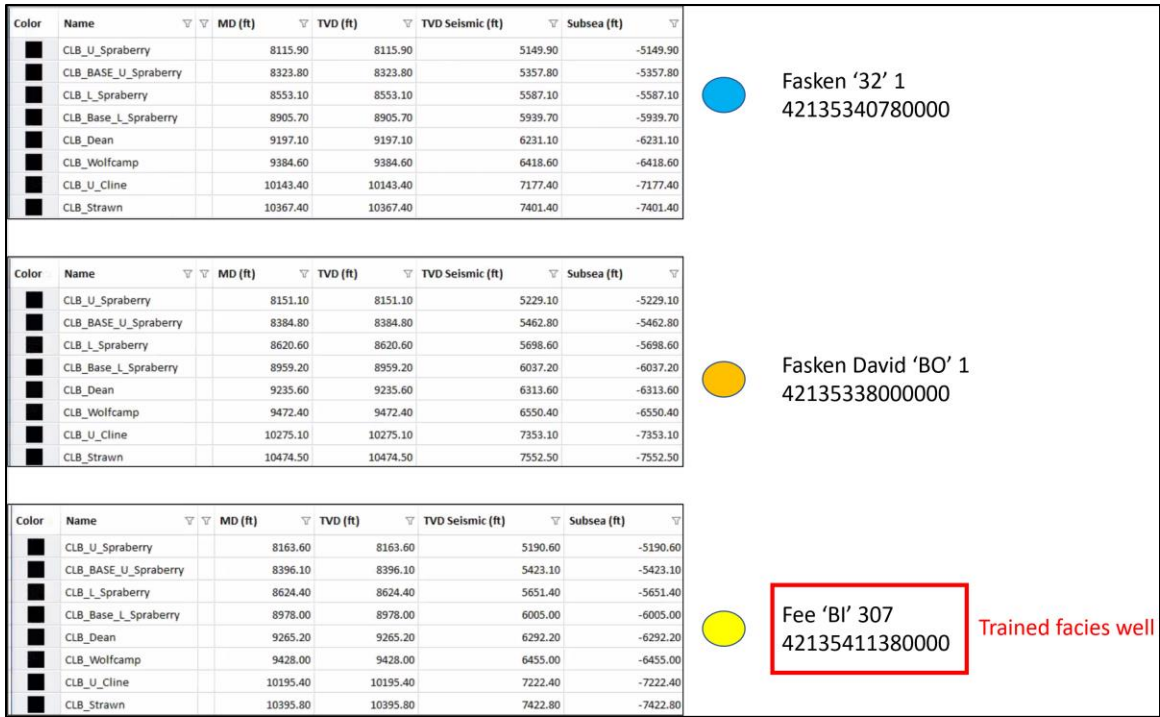


Figure 32: Associated depths of formation tops correlated on the Fasken C Ranch dataset, including the Fee BI #307 well used in this model.

4.9 Pore Pressure (P_p)

To achieve an accurate pore pressure, usually one would use data sources from the drilling program to calibrate a log-based pore pressure curve. While I did use Eaton's method seen in $P_p = \sigma_v - (\sigma_v - P_{png}) * (\Delta t_n / \Delta t)^n$ (21 in section 3.1, I did not have access to any FIT data points, or LOT data points to obtain a baseline for the pore pressure trend line. The n value was assumed to be one as I did not have any quality control data to calibrate the pore pressure curve to and no areas of overpressure or gradient changes could be calculated or calibrated as they were unknowns.

Figure 33 below is the calculated graphical representation of the estimation of the pore pressure and calculated overburden curve used to define pore pressure for this model.

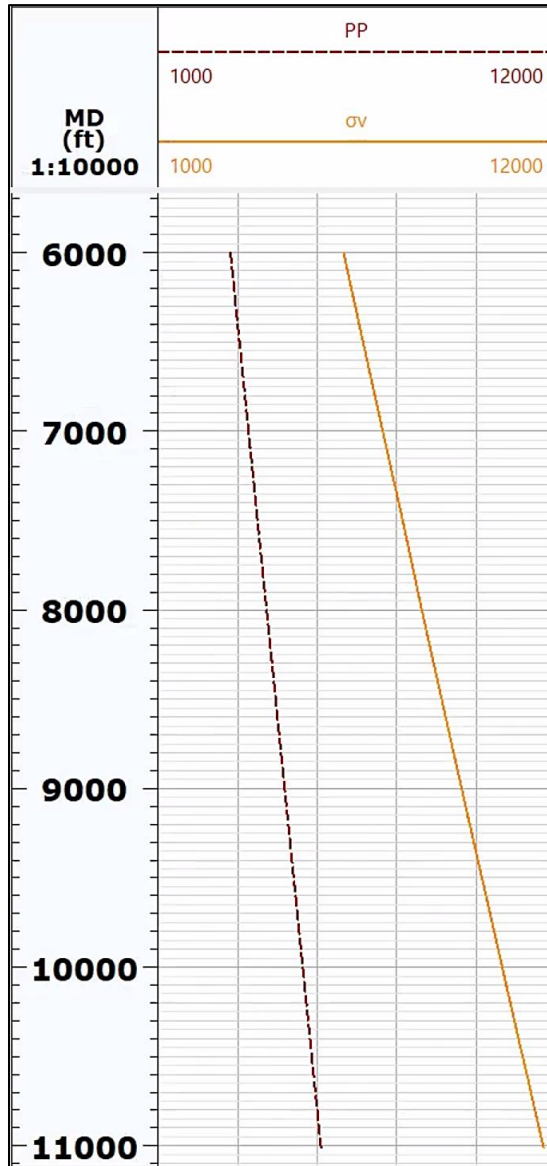


Figure 33: Visualization of pore pressure and overburden calculated curves used in this model. Units are in psi.

4.10 Minimum Horizontal Stress (σ_h)

As discussed in section 2.2.2 the minimum horizontal stress curve is imperative because it is the main component of the loss threshold that will be described in section 4.11. Assuming an isotropic system, I used Equation 13 from section 2.2.2, using calculated curves for Poisson's ratio, overburden, and Biot's constant, the estimated pore pressure discussed in section 4.8, as well as estimated tectonic stress from Lund Snee and Zoback (2016). Figure 34 is an example of the minimum horizontal stress curve. However, without DFIT data points, or LOT data points to quality control check pore pressure to, it is only an estimation.

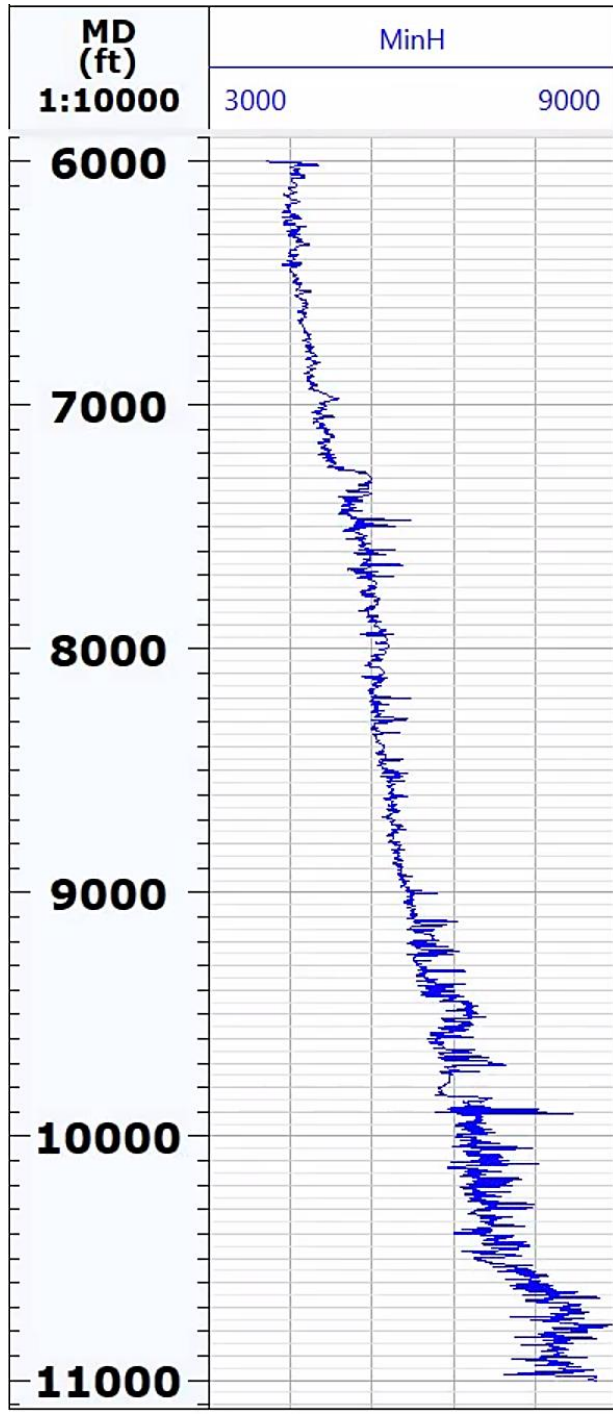


Figure 34: Visualization of minimum horizontal stress calculated curve. Units are in psi.

4.11 Loss and Breakout Thresholds

While calculating all the geomechanical rock properties is helpful to the drilling process, the true benefit is to the well planning process and potential cost savings comes from defining accurate breakout and loss threshold curves along with a safe mud weight windows (Singh et al., 2019). By analyzing zones that could potentially lead to serious loss/flow hole conditions, or defining intervals of potential wellbore breakout, one can be proactive in the drilling program. This leads to having an easier time testing new zones of interest, having less problems running casing, as well as less problems drilling the curve and lateral sections of the wellbore (Haidary et al., 2015). To understand the next calculated log images, one must understand the concepts behind calculating loss and breakout threshold. The loss threshold is calculated using Equation 33.

$$\text{Loss Threshold} = (\sigma_h / MD) / 0.052 \quad (33)$$

where,

MD = measured depth (ft)

It represents the mud weight, that if the pressure of the fluid in the hole reaches, will overcome the surrounding lithology's pore space. It leads to fluid being pushed out into the surrounding formation and mud losses occurring in the hole. In a vertical sense, it is a good indication of potential mud loss or fluid flow zones. This leads to better planning. and potential cost savings. One can budget extra mud on location or predict zones to use lost circulation material or an LCM program to minimize mud losses or fluid

flows if they are unavoidable. The calculated loss threshold curves are represented by a light blue shaded line in the model as seen in Figure 35.

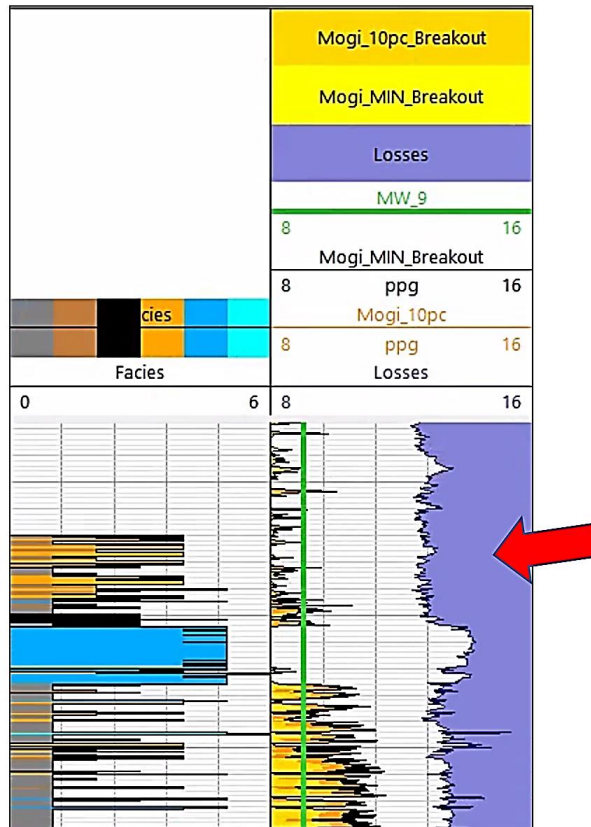


Figure 35: Visualization of calculated loss threshold curve. Threshold units are in ppg.

The breakout threshold is more complicated to calculate due to the uncertainty in rock strength. There are multiple methods as discussed in section 4.5. The breakout threshold is the point at which your fluid column is too weak to support the surrounding lithology and rock starts to fall into the current borehole, leading to cavings, and borehole collapse (Zhang, 2020). The following Figure 36 is the visual representation of the breakout threshold as a yellow shaded curve and an orange shaded curve. The yellow

curve represents when the first grain of lithologic sediment falls into the borehole, while the orange shaded section represents the threshold for 10% of the surrounding sediment breaking apart and falling into the borehole leading to hole instability and collapse.

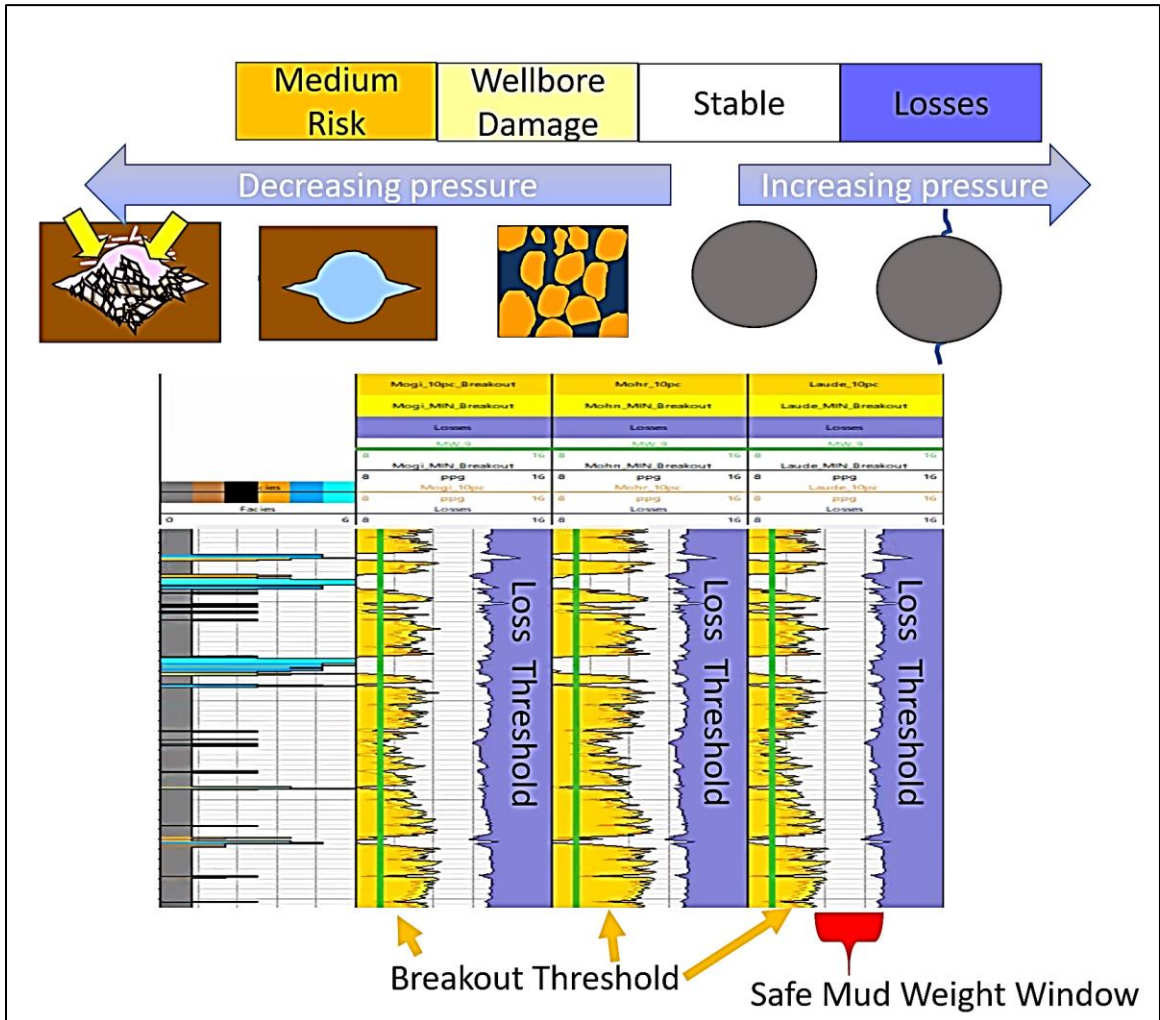


Figure 36: Visualization of calculated breakout threshold curve, safe mud weight window, and accompanying examples of wellbore complication risks.

Figure 36 also gives an example of the safe mud weight window represented as the white area. This is an ideal mud weight used to drill this section that is modeled to encounter no wellbore breakout or fluid losses at a given mud weight.

Three separate breakout threshold calculations were used that were also discussed in sections 3.2.1 – 3.2.3 in the literature review. They were generated using Tech Log 2019 wellbore stability modeling module using the variables in Figure 37 below.

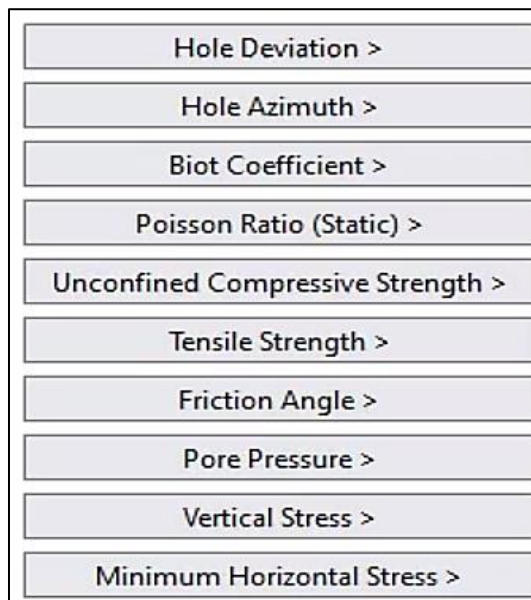


Figure 37: Example of necessary curves to run a Mohr Coulomb, Mogi Coulomb, and modified Lade breakout curve using the wellbore stability modeling module used in this model.

The three separate log tracks below in Figure 38 gives an example of the full wellbore of the Fee Bi #307 well and the calculated breakout threshold, loss threshold, and safe mud weight windows along with offset caliper data to help quality control the

calculated breakout thresholds. The green line represents a mud weight of 9.0 ppg as a reference point.

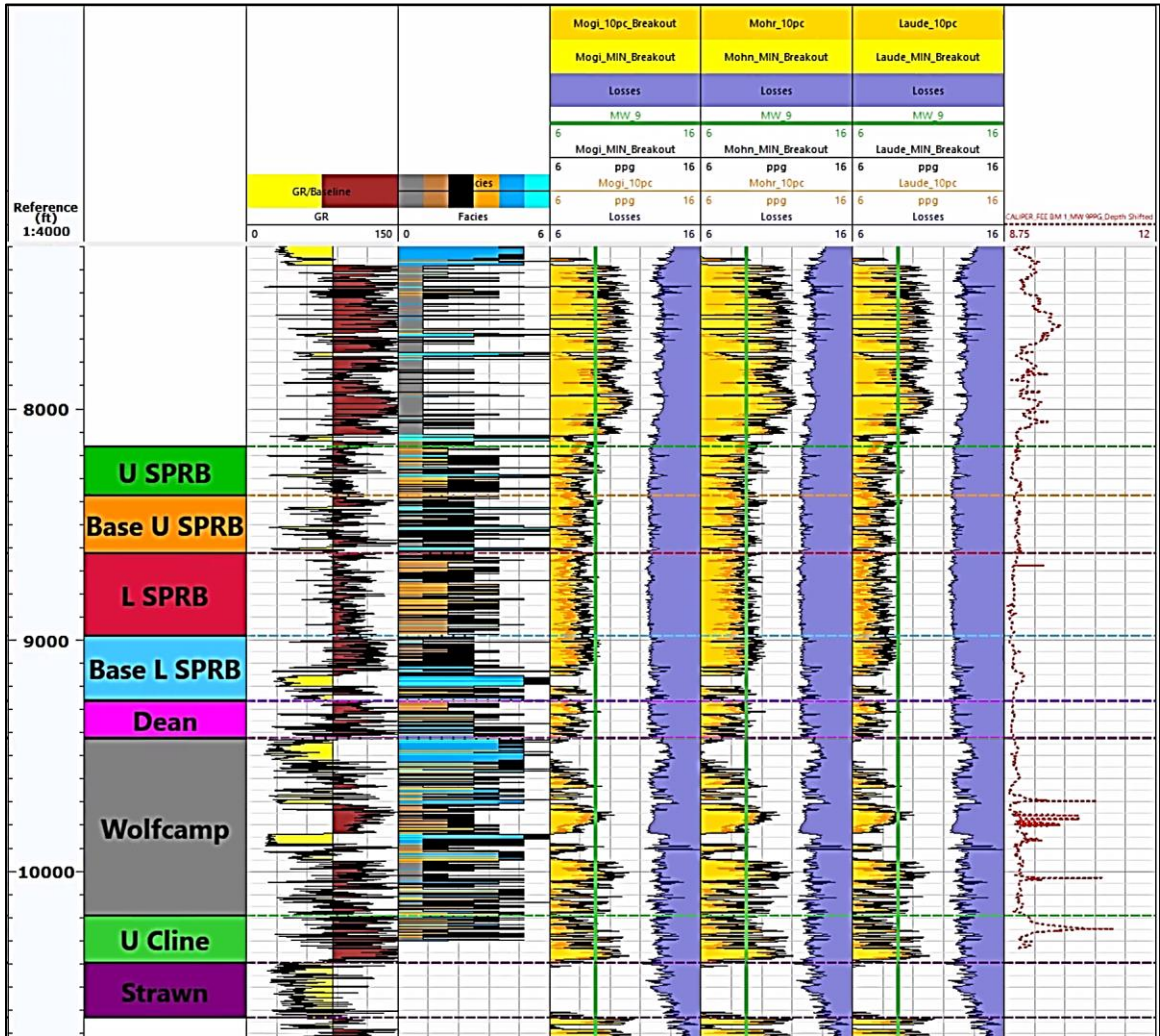


Figure 38: Example of calculated breakout threshold, loss threshold, and safe mud weight windows; Along with offset caliper data, and facies logs, to help quality control the calculated breakout and loss thresholds.

An image log and offset caliper log were also used to quality control the breakout thresholds for this model. Figure 15 is the offset caliper showing breakout at ~ 7500' MD

– 8500’ MD and in Figure 15 the red caliper log shows breakout from ~ 7000-8000’ MD leading credence to our calculated breakout thresholds in the same figure. The image log from Figure 16 also shows drilling induced fractures through some of the intervals the breakout threshold predicts breakout which is promising.

4.12 Cross Plots

Figures 39 – 42 are cross plots from the calculated geomechanical properties from the model colored by the generated facies. The r^2 values and lithologic groupings are strong which builds confidence in the facies model and the *UCS* curve in terms of lithology. The groupings observed lead credence to the facies model as well, visualizing clear clusters of limestone, siliciclastic mudstone, and organic rich mudstones in regards to their geomechanical parameters. Weaker shales are clearly distinguishable from stronger sands and limestone.

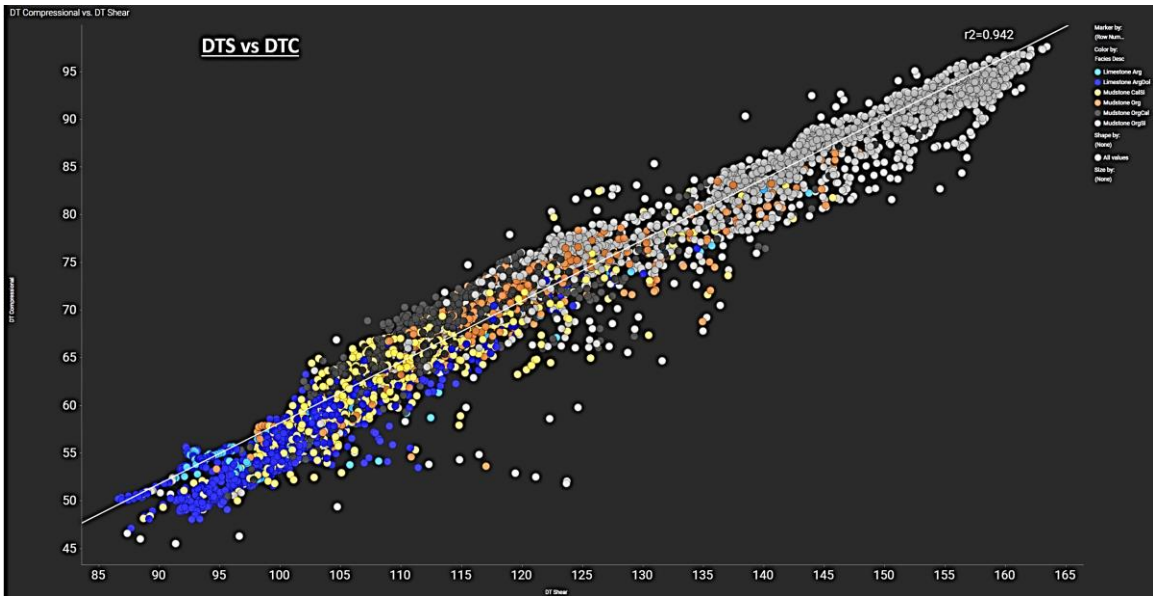


Figure 39: Cross plot of compressional and shear sonic log data colored by facies with an r^2 value of 0.94.

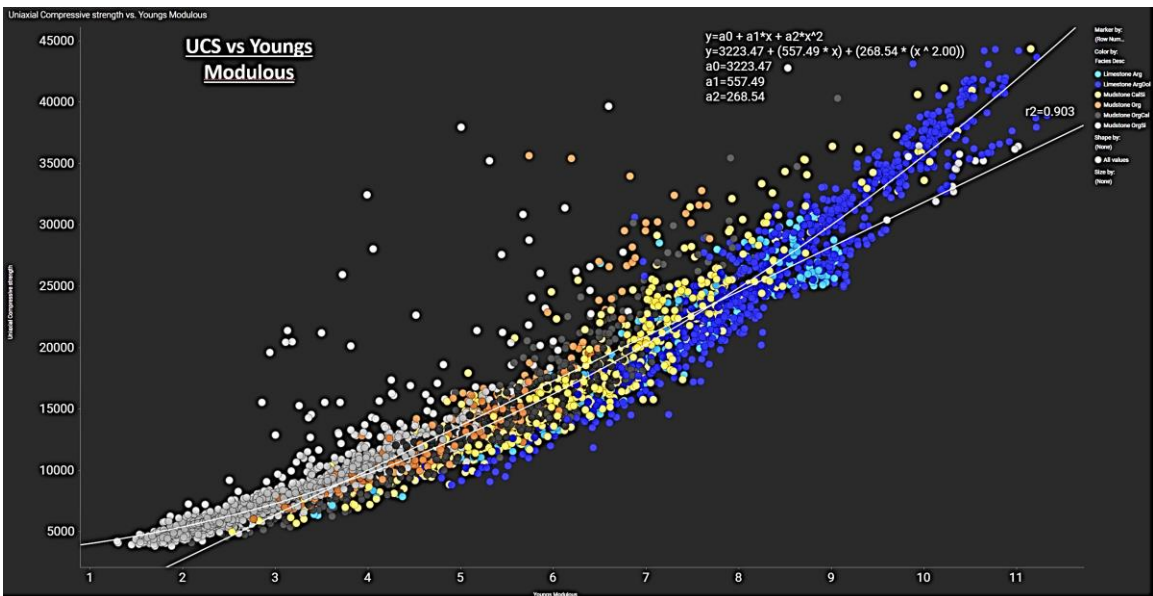


Figure 40: Cross plot of UCS and Young's modulus colored by facies with an r^2 value of 0.90 and attributed best fit curve values.

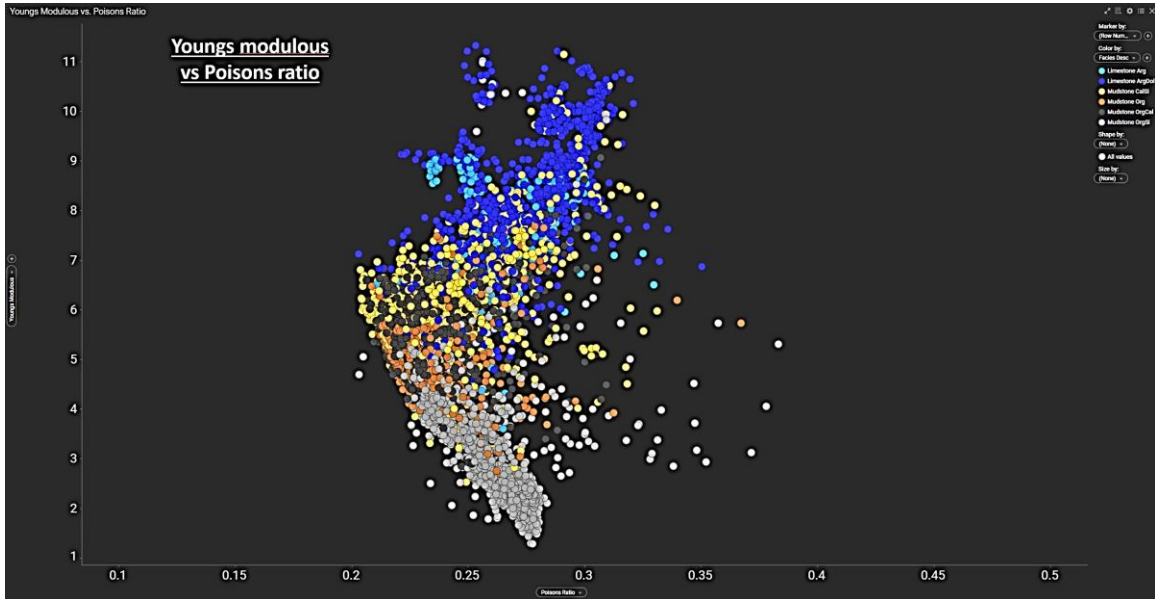


Figure 41: Cross plot of Young's modulus and Poisson's ratio colored by facies.

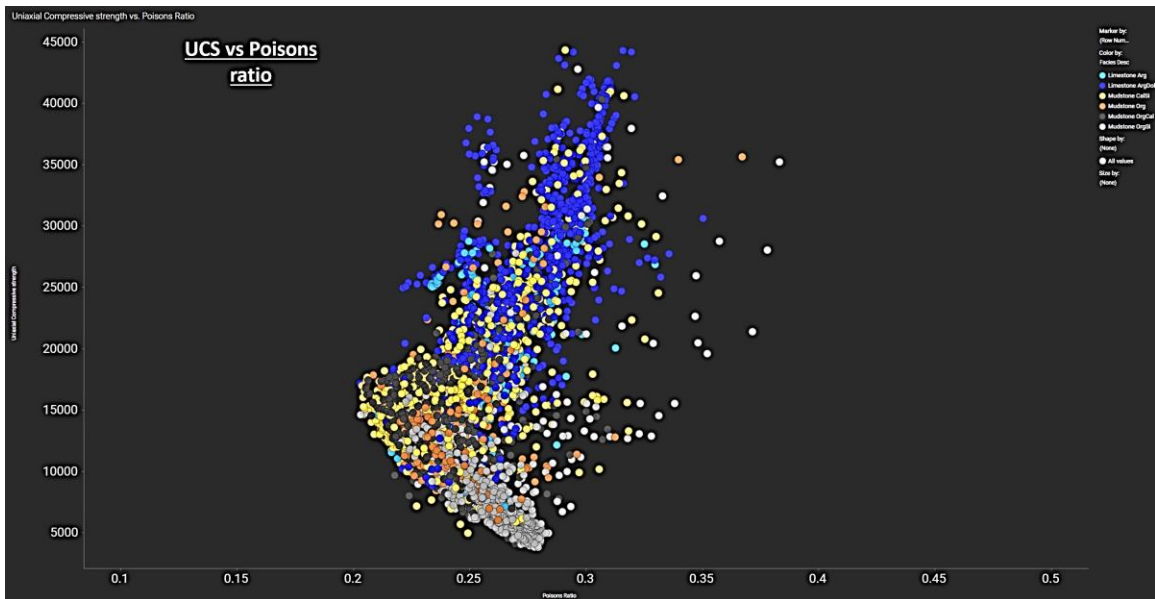


Figure 42: Cross plot of UCS and Poisson's ratio colored by facies.

CHAPTER V

5.0 DISCUSSION AND CONCLUSIONS

Building the mechanical earth model for Fee BI #307 well was a rewarding and challenging undertaking. The final model generated, while not perfect, does a fantastic job predicting known breakouts in the area and is realistic when put up against the generated facies model. Figure 43 below gives a representation of potential areas of concern for breakout. While there are weaknesses to the model that will be discussed below, the generated wellbore stability model is a strong tool that can help make good decisions in the drilling process and is a useful baseline for future geomechanical study in the area.

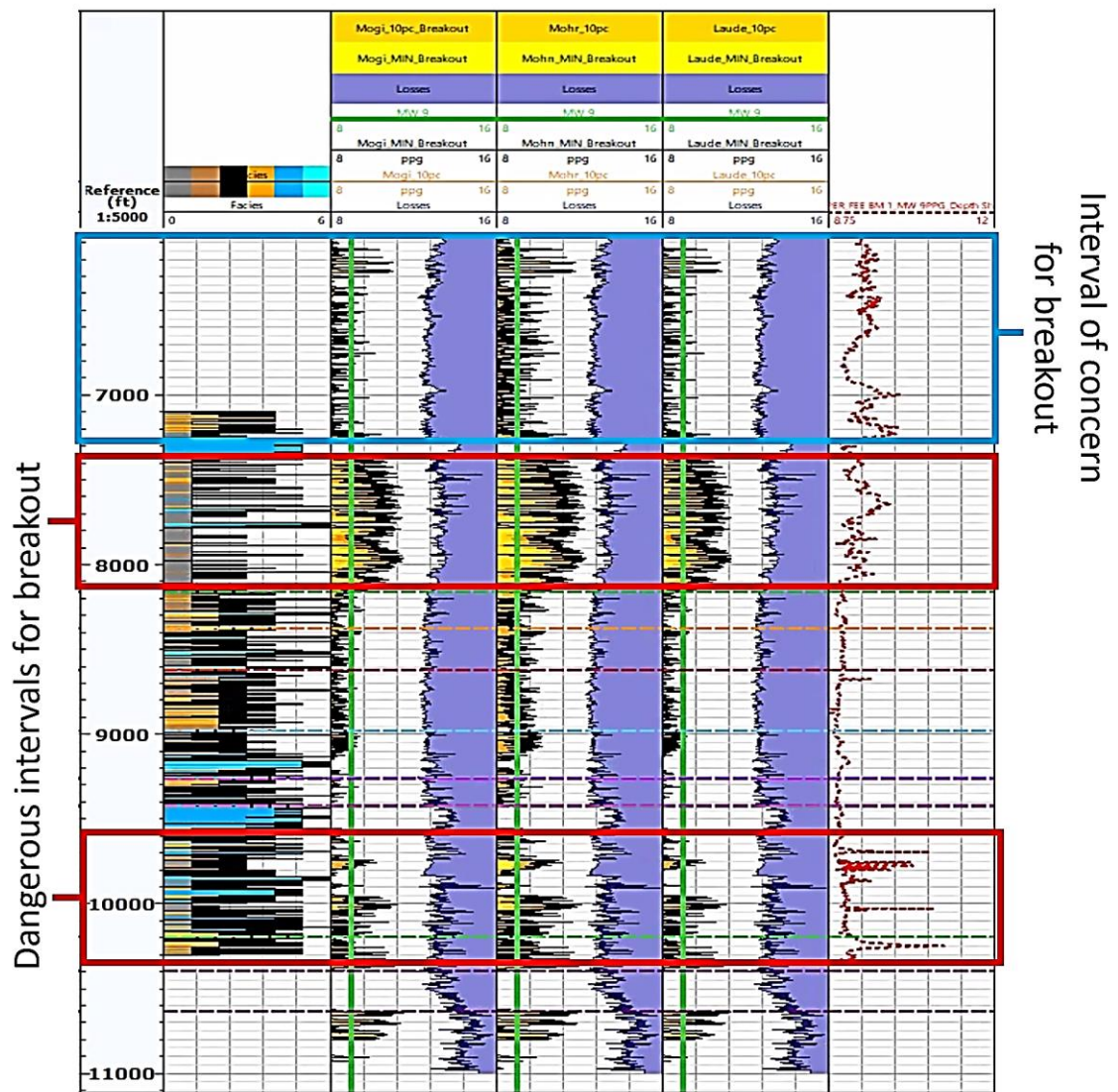


Figure 43: Example of calculated breakout threshold, loss threshold, and safe mud weight windows; Along with offset caliper data, and facies log, visualizing the potential problematic intervals while drilling. Thresholds units are in ppg.

Potential areas of concerns for breakout are from 7380' MD – 8105' MD with a safe mud weight of ~11.3ppg and 9630' MD – 10269' MD with a safe mud weight of ~11.7ppg.

The facies model appears very accurate when viewed with all the log curves and calculated curves along with the trend of the breakout threshold where our mudstones are appearing weaker and more prone to breakout and limestones are appearing stronger and more resilient. Figure 44 below is a zoomed in view of an example of just how well the breakout threshold are correlating to the lithologic and log-based character of the curves and generated facies. It is clear the model is doing a superb job at capturing trends in rock strength and weakness, especially in the smaller sand and limestone stringers.

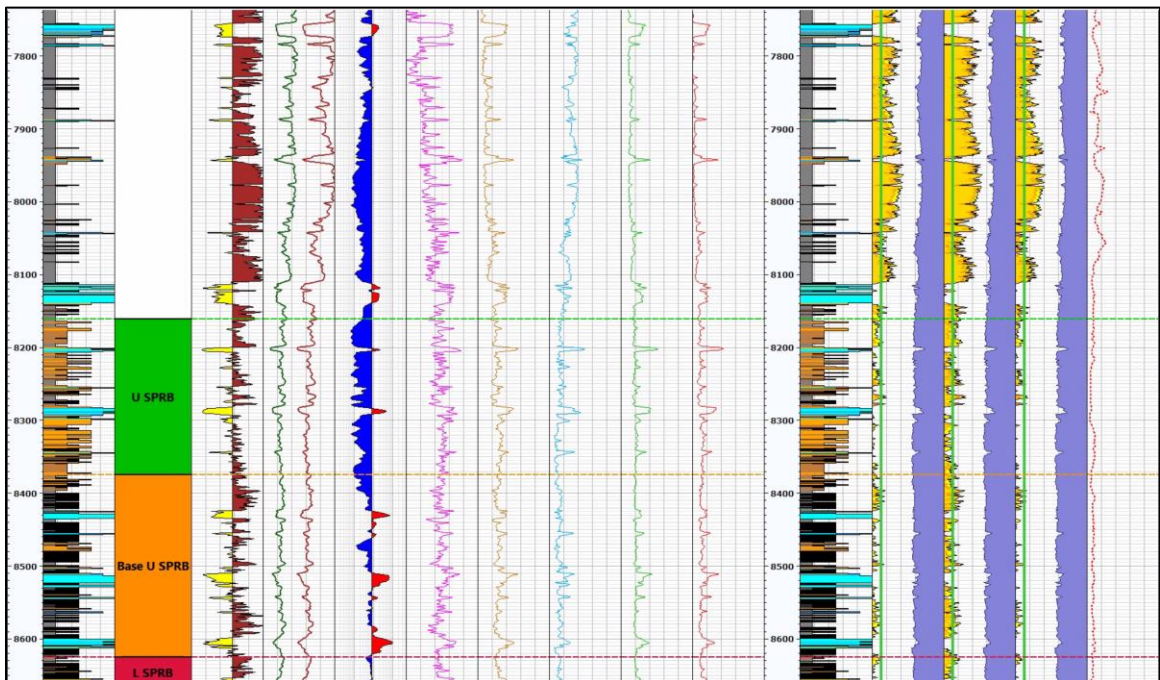


Figure 44: Example of zoomed in view of full model demonstrating accurate depictions of breakout and loss curve trends in relation to logs and facies curves.

It would be advised if targeting any of the intervals in the Spraberry trend, to make sure to set intermediate casing below the depth of 8105' MD. This guaranties avoidance of potential hole stability problems in the curve and lateral sections of the wellbore based on the predicted breakout threshold, the correlating data with image logs, the offset caliper corroboration, and calculated *UCS* and facies curves of the model.

All calculated log curves with the exception of *UCS* look to be strong and show a good correlation with quality control data points from core seen in Figure 14 in section 4.2.2. Young's modulus, Poisson's ratio, and bulk modulus curves demonstrate strong correlation to core data points. *UCS* in any of the three methods used to calculate it all appeared on the weaker end of the core data points as seen in **Error! Reference source not found.** and **Error! Reference source not found.** in section 4.5. Since it is weaker than core it may be safe to assume that the breakout curve is slightly skewed on the side of weaker rock strength, meaning it may portray a lower mud weight needed to reach the breakout point than reality. That being said, there is also such strong corroboration in quality control points for predicted breakout sections that it does not seem to be hurting the overall breakout model predictions by a significant amount when looking at the image log and caliper.

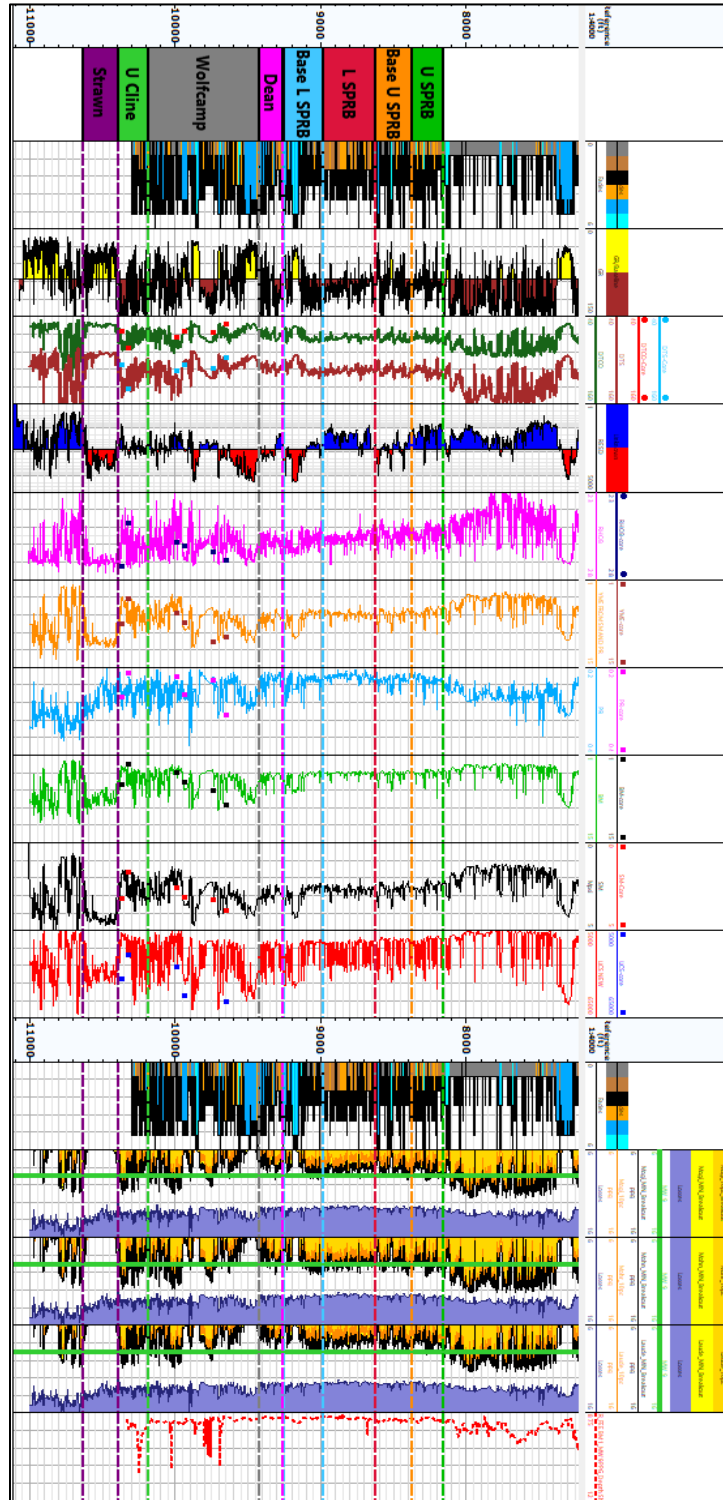
The only potential weak point of this model is the fact that there was no available quality control point or calibration data for the pore pressure gradient curve and in turn the minimum horizontal stress curve. Observing Figure 38 the loss threshold does seem to trend with predicted facies and other calculated/digital curves, however, given the lack of those data points, I cannot confidently assert it is calibrated well and predicting a true

loss threshold. However, some prediction is better than no prediction, and the fact that it does trend well is encouraging. I would not take the loss threshold mud weights at face value due to the above facts. But rather use the curve as a general guideline. Then look for future ways to improve the confidences in the pore pressure curve calculation or corresponding actual drilling data for losses observed while drilling offset wells.

5.1 Recommendations for Future Work

The “low hanging fruit” is finding quality control points for the pore pressure or offset drilling data to calibrate the loss threshold. The rest of the facets of the model appear to be strong and correlate well with lab driven data points from core. On the whole this model seems to be accurate, however, there is always room for improvement. Any nearby cored wells or quad-combo wells could be compared to improve upon and tighten up the calibration of some of the elastic property curves. Potential different techniques or a different facies model could be generated to get a stronger correlation for the *UCS* curve to core. This project and calculated dataset could be used along with the workflows to generate more 1D mechanical earth models of the surrounding area in Ector county and eventually be built into a full 3D model calibrated to a number of sources. This thesis was written based on a wellbore stability standpoint, however, the calculated elastic properties and calculated geomechanical curves could be used in completions modelling to help predict frac growth and recoverable oil. Generating an initial mechanical earth model is just a starting point for a great deal of potential future projects and the curves and workflows used in the modelling process are a good baseline for insights into the engineering and completions realm of the business.

5.2 Image of Final Model



REFERENCES

- Aadnøy, B.S., and Looyeh, R., 2019, Drilling Design and Selection of Optimal Mud Weight: Petroleum Rock Mechanics, p. 165–181, doi:10.1016/b978-0-12-815903-3.00010-8.
- Aadnøy, B.S., and Looyeh, R., 2019, In Situ Stress: 105–144 p., doi:10.1016/b978-0-12-815903-3.00008-x.
- Aadnøy, B.S., and Looyeh, R., 2019, Rock Strength and Rock Failure: Petroleum Rock Mechanics, p. 145–163, doi:10.1016/b978-0-12-815903-3.00009-1.
- Aadnøy, B.S., and Looyeh, R., 2019, Failure Criteria: Petroleum Rock Mechanics, p. 53–62, doi:10.1016/b978-0-12-815903-3.00005-4.
- Aadnøy, B.S., 1998, Geomechanical Analysis for Deep-Water Drilling: IADC/SPE Drilling Conference,.
- Abbas, A.K., Flori, R.E., and Alsaba, M., 2018, Geomechanical modeling and wellbore stability analysis approach to plan deep horizontal wells across problematic formations: SPE/AAPG/SEG Unconventional Resources Technology Conference 2018, URTC 2018, doi:10.15530/urtec-2018-2879569.
- Adisornsupawat, K., Tan, C.P., Anis, L., Vantala, A., Juman, R., and Boyce, B., 2011, Enhanced geomechanical modeling with advanced sonic processing to delineate and evaluate tight gas reservoirs: Society of Petroleum Engineers - SPE Middle East

- Unconventional Gas Conference and Exhibition 2011, UGAS, p. 546–554,
doi:10.2118/142813-ms.
- Aird, P., 2019, Deepwater Geology & Geoscience: 17–68 p., doi:10.1016/b978-0-08-102282-5.00002-8.
- Al-Ajmi, A.M., 2012, Mechanical Stability of Horizontal Wellbore Implementing Mogi-Coulomb Law: Advances in Petroleum Exploration and Development, v. 4, p. 28–36.
- Albukhari, T.M., Beshish, G.K., Abouzbeda, M.M., and Madi, A., 2018, Geomechanical wellbore stability analysis for the reservoir section in J-NC186 oil field: 1st International Conference on Advances in Rock Mechanics, TuniRock 2018, p. 179–193.
- Archer, S., and Rasouli, V., 2012, A log based analysis to estimate mechanical properties and in-situ stresses in a shale gas well in the Northern Perth Basin: WIT Transactions on Engineering Sciences, v. 80, p. 163–174, doi:10.2495/PMR120151.
- Asquith, G., and Krygowski, D., 2004, Basic Well Log Analysis (E. A. Mancini, Ed.): Tulsa, The American Association of Petroleum Geologist Methods in Exploration Series No.16, 244 p.
- Belyadi, H., and Belyadi, F., 2019, Rock mechanical properties and in situ stresses Simulation of Multistage Hydraulic Fracturing in Unconventional Reservoirs Using Displacement Discontinuity Method (DDM): Science Direct.

- Bhatnagar, P., S. Verma, R. Bianco, 2019, Geomorphologic character of an Upper Leonardian mass transport deposit, Midland Basin: insights from 3D seismic data: *Interpretation*, **7**, no. 4, 1–14. <http://dx.doi.org/10.1190/INT-2019-0036.1>
- Biot, M.A., and Willis, D.G., 1957, The Elastic Coefficients of the Theory of consolidation: *Journal of Applied Mechanics*, v. 48, p. 594–601, doi:10.1016/B978-0-444-98950-5.50011-3.
- Bohling, G.C., and Dubois, M.K., 2003, An integrated application of neural network and Markov chain techniques to prediction of lithofacies from well logs: Kansas Geological Survey, p. 6pp.
- Bowers, G.L., 1995, Pore pressure estimation from velocity data; accounting for overpressure mechanisms besides under compaction, *in* SPE/AAPG/SEG Unconventional Resources Technology Conference, The Leading Edge.
- Chang, C., Zoback, M.D., and Khaksar, A., 2006, Empirical relations between rock strength and physical properties in sedimentary rocks: *Journal of Petroleum Science and Engineering*, v. 51, p. 223–237.
- Crain, E.R., 2000, Crain's petrophysical handbook: Rocky Mountain House.
- Eaton, B.A., 1975, The Equation for Geopressure Prediction from Well Logs.
- Ewy, R.T., 1999, Wellbore-Stability Predictions by Use of a Modified Lade Criterion: *SPE Drilling & Completion*, v. 14, p. 85–91.

- Fanchi, J.R., 2006, Petroleum Engineering Handbook Volume 1: Society of Petroleum Engineers, 864 p.
- Fei, W., Huiyuan, B., Jun, Y., and Yonghao, Z., 2016, Correlation of Dynamic and Static Elastic Parameters of Rock: *Electronic Journal of Geotechnical Engineering*, v. 21, p. 1551–1560.
- Forand, D., Heesakkers, V., and Schwartz, K., 2017, Constraints on natural fracture and in-situ stress trends of unconventional reservoirs in the Permian Basin, USA: SPE/AAPG/SEG Unconventional Resources Technology Conference 2017, doi:10.15530/-urtec-2017-2669208.
- Formento, J.-L., 2004, Seismic Pore Pressure Prediction, *in* EAGE, Paris, https://www.cgg.com/technicaldocuments/cggv_0000001681.pdf. accessed on 28 July, 2020.
- Haidary, S.A., Shehri, H.A., Ahmem, A.A.M., and Alqam, M.H., 2015, Wellbore Stability Analysis for Trouble Free Drilling: Society of Petroleum Engineers, doi: <https://doi.org/10.2118/175170-MS>.
- Hall, B., 2016, Facies classification using machine learning: *Leading Edge*, v. 35, p. 906–909, doi:10.1190/tle35100906.1.
- Han, Y., Liu, C., Phan, D., AlRuwaili, K., and Abousleiman, Y., 2019, Advanced wellbore stability analysis for drilling naturally fractured rocks: SPE Middle East Oil

and Gas Show and Conference, MEOS, Proceedings, v. 2019-March,

doi:10.2118/195021-ms.

Hissong, R., 2020, Support vector machine prediction of lithofacies in Midland Basin in Wolf camp formation for GEOL 6323 Quantitative interpretation class project: UT Permian Basin.

Kadhim, F., Samsuri, A., and Idris, A.K., 2016, Using Well Log Data to Estimate Dynamic Elastic Properties of Carbonate Formations: European Centre for Research Training and Development UK, v. 4, p. 1–15.

Kadyrov, T., 2013, Integrated Wellbore Stability Analysis for Well Trajectory Optimization and Development: The West Kazakhstan Field: Colorado School of Mines.

Knöll, L., 2016, The Process of Building a Mechanical Earth Model Using Well Data: Master Thesis, <https://www.mendeley.com/viewer/?fileId=554d030a-17f3-f285-6c4d-a7d6a5bf7858&documentId=f4b91a59-9423-3f5a-9aea-e623667ae994>. accessed on 28 July, 2020.

Kowan, J., Ong, S., and Sheridan, J., 2017, Efficient Well Delivery in Shale Plays – Examples from the Marcellus and Permian, *in* 2017 Applied Geoscience Conference “Geomechanics of Unconventionals,” Houston, p. 15–16, doi:10.1145/3086467.3086475.

- Lade, P. V., 1977, Elasto-Plastic Stress-Strain Theory for Cohesionless Soil with Curved Yield Surfaces: *Solid Structures*, v. 13, p. 1019–1035.
- Liner, T.J., 2018, *Subsurface Analysis of Mississippian Tripolitic Chert in Northwest Arkansas*: University of Arkansas.
- Lund Snee, J.E., and Zoback, M.D., 2016, State of stress in Texas: Implications for induced seismicity: *Geophysical Research Letters*, v. 43, p. 10,208-10,214, doi:10.1002/2016GL070974.
- Luo, X., Were, P., Liu, J., and Hou, Z., 2015, Estimation of Biot's effective stress coefficient from well logs: *Environmental Earth Sciences*, v. 73, p. 7019–7028, doi:10.1007/s12665-015-4219-8.
- Mavko, G., Mukerji, T., and Dvorkin, J., 2009, *The Rock Physics Handbook*: Cambridge University Press, doi: 10.1017/CBO9780511626753.
- Mechanics, P.R., 1993, List of Symbols: *North-Holland Mathematical Library*, v. 48, p. 327–328, doi:10.1016/S0924-6509(08)70091-6.
- Milovac, J., 2009, *Seismic-Rock physics seminar*, http://www.rpl.uh.edu/papers/milovac_intro.pdf, accessed on 28 July, 2020.
- Ming, K., and Dorobek, S.L., 1995, *the Permian Basin of West Texas and New Mexico Tectonic History of a Foreland Basin and Its Effects on Stratigraphic Development*: Society for Sedimentary Geology, p. 150–174, doi:1-56576-016-6.

- Mogi, K., 1971, Fracture and Flow Under High Triaxial Compression: Geophysical Research, v. 76, p. 1255–1269.
- Najibi, A.R., Ghafoori, M., Gholam, L.R., and Asef, M.R., 2014, Empirical relations between strength and static and dynamic elastic properties of Asmari and Sarvak limestones, two main oil reservoirs in Iran: Journal of Petroleum Science and Engineering, v. 126,
<https://www.researchgate.net/publication/270344929> Empirical relations between strength and static and dynamic elastic properties of Asmari and Sarvak limestones two main oil reservoirs in Iran/citations.
- Osaki, L., Uko, E.D., Tamunobereton-ari, I., and Alabraba, M., 2019, Geomechanical Characterization of a Reservoir in Part of Niger Delta, Nigeria: Asian Journal of Applied Science and Technology (AJAST), v. 3, p. 10–30.
- Ouenes, A., Umholtz, N.M., and Aimene, Y.E., 2016, Using geomechanical modeling to quantify the impact of natural fractures on well performance and microseismicity: Application to the Wolfcamp, Permian Basin, Reagan County, Texas: Interpretation, v. 4, p. SE1–SE15, doi:10.1190/int-2015-0134.1.
- Patzek, T., 2005, Biot Theory (Almost) For Dummies: Seminar at the University of Houston, p. 32.
- Rahimi, R., 2014, The effect of using different rock failure criteria in wellbore stability analysis: Masters Thesis, p. 72, https://scholarsmine.mst.edu/masters_theses/7270., accessed on 28 July, 2020.

Rotrends.net, 2020, Crude oil price graph graphical representation,
[rotrends.net/2566/crude-oil-prices-today-live
chart#targetText=Crude%20Oil%20Prices%20Today%20%2D%20Live%20Chart,2019
%20is%2052.81%20per%20barrel](https://rotrends.net/2566/crude-oil-prices-today-live-chart#targetText=Crude%20Oil%20Prices%20Today%20%2D%20Live%20Chart,2019%20is%2052.81%20per%20barrel). July 27th, 2020 BPD WTI crude oil price graphical
representation, accessed on 27 July, 2020.

RRC (Texas Rail Road Commission), 2020, <https://gis.rrc.texas.gov/GISViewer/>,
accessed on 27 July, 2020.

Schlumberger, 2020, Schlumberger Oilfield Glossary: Pore Pressure:
https://www.glossary.oilfield.slb.com/en/Terms/p/pore_pressure.aspx, accessed on
28 July, 2020.

ShaleXP.com, 2020, Oil & Gas Activity in Ector County, TX,
<https://www.shalexp.com/texas/ector-county>, accessed on 28 July, 2020.

Singh, A., Rao, K.S., and Ayothiraman, R., 2019, An analytical solution to wellbore
stability using Mogi-Coulomb failure criterion: *Journal of Rock Mechanics and
Geotechnical Engineering*, v. 11, p. 1211–1230, doi:10.1016/j.jrmge.2019.03.004.

Słota-Valim, M., 2015, Static and dynamic elastic properties, the cause of the difference
and conversion methods – case study: *Research Gate*, v. 71, p. 816–826,
doi:10.18668/ng2015.11.02.

Tingay, M., Reinecker, J., and Müller, B., 1998, Borehole breakout and drilling-induced
fracture analysis from image logs: , p. 1–8.

- Verma, S., and M. Scipione, 2020, Influence of the Early Paleozoic structures on the Permian strata, Midland Basin: insights from multi-attribute seismic analysis: *Journal of Natural Gas Science and Engineering*, <https://doi.org/10.1016/j.jngse.2020.103521>.
- Ulmo, G., 2018, Geologic Nomenclature of the Midland Basin and Basin Formation, in Midland, TX, at SM Energy: Short Courses p. 13.
- Wang, J., and Weijermars, R., 2019, Expansion of Horizontal Wellbore Stability Model for Elastically Anisotropic Shale Formations With Anisotropic Failure Criteria: Permian Basin Case Study, *in* 53rd U.S. Rock Mechanics/Geomechanics Symposium, New York City, New York, American Rock Mechanics Association.
- Warner Jr, H.R., and Holstein, E.D., 2007, *Petroleum Engineering Handbook*: , p. 1103–1147.
- Yandell, J., C. Whaley, S. Verma, and M. A. Henderson, 2019, Integration of 3D seismic, Well, and Core Data to investigate channel-like features in the Grayburg Formation, Midland Basin, TX: Poster presentation at AAPG SWS section annual meeting.
- Zahiri, J., Abdideh, M., and Ghaleh Golab, E., 2019, Determination of safe mud weight window based on well logging data using artificial intelligence: *Geosystem Engineering*, v. 22, p. 193–205, doi:10.1080/12269328.2018.1504697.

- Zhang, J., 2011, Pore pressure prediction from well logs: Methods, modifications, and new approaches: *Earth-Science Reviews*, v. 108, p. 50–63, doi:10.1016/j.earscirev.2011.06.001.
- Zhang, J., 2013, Effective stress, porosity, velocity and abnormal pore pressure prediction accounting for compaction disequilibrium and unloading: *Marine and Petroleum Geology*, v. 45, p. 2–11, doi:10.1016/j.marpetgeo.2013.04.007.
- Zhang, J.J., 2020, *Applied Petroleum Geomechanics*: Gulf Professional Publishing, 553 p.
- Zhang, L., Cao, P., and Radha, K.C., 2010, Evaluation of Rock Strength Criteria for Wellbore Stability Analysis: *International Journal of Rock Mechanics and Mining Sciences*, v. 47, p. 1304–1316, doi:10.1016/j.ijrmms.2010.09.001.
- Zheng, W., Xu, L., Pankaj, P., Ajisafe, F., and Li, J., 2018, Advanced Modeling of Production Induced Stress Change Impact on Wellbore Stability of Infill Well Drilling in Unconventional Reservoirs, *in Proceedings of the 6th Unconventional Resources Technology Conference*,.

APPENDIX

Appendix A: List of Equations

$$\text{Static: } E = \sigma / \varepsilon \quad \dots\dots\dots (1)$$

$$\text{Dynamic: } E_{dyn} = \rho V_S^2 [(3V_P^2 - 4 V_S^2) / (V_P^2 - V_S^2)] \quad \dots\dots\dots (2)$$

$$E_{dyn} = 2 * G * (1 + \nu) \quad \dots\dots\dots (3)$$

$$\text{Static: } \nu = \varepsilon_{trans} / \varepsilon_{axial} \quad \dots\dots\dots (4)$$

$$\text{Dynamic: } \nu_{dyn} = (V_P^2 - 2*V_S^2) / (2 (V_P^2 - V_S^2)) \quad \dots\dots\dots (5)$$

$$G = [F/A] / [\Delta x/l] \quad \dots\dots\dots (6)$$

$$G = \rho V_S^2 \quad \dots\dots\dots (7)$$

$$K = \Delta P / [\Delta V/V] \quad \dots\dots\dots (8)$$

$$K = \rho (V_P^2 - (4/3) V_S^2) \quad \dots\dots\dots (9)$$

$$V_S = 0.8042 * V_P - 855.9 \quad \dots\dots\dots (10)$$

$$\sigma_v = \sum_i \rho_i h_i g \quad \dots\dots\dots (11)$$

$$\sigma_h = [(\nu / 1 - \nu) \sigma_v] + [(1 - 2 \nu / 1 - \nu) P_p \alpha] + [(E / 1 - \nu^2) \varepsilon_y] + [(E \nu / 1 - \nu^2) \varepsilon_x] \quad \dots\dots (12)$$

$$\text{Isotropic } \sigma_h = (\nu / 1 - \nu)(\sigma_v - \alpha_v P_p) + \alpha_H P_p + \sigma_{tect} \quad \dots\dots\dots (13)$$

$$\sigma_H = [(\nu / 1 - \nu) * (\sigma_v - P_p \alpha)] + P_p \alpha + \sigma_{tect} \quad \dots\dots\dots (14)$$

$$\alpha = 1 - (K_b / K_m) \quad \dots\dots\dots (15)$$

$$K_b = \rho * (1 / (DTC^2) - (4/3) * (1 / (DTS^2))) \quad \dots\dots\dots (16)$$

$$K_m = \rho_m * (1 / (DTC^2) - (4/3) * (1 / (DTS^2))) \quad \dots\dots\dots (17)$$

$$V_P = V_{ml} + C \sigma_v^B \quad \dots\dots\dots (18)$$

$$P_p = \sigma_v - ((V_P - V_{ml}) / C)^{1/B} \quad \dots\dots\dots (19)$$

$$P_{pulo} = \sigma_v - ((V_P - V_{ml}) / C)^{U/B} * (\sigma_{max}^{1-U}) \quad \dots\dots\dots (20)$$

$$P_p = \sigma_v - (\sigma_v - Pp_{ng}) * (\Delta t_n / \Delta t)^n \dots\dots\dots (21)$$

$$P_p = \sigma_v - (\sigma_v - G_{hyd} * TVD) * (V_{norm} - V_{comp})^n \dots\dots\dots (22)$$

$$\tau_{max} = (1/2)(\sigma_1 - \sigma_3) \dots\dots\dots (23)$$

$$\tau_{oct} = a + b \sigma_{m2} \dots\dots\dots (24)$$

$$a = ((2\sqrt{2}) / 3) * (C_o / q) \dots\dots\dots (25)$$

$$b = ((2\sqrt{2}) / 3) * ((q-1) / (q+1)) \dots\dots\dots (26)$$

$$q \text{ conversion} = (1 + \sin(\phi)) / (1 - \sin(\phi)) \dots\dots\dots (27)$$

$$(I_1^n)^3 / (I_3^n) = 27 + \eta \dots\dots\dots (28)$$

$$I_1 = (\sigma_1 + S) + (\sigma_2 + S) + (\sigma_3 + S) \dots\dots\dots (29)$$

$$I_3 = (\sigma_1 + S) * (\sigma_2 + S) * (\sigma_3 + S) \dots\dots\dots (30)$$

$$S \text{ conversion} = C_o / \tan(\phi) \dots\dots\dots (31)$$

$$\eta \text{ conversion} = (4 \tan^2(\phi) * (9 - 7 \sin(\phi))) / (1 - \sin(\phi)) \dots\dots\dots (32)$$

$$\text{Loss Threshold} = (\sigma_h / MD) / 0.052 \dots\dots\dots (33)$$

Appendix B: List of Variables

σ = stress

ε = strain

ρ = bulk density

V_S = shear wave velocity

V_P = compressional or primary wave velocity

ε_{axial} = axial strain

ε_{trans} = transverse strain

F = the shear force applied

A = the cross-sectional area of material with area parallel to the applied force vector

Δx = shear displacement

l = initial length

ΔP = change of pressure

ΔV = change in volume

V = initial volume of material

σ_v = overburden stress

σ_h = minimum horizontal stress,

σ_H = maximum horizontal stress

g = is the gravitational constant (32.175 ft/s²)

h = the vertical thickness of rock formation (ft)

ρ_i = the density of the i^{th} rock layer (lb_m/ft³)

$P_p = \text{pore pressure}$

$\alpha = \text{Biot elastic constant}$

$\varepsilon_y = \text{vertical strain}$

$\varepsilon_x = \text{lateral strain}$

$\alpha_v = \text{Biot elastic constant (vertical)}$

$\alpha_H = \text{Biot elastic constant (horizontal)}$

$\sigma_{tect} = \text{tectonic stress}$

$\phi = \text{friction angle}$

$C, B, \text{ and } U = \text{constants for calibration Bowers method}$

$P_{p_{ulo}} = \text{pore pressure in unloading}$

$\sigma_{max} = \text{the estimated effective stress at the onset unloading}$

$P_{p_{ng}} = \text{pore pressure of hydrostatic pressure}$

$\Delta t = \text{sonic delta time}$

$n = \text{constant for calibration Eaton's}$

$G_{hyd} = \text{gradient of hydrostatic pressure}$

$V_{norm} = \text{Velocity log value according to normal trend}$

$V_{comp} = \text{Velocity log value according to compaction trend}$

$TVD = \text{True Vertical Depth}$

$\tau_{max} = \text{the maximum shear stress}$

$\sigma_1 = \text{maximum principal stress}$

$\sigma_2 = \text{intermediate principal stress}$

$\sigma_3 = \text{minimum principal stress}$

$\tau_{oct} = \text{max octahedral shear stress}$

$\sigma_{m2} = \text{intermediate effective mean stress}$

$a = \text{intersection of the line on } \tau_{oct} \text{ axis}$

$b = \text{the line's inclination}$

$C_o = \text{Cohesion}$

$I_1 = \text{first stress invariant}$

$I_3 = \text{third stress invariant}$

$\eta = \text{material constant}$

$S = \text{stress}$

$DTC = \text{compressional wave travel time}$

$DTS = \text{shear wave travel time}$

$K_b = \text{bulk modulus of base material}$

$K_m = \text{bulk modulus of rock matrix}$

$K = \text{bulk modulus}$

$G = \text{shear modulus}$

$\nu = \text{Poisson's ratio}$

$E = \text{Young's modulus}$

$MD = \text{measured depth}$

Appendix C: Conversion Tables

Conversions	Conversions
$1 \text{ g/cm}^3 = 9.81 \text{ MPa/km}$	$1 \text{ ppg} = 0.051948 \text{ psi/ft}$
$1 \text{ g/cm}^3 = 0.00981 \text{ MPa/m}$	$1 \text{ ppg} = 0.12 \text{ g/cm}^3$
$1 \text{ g/cm}^3 = 1 \text{ SG}$	$1 \text{ ppg} = 0.12 \text{ SG}$
$1 \text{ MPa/km} = 0.102 \text{ SG} = 0.102 \text{ g/cm}^3$	$1 \text{ ppg} = 1.177 \text{ MPa/km}$
$1 \text{ MPa/km} = 1 \text{ kPa/m}$	$1 \text{ ppg} = 1.177 \text{ kPa/m}$
$1 \text{ g/cm}^3 = 8.345 \text{ ppg}$	$1 \text{ psi/ft} = 19.25 \text{ ppg}$
$1 \text{ g/cm}^3 = 0.4335 \text{ psi/ft}$	$1 \text{ psi/ft} = 2.31 \text{ g/cm}^3$
$1 \text{ SG} = 8.345 \text{ ppg}$	$1 \text{ psi/ft} = 22.66 \text{ MPa/km}$
$1 \text{ SG} = 0.4335 \text{ psi/ft}$	$1 \text{ psi/ft} = 2.31 \text{ SG}$
$1 \text{ SG} = 62.428 \text{ pcf (lb/ft}^3)$	$1 \text{ ppg} = 7.4805 \text{ pcf}$

Table 12: Table referencing conversions to and from metric and imperial unit of measurement systems (Zhang, 2011).

Appendix D: Facies Python Code

```
import numpy as np # linear algebra
import pandas as pd # data processing, CSV file I/O (e.g. pd.read_csv)
import os
for dirname, _, filenames in os.walk('/kaggle/input'):
    for filename in filenames:
        print(os.path.join(dirname, filename))
# From R Hissong, using Brendon Hall (Facies Classification with Machine Learning:
# Notebook workflow used for a UTPB Quantitative Interpretation Lab 4-18-2020)
# This notebook demonstrates how to train a machine learning algorithm to predict facies
# from well log data. The dataset we will use comes from a downloaded and digitized
# public logs from the TRRC. This exercise uses machine learning techniques to predict log
# facies from core defined facies analysis on logs. For more info on the original workflow
# and data, see Bohling and Dubois (2003) and Dubois et al. (2007).
# The dataset we will use is log data from four wells that have been labelled with a facies
# type based on log data and ran through a random forest method broken down into 6
# facies. We will use this log data to train a support vector machine to classify facies types.
# Support vector machines (or SVMs) are a type of supervised learning model that can be
# trained on data to perform classification and regression tasks. The SVM algorithm uses
# the training data to fit an optimal hyperplane between the different classes (or facies, in
# our case). We will use the SVM implementation in scikit-learn.
# First we will explore the dataset. We will load the training data from 4 wells, and take a
# look at what we have to work with. We will plot the data from a couple wells, and create
# cross plots to look at the variation within the data.
# Next we will condition the data set. We will remove the entries that have incomplete
# data. The data will be scaled to have zero mean and unit variance. We will also split the
# data into training and test sets.
# We will then be ready to build the SVM classifier. We will demonstrate how to use the
# cross validation set to do model parameter selection.
# Finally, once we have a built and tuned the classifier, we can apply the trained model to
# classify facies in wells which do not already have labels. We will apply the classifier to
# two wells, but in principle you could apply the classifier to any number of wells that had
# the same log data.
%matplotlib inline
```

```

import pandas as pd
import numpy as np
import matplotlib as mpl
import matplotlib.pyplot as plt
import matplotlib.colors as colors

from mpl_toolkits.axes_grid1 import make_axes_locatable
from pandas import set_option

set_option("display.max_rows", 10)

pd.options.mode.chained_assignment = None

training_data = pd.read_excel("../input/testdata/test.xlsx", sheet_name='RH Facies Lab
Data')

training_data

# we will remove one well from the training set so that we can compare
# the predicted and actual facies labels.

blind = training_data[training_data['Well Name'] == 'well 2']
training_data = training_data[training_data['Well Name'] != 'well 2']

blind

# Let's clean up this dataset. The 'Well Name' column
# can be turned into a categorical data type.

training_data['Well Name'] = training_data['Well Name'].astype('category')
training_data['Well Name'].unique()

#Now we label and color our facies

# 1=Mudstone_Org_Si 2=Mudstone_Org 3=Mudstone_ORG_Cal
# 4=Mudstone_Cal_Si 5=Limestone_Arg_Dol 6=Limestone_Arg
facies_colors = ['#A09D92', '#8E7308', '#0B0901', '#F5D451',
                 '#EE44BB', '#44BBEE']

facies_labels = ['MSOrgSi', 'MSOrg', 'MSOrgCal', 'MSCalSi', 'LSArgDol',
                 'LSArg']

```

```

#facies_color_map is a dictionary that maps facies labels
#to their respective colours
facies_color_map = {}
for ind, label in enumerate(facies_labels):
    facies_color_map[label] = facies_colors[ind]

#note: this next step gives you a breakdown of the data, if you need to see if data busts
exist like -999s then just delete the 3 rows and use "training_data.describe()" function to
generate a table
def label_facies(row, labels):
    return labels[ row['Facies'] -1]

training_data.loc[:, 'FaciesLabels'] = training_data.apply(lambda row: label_facies(row,
facies_labels), axis=1)
training_data.describe()

# Let's take a look at the data from individual wells in a more familiar log plot form.
# We will create plots for the five well log variables, as well as a log for facies labels.
def make_facies_log_plot(logs, facies_colors):
    #make sure logs are sorted by depth
    logs = logs.sort_values(by='Depth')
    cmap_facies = colors.ListedColormap(
        facies_colors[0:len(facies_colors)], 'indexed')
    ztop=(5896); zbot=(8140)
    cluster=np.repeat(np.expand_dims(logs['Facies'].values,1), 100, 1)
    f, ax = plt.subplots(nrows=1, ncols=6, figsize=(8, 12))
    ax[0].plot(logs.GR, logs.Depth, '-g')
    ax[1].plot(logs.ILD_log10, logs.Depth, '-')
    ax[2].plot(logs.DeltaPHI, logs.Depth, '-', color='0.5')
    ax[3].plot(logs.PHIND, logs.Depth, '-', color='r')
    ax[4].plot(logs.RHOB, logs.Depth, '-', color='black')
    im=ax[5].imshow(cluster, interpolation='none', aspect='auto',

```

```

        cmap=cmap_facies,vmin=1,vmax=6)
divider = make_axes_locatable(ax[5])
cax = divider.append_axes("right", size="20%", pad=0.05)
cbar=plt.colorbar(im, cax=cax)
cbar.set_label(((17*' ').join([ 'MSOrgSi ', 'MSOrg ', 'MSOrgCal ', 'MSCalSi ', '
LSArgDol ',
        'LSArg ']))
cbar.set_ticks(range(0,1)); cbar.set_ticklabels("")
for i in range(len(ax)-1):
    ax[i].set_ylim(ztop,zbot)
    ax[i].invert_yaxis()
    ax[i].grid()
    ax[i].locator_params(axis='x', nbins=3)
ax[0].set_xlabel("GR")
ax[0].set_xlim(0,200)
ax[1].set_xlabel("ILD_log10")
ax[1].set_xlim(0,500)
ax[2].set_xlabel("DeltaPHI")
ax[2].set_xlim(0,0.8)
ax[3].set_xlabel("PHIND")
ax[3].set_xlim(0.1,0.5)
ax[4].set_xlabel("RHOB")
ax[4].set_xlim(1,3)
ax[5].set_xlabel('Facies')
ax[1].set_yticklabels([]); ax[2].set_yticklabels([]); ax[3].set_yticklabels([])
ax[4].set_yticklabels([]); ax[5].set_yticklabels([])
ax[5].set_xticklabels([])
f.suptitle('Well: %s'%logs.iloc[0]['Well Name'], fontsize=14,y=0.94)

```

```

# We then show log plots for well 3.
make_facies_log_plot(
    training_data[training_data['Well Name'] == 'well 3'],
    facies_colors)
# Now for well 4.
make_facies_log_plot(
    training_data[training_data['Well Name'] == 'well 4'],
    facies_colors)
# Now for well 5.
#Note:since we set our well 2 as training data it can not be displayed using this code
make_facies_log_plot(
    training_data[training_data['Well Name'] == 'well 5'],
    facies_colors)
#count the number of unique entries for each facies, sort them by
#facies number (instead of by number of entries)
facies_counts = training_data['Facies'].value_counts().sort_index()
#use facies labels to index each count
facies_counts.index = facies_labels
facies_counts.plot(kind='bar',color=facies_colors,
                    title='Distribution of Training Data by Facies')
facies_counts
#save plot display settings to change back to when done plotting with seaborn
inline_rc = dict(mpl.rcParams)
one_hot_encoded_training_predictors = pd.get_dummies(training_data)
import seaborn as sns
sns.set()
sns.pairplot(training_data.drop(['Well
Name', 'Facies', 'Depth', 'DeltaPHI', 'PHIND'],axis=1),

```

```

#Not sure why but I cant get the DeltaPHI or PHIND to plot it gives a error -Rob
hue='FaciesLabels', palette=facies_color_map,
hue_order=list(reversed(facies_labels)))
#switch back to default matplotlib plot style
mpl.rcParams.update(inline_rc)
#Now have visualized all we can, now its time to condition the data for use in creating
our predictors and vectors
# We extract just the feature variables we need to perform the classification.
# The predictor variables are the four wireline wells and facies variables.
# We also get a vector of the facies labels that correspond to each feature vector.
correct_facies_labels = training_data['Facies'].values
feature_vectors = training_data.drop(['Well Name', 'Depth', 'Facies', 'FaciesLabels'],
axis=1)
feature_vectors.describe()
#make note if counts are off or min/max is unusual
#This creates our vectors
from sklearn import preprocessing
scaler = preprocessing.StandardScaler().fit(feature_vectors)
scaled_features = scaler.transform(feature_vectors)
feature_vectors
# Split to test and training data, test will be used to compare the accuracy of the model
from sklearn.model_selection import train_test_split
X_train, X_test, y_train, y_test = train_test_split(
    scaled_features, correct_facies_labels, test_size=0.2, random_state=42)
#Training the classifier
from sklearn import svm
clf = svm.SVC()
clf.fit(X_train,y_train)
#Predict

```

```

predicted_labels = clf.predict(X_test)

# a function has been written to display the matrix along with facies labels and various
error metrics.

def display_cm(cm, labels, hide_zeros=False,
              display_metrics=False):
    """Display confusion matrix with labels, along with
    metrics such as Recall, Precision and F1 score.
    Based on Zach Guo's print_cm gist at
    https://gist.github.com/zachguo/10296432
    """
    precision = np.diagonal(cm)/cm.sum(axis=0).astype('float')
    recall = np.diagonal(cm)/cm.sum(axis=1).astype('float')
    F1 = 2 * (precision * recall) / (precision + recall)
    precision[np.isnan(precision)] = 0
    recall[np.isnan(recall)] = 0
    F1[np.isnan(F1)] = 0
    total_precision = np.sum(precision * cm.sum(axis=1)) / cm.sum(axis=(0,1))
    total_recall = np.sum(recall * cm.sum(axis=1)) / cm.sum(axis=(0,1))
    total_F1 = np.sum(F1 * cm.sum(axis=1)) / cm.sum(axis=(0,1))
    #print total_precision
    columnwidth = max([len(x) for x in labels]+[5]) # 5 is value length
    empty_cell = " " * columnwidth
    # Print header
    print(" " + " Pred", end=' ')
    for label in labels:
        print("%{0}s".format(columnwidth) % label, end=' ')
    print("%{0}s".format(columnwidth) % 'Total')
    print(" " + " True")

```

```

# Print rows
for i, label1 in enumerate(labels):
    print("  % {0}s".format(columnwidth) % label1, end=' ')
    for j in range(len(labels)):
        cell = "% {0}d".format(columnwidth) % cm[i, j]
        if hide_zeros:
            cell = cell if float(cm[i, j]) != 0 else empty_cell
        print(cell, end=' ')
    print("% {0}d".format(columnwidth) % sum(cm[i,:]))
if display_metrics:
    print()
    print("Precision", end=' ')
    for j in range(len(labels)):
        cell = "% {0}.2f".format(columnwidth) % precision[j]
        print(cell, end=' ')
    print("% {0}.2f".format(columnwidth) % total_precision)
    print("  Recall", end=' ')
    for j in range(len(labels)):
        cell = "% {0}.2f".format(columnwidth) % recall[j]
        print(cell, end=' ')
    print("% {0}.2f".format(columnwidth) % total_recall)
    print("    F1", end=' ')
    for j in range(len(labels)):
        cell = "% {0}.2f".format(columnwidth) % F1[j]
        print(cell, end=' ')
    print("% {0}.2f".format(columnwidth) % total_F1)
def display_adj_cm(
    cm, labels, adjacent_facies, hide_zeros=False,

```

```

        display_metrics=False):
    """This function displays a confusion matrix that counts
        adjacent facies as correct.
    """
    adj_cm = np.copy(cm)
    for i in np.arange(0,cm.shape[0]):
        for j in adjacent_facies[i]:
            adj_cm[i][i] += adj_cm[i][j]
            adj_cm[i][j] = 0.0
    display_cm(adj_cm, labels, hide_zeros,
                display_metrics)

#create our confusion matrix
from sklearn.metrics import confusion_matrix
conf = confusion_matrix(y_test, predicted_labels)
display_cm(conf, facies_labels, hide_zeros=True)

# define our accuracy
def accuracy(conf):
    total_correct = 0.
    nb_classes = conf.shape[0]
    for i in np.arange(0,nb_classes):
        total_correct += conf[i][i]
    acc = total_correct/sum(sum(conf))
    return acc

# Define error within 'adjacent facies'
#This needs to be updated for 6 facies model ,np.array
adjacent_facies = np.array([[1], [0,3], [1], [0,3], [1], [1], [1], [5], [3]])
def accuracy_adjacent(conf, adjacent_facies):
    nb_classes = conf.shape[0]

```

```

total_correct = 0.
for i in np.arange(0,nb_classes):
    total_correct += conf[i][i]
    for j in adjacent_facies[i]:
        total_correct += conf[i][j]
return total_correct / sum(sum(conf))

#display accuracy
print('Facies classification accuracy = %f' % accuracy(conf))
print('Adjacent facies classification accuracy = %f' % accuracy_adjacent(conf,
adjacent_facies))

#Note: the misclassification is not severe (how close it is to value of 1)
#Note: this will take some time please wait for it to run the parameter loop...
#this checks our C values and trained well error
do_model_selection = True
if do_model_selection:
    C_range = np.array([.01, 1, 5, 10, 20, 50, 100, 1000, 5000, 10000])
    gamma_range = np.array([0.0001, 0.001, 0.01, 0.1, 1, 10])
    fig, axes = plt.subplots(3, 2,
                            sharex='col', sharey='row',figsize=(10,10))
    plot_number = 0
    for outer_ind, gamma_value in enumerate(gamma_range):
        row = int(plot_number / 2)
        column = int(plot_number % 2)
        cv_errors = np.zeros(C_range.shape)
        train_errors = np.zeros(C_range.shape)
        for index, c_value in enumerate(C_range):
            clf = svm.SVC(C=c_value, gamma=gamma_value)
            clf.fit(X_train,y_train)

```

```

train_conf = confusion_matrix(y_train, clf.predict(X_train))
cv_conf = confusion_matrix(y_test, clf.predict(X_test))
cv_errors[index] = accuracy(cv_conf)
train_errors[index] = accuracy(train_conf)
ax = axes[row, column]
ax.set_title('Gamma = %g'%gamma_value)
ax.semilogx(C_range, cv_errors, label='CV error')
ax.semilogx(C_range, train_errors, label='Train error')
plot_number += 1
ax.set_ylim([0.2,1])
ax.legend(bbox_to_anchor=(1.05, 0), loc='lower left', borderaxespad=0.)
fig.text(0.5, 0.03, 'C value', ha='center',
        fontsize=14)
fig.text(0.04, 0.5, 'Classification Accuracy', va='center',
        rotation='vertical', fontsize=14)
#display accuracy at %.2f
clf = svm.SVC(C=10, gamma=1)
clf.fit(X_train, y_train)
cv_conf = confusion_matrix(y_test, clf.predict(X_test))
print('Optimized facies classification accuracy = %.2f % accuracy(cv_conf))
print('Optimized adjacent facies classification accuracy = %.2f %
accuracy_adjacent(cv_conf, adjacent_facies))
#display cm confusion matrix with precisions
display_cm(cv_conf, facies_labels,
          display_metrics=True, hide_zeros=True)
#display adj_cm confusion matrix with precisions
display_adj_cm(cv_conf, facies_labels, adjacent_facies,
              display_metrics=True, hide_zeros=True)

```

```

# Applying the classification model to the blind data
# We held a well back from the training, and stored it in a dataframe called blind: (well 2)
blind
#defines Y_blind as facies
y_blind = blind['Facies'].values
#drops unneeded columns
well_features = blind.drop(['Facies', 'Well Name', 'Depth'], axis=1)
well_features.describe()
# Now we can transform this with the scaler we made before:
X_blind = scaler.transform(well_features)
# use the predictor we created storing it back in the dataframe:
y_pred = clf.predict(X_blind)
blind['Prediction'] = y_pred
# Let's see how we did with the confusion matrix
cv_conf = confusion_matrix(y_blind, y_pred)
print('Optimized facies classification accuracy = %.2f % accuracy(cv_conf))
print('Optimized adjacent facies classification accuracy = %.2f %
accuracy_adjacent(cv_conf, adjacent_facies))
#not to shabby...
#display the confusion matrix with precisions
display_cm(cv_conf, facies_labels,
           display_metrics=True, hide_zeros=True)
#now lets see how it does on the adj facies confusion matrix
# but does remarkably well on the adjacent facies predictions.
display_adj_cm(cv_conf, facies_labels, adjacent_facies,
              display_metrics=True, hide_zeros=True)
def compare_facies_plot(logs, compadre, facies_colors):
    #make sure logs are sorted by depth

```

```

logs = logs.sort_values(by='Depth')
cmap_facies = colors.ListedColormap(
    facies_colors[0:len(facies_colors)], 'indexed')
ztop=(5896); zbot=(8140)
cluster1 = np.repeat(np.expand_dims(logs['Facies'].values,1), 100, 1)
cluster2 = np.repeat(np.expand_dims(logs[compadre].values,1), 100, 1)
f, ax = plt.subplots(nrows=1, ncols=7, figsize=(9, 12))
ax[0].plot(logs.GR, logs.Depth, '-g')
ax[1].plot(logs.ILD_log10, logs.Depth, '-')
ax[2].plot(logs.DeltaPHI, logs.Depth, '-', color='0.5')
ax[3].plot(logs.PHIND, logs.Depth, '-', color='r')
ax[4].plot(logs.RHOB, logs.Depth, '-', color='black')
im1 = ax[5].imshow(cluster1, interpolation='none', aspect='auto',
    cmap=cmap_facies,vmin=1,vmax=6)
im2 = ax[6].imshow(cluster2, interpolation='none', aspect='auto',
    cmap=cmap_facies,vmin=1,vmax=6)
divider = make_axes_locatable(ax[6])
cax = divider.append_axes("right", size="20%", pad=0.05)
cbar=plt.colorbar(im2, cax=cax)
cbar.set_label(((17*' ').join(['MSOrgSi ', 'MSOrg ', 'MSOrgCal ', 'MSCalSi ',
LSArgDol ',
    'LSArg ']))
cbar.set_ticks(range(0,1)); cbar.set_ticklabels("")
for i in range(len(ax)-2):
    ax[i].set_ylim(ztop,zbot)
    ax[i].invert_yaxis()
    ax[i].grid()
    ax[i].locator_params(axis='x', nbins=3)

```

```

ax[0].set_xlabel("GR")
ax[0].set_xlim(0,200)
ax[1].set_xlabel("ILD_log10")
ax[1].set_xlim(0,500)
ax[2].set_xlabel("DeltaPHI")
ax[2].set_xlim(0,0.8)
ax[3].set_xlabel("PHIND")
ax[3].set_xlim(0.1,0.5)
ax[4].set_xlabel("RHOB")
ax[4].set_xlim(1,3)
ax[5].set_xlabel('Facies')
ax[6].set_xlabel(compadre)
ax[1].set_yticklabels([]); ax[2].set_yticklabels([]); ax[3].set_yticklabels([])
ax[4].set_yticklabels([]); ax[5].set_yticklabels([])
ax[5].set_xticklabels([])
ax[6].set_xticklabels([])
f.suptitle('Well: %s'%logs.iloc[0]['Well Name'], fontsize=14,y=0.94)
# Now we create the comparison of predicted facies vs actual from the random forest
classification dataset
compare_facies_plot(blind, 'Prediction', facies_colors)
#### Now lets test this bad boy on a well with no facies descriptions
#we will have to import the well 1 dataset so please add it in now
# Now that we have a trained facies classification model we can use it to
# identify facies in wells that do not have core data.
# In this case, we will apply the classifier to one well,
# but we could use it on any number of wells for which we have the same set of well logs
for input.
# This dataset is similar to the training data except it does not have facies labels.
#/kaggle/input/well-1/well1.xlsx

```

```

well_data = pd.read_excel("../input/well-1/well1.xlsx",sheet_name='Sheet1')
well_data['Well Name'] = well_data['Well Name'].astype('category')
well_features = well_data.drop(['Well Name', 'Depth'], axis=1)
# The data needs to be scaled using the same constants we used for the training data.
X_unknown = scaler.transform(well_features)
# predict facies of unclassified data
y_unknown = clf.predict(X_unknown)
well_data['Facies'] = y_unknown
well_data
# defines well 1 as unique
well_data['Well Name'].unique()
# We can use the well log plot to view the classification results along with the well logs.
make_facies_log_plot(
    well_data[well_data['Well Name'] == 'well 1'],
    facies_colors=facies_colors)
# Finally we can write out a csv file with the well data along with the facies classification
results.
# CONGRATS!!!!!!!!!!!!!! you just did some high level facies prediction and
classifications by machine learning
well_data.to_csv('well_data_with_facies.csv')

```